# Investigations of Injectors for Scramjet Engines

by Luca Maddalena

Dissertation submitted to the Faculty of the
Virginia Polytechnic Institute and State University
in partial fulfillment of the requirements for the degree of

Doctor of Philosophy
in
Aerospace Engineering

Dr. Joseph Schetz, Chair
Dr. Claudio Bruno, Committee Member
Dr. William Devenport, Committee Member
Dr. Wing Ng, Committee Member
Dr. Joseph Wang, Committee Member

July 25, 2007
Blacksburg, Virginia

Keywords: Scramjet, Mixing, Vortex dynamics, Experimental Fluid Mechanics

# Investigations of Injectors for Scramjet Engines

by Luca Maddalena

## ABSTRACT

Three, coordinate experimental studies were undertakes. First, an experimental study of an aerodynamic ramp (aeroramp) injector was conducted at Virginia Tech. The aeroramp consisted of an array of two rows with two columns of flush-wall holes that induce vorticity and enhance mixing. The holes were spaced four diameters apart in the streamwise direction with two diameters transverse spacing between them. For comparison, a single-hole circular injector with the same area angled downstream at 30 degrees was also examined. Test conditions involved sonic injection of helium heated to 313 K, to safely simulate hydrogen into a Mach 4 air cross-stream with average Reynolds number $5.77 \cdot 10^7$ per meter at a jet to freestream momentum flux ratio of 2.1. Sampling probe measurements were utilized to determine the local helium concentration. Pitot and cone-static pressure probes and a diffuser thermocouple probe were employed to document the flow. The main results of this work was that the mixing efficiency value of this aeroramp design which was originally optimized at Mach 2.4 for hydrocarbon injectants was only slightly higher than that of the single-hole injector at these high Mach number flow conditions with a low molecular weight injectant. The mass-averaged total pressure loss parameter showed that the aero-ramp and single-hole injectors had the same overall losses. The natural extension of the investigation was then to look in detail at two major physical phenomena that occur in a complex injector design such the aeroamp as well as in Scramjet combustors in general: the jet-shock interaction and the interaction of the vortical structures produced by the jets injection into a supersonic cross flow with an added axial vortex. Experimental studies were performed to investigate the effects of impinging shocks on injection of heated helium into a Mach 4 crossflow. Helium concentration, Pitot pressure, total temperature and cone-static measurements were taken during the mixing studies. It was found that the addition of a shock behind gaseous injection into a Mach 4 crossflow enhances mixing only if the shock is closer to the injection point where the counter-rotating vortex pair (always associated with transverse injection in a crossflow) is not yet formed, and the deposition of baroclinic generated of vorticity is the

highest. The final investigation was concerned with the interaction of the usual vortex structure produced by jet injection into a supersonic crossflow and an additional axial vortex typical of those that might be produced by the inlet of a scramjet or the forebody of a vehicle to be controlled by jet interaction phenomena. The cases treated are for sonic, heated Helium injection from a circular jet inclined at 30 degrees to a Mach 4 flow at high Reynolds number conditions. The additional axial vortices were generated by a strut-mounted, diamond cross-section wing mounted upstream of the injection location.The wing was designed to produce a tip vortex of a strength comparable to that of one of the typical counter-rotating vortex pair (CVP) found in the plume of a jet in a crossflow. For this purpose a separate study of the detailed vortex structure produced by jet injection into a supersonic crossflow was conducted. The profound interaction of supersonic vortices supported by a quantitative description and characterization of the flowfield was been demonstrated. The results show an higher value of the helium maximum concentration in all the cases investigated, but also higher penetration with a wider fuel plume compared to the case without a vortex. The decrease in mixing is attributed to severe disruption of the usual counter-rotating vortex pair in a jet plume.

# Acknowledgements

First and foremost, I would like to acknowledge my father Giuseppe, my mother Mirella, and my sister Sara. Without their love and encouragement, I could have never finished this study. They have always believed in me and gave their emotional support at difficult times.

I had the privilege of working with exceptionally good people in my PhD study. Their extensive knowledge, experience, and encouragement played an important role in the success of this project. I am grateful to my advisor, Dr. Joseph Schetz, for his academic advise, support, and encouragement. I would like to thank for his help and guidance.

I would like also to thank my committee, Dr. Bruno, Dr. Devenport, Dr. Ng and Dr. Wang for playing active roles in my research development and for always being available for advice and questions.

Much deserved thanks goes to my research partner, Theresa Campioli. Im glad to have been able to share research efforts and time with you. You are a great person and great friend.

I would like to acknowledge the current and the former student members of the Scramjet Research Group: Aris Bonanos, Eric Marineau, AJ Rolling, Ryan Throckmorton, Peter Grossmann and Alexander Duchmann. It was a great pleasure to work with them.

My thanks also go out to my friend Steve Edwards for his knowledge of electronics and operation of the supersonic wind tunnel lab and compressor. Without his knowledge of the wind tunnel facility and LabView, I doubt that anything would have run. I would also like to thank the AOE Machine shop staff, Bruce Stanger and James Lambert, for their involvement in the design and fabrication of various devices throughout the years at Virginia Tech.

# Contents

# List of Figures

# List of Tables

# Nomenclature

$A$ = cross-sectional area
$A_u$ = area of an isentropically expanded jet with a static pressure equal to that of the freestream
$a$ = gas analyzer calibration constant
$\alpha$ = mass fraction
$\alpha_{max}$ = maximum helium mass fraction
$b$ = gas analyzer calibration constant
$C_d$ = discharge coefficient
$C^*$ = critical flow function
$C_p$ = constant pressure specific heat
$C_v$ = constant volume specific heat
$C_{DN}$ = similarity law constant
$d$ = diameter
$d_{eff}$ = effective jet diameter
$d_{eq}$ = equivalent jet diameter
$D_N$ = cone's flat nose diameter
$f$ = hydrogen-air stoichiometric mass fraction, 0.0292
$\mathbb{M}$ = molecular weight
$X$ = molar fraction
$K_1$ = similarity parameter
$K_3$ = similarity parameter
$I$ = hot-film current
$l$ = active length of the hot-film sensor
$\dot{m}$ = mass flow rate
$\Pi$ = total pressure loss parameter

$\kappa$ = thermal conductivity
$N_u$ = Nusselt number
$\mu$ = viscosity
$\bar{q}$ = jet-to-free-stream momentum flux ratio
$R$ = specific gas constant
$\mathbb{R}$ = universal gas constant
$R_f$ = hot-film resistance
$R_s$ = series bridge resistance
$P$ = pressure
$q$ = heat flux
$M$ = Mach number
$Re$ = Reynolds number
$u$ = flow velocity
$V$ = voltage
$x$ = axial distance downstream of injector center
$y$ = lateral distance from the injector centerline
$t$ = time
$z$ = vertical distance from the wall
$z^+$ = plume center of mass
$y^\pm$ = plume width
$T$ = temperature
$\delta_c$ = cone angle
$\gamma$ = ratio of specific heats
$\eta_m$ = mixing efficiency
$C_{p\xi}$ = roll coefficient
$C_{p\eta}$ = pitch coefficient
$\theta$ = pitch angle
$\phi$ = roll angle
$\Gamma$ = circulation
$\omega$ = vorticity
$\Omega$ = hyperbolic length
$\rho$ = density

## Subscripts

| | |
|---|---|
| $c$ | = cone |
| $j$ | = jet-exit property |
| $t$ | = total condition |
| $He$ | = helium property |
| $air$ | = air property |
| $f$ | = hot-film |
| $\infty$ | = freestream property |
| $AV$ | = average of the four peripheral cone pressures |

# Chapter 1

# Introduction

## 1.1 Background

Since Yeager's breaking of the sound barrier in 1947 the desire to fly faster and higher has shaped the history or aeronautics. Revolutionary engine technology is being developed with the potential to fly at high Mach numbers and integrate atmospheric and space operations. The supersonic combustion ramjet, commonly referred to as scramjet, uses no rotating parts and can power vehicles at hypersonic speeds in the athomsphere, making rapid, global travel and affordable access to space a reality. Scramjet engine research has a long development history. From the 1960s through today, many programs have had the objective of developing and demonstrating hydrogen and hydrocarbon-fueled scramjet engines. A comprehensive look into advances in ramjet propulsion technology from subsonic to supersonic speeds since the early 1900s is provided by Fry.[1] The NASP (National Aero-Space Plane) program (USA) established in 1986 to develop and fly an integrated low speed booster, ramjet and scramjet propulsion system is recognized as the most influential program in modern scramjet development. Designed to operate on hydrogen fuel the X-30 was developed intensively over the years of the NASP program. This engine, while significantly modified by NASA, was used as the foundation for power plant of the NASA X-43 vehicle.

The first flight test of a hypersonic vehicle at mach 5.35 was conducted in Russia in late 1991. The vehicle operated as a dual-mode scramjet engine demonstrating both subsonic and supersonic combustion. A joint venture between Russia and France produced three

more flight tests. The second held in 1995 reportedly achieved supersonic combustion conditions at Mach 5.6 and the third test failed. University of Queensland (UQ) reported the development of a scramjet that achieved more thrust than drag in ground testing in 1993. UQ also led the international HyShot program which demonstrated the world's first supersonic combustion in an atmospheric flight test at Woomera on July 30, 2002, at speeds of more than Mach 8. Further international interest in scramjet technology was fuelled when NASA flew its X-43A scramjet-powered aircraft freely for the first time at a speed of Mach 7 on March 27, 2004, over the Pacific Ocean for 10 seconds and later at Mach 10 for 11 seconds in November of 2004.

Figure 1.1 is a representative schematic of a scramjet engine. The scramjet engine occupies the entire lower surface of the vehicle body. The inlet captures and compresses air for further progressing by the remaining components of the engine. Then, within the combustor chamber, the injected fuel is mixed and combusted into the supersonic air stream and lastly expanded through the nozzle. As a result of the very high freestream velocity of scramjets reaching Mach 10, fuel residence time is on the order of milliseconds and supersonic combustion presents an interesting challenge in scramjet engines. It is, therefore, desirable to enhance penetration and mixing of the fuel plume in order to accomplish rapid combustion leading to a reduction of the required combustor length, reducing the skin-friction drag and heat transfer and increasing the net thrust. To improve the overall engine efficiency, the injection process must also induce low total pressure losses.

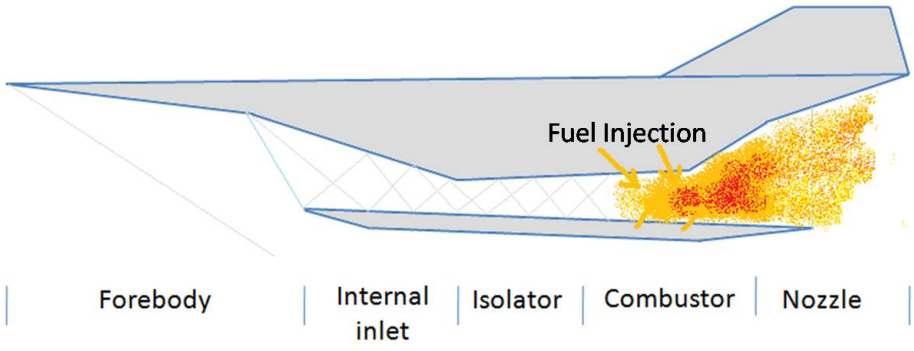


Figure 1.1: **Rapresentative Scramjet Engine**

## 1.2 Literature Survey

In order to state the problems associated with compressible turbulent mixing a review of the current understanding of the physics underlying the process of will be presented. Several injection configurations have been tested over the years in the attempt to enhance mixing through various physical means, such a production of vorticity and acoustic excitation . A brief overview of the most common injection systems will be then be discussed.

## 1.3 Compressible Turbulent Mixing Layers

The majority of fundamental studies of compressible turbulent mixing have investigated two-dimensional mixing layers. This is largely because they do not exhibit the problem of mixing layer merging associated with three-dimensional flows. At the high Reynolds numbers of interest here and for Schmidt numbers which, if not large are not much smaller than unity, the shear layer growth rate $\delta/x$ is an important quantity. The transverse extent $\delta/x$ of the shear layer is known to depend on the dimensionless parameters of the flow:

$$r = \frac{U_2}{U_1} \tag{1.1}$$

And

$$s = \frac{\rho_2}{\rho_1} \tag{1.2}$$

Brown and Roshko[2] postulated that the density effect was due to differing diffusion rates of mass and momentum.

It is well established that the growth rates of compressible turbulent mixing layers diminish as the flow Mach number increases, and are generally lower than those observed in incompressible mixing layers with the same velocity and density ratios. Dimotakis[3] summarizes most of this work. In their experimental work Brown and Roshko were able to prove that the reduced growth rates found in compressible flows could not be attributed merely to the density ratio, but were largely due to compressibility. In addition,

their Schlieren pictures of the two-dimensional mixing layers revealed that a fundamental property of turbulent shear flow, related to its growth, is the phenomenon of *entrainment*, that is the incorporation of non-turbulent, usually irrotational fluid into the turbulent region or, conversely, the diffusion of the turbulent region into the ambient flow.

Recent experimental investigations of compressible shear layers by Papamoschou and Roshko[4] and others, have suggested that the effects of compressibility are scaled by the convective Mach numbers with respect to the two streams, which measure the relative free stream Mach numbers as seen not from the laboratory reference frame but from the Galilean frame of the large scale structures in the layer. This is the Mach number at which structures in the mixing layer move with respect to the two mixing steams, defined as:

$$M_{c,1} = \frac{U_1 - U_c}{a_1} \tag{1.3}$$

$$M_{c,2} = \frac{U_c - U_2}{a_2} \tag{1.4}$$

Where $a$ is the speed of sound and the subscript $c$ stands for "convective".

Papamoschou and Roshko found that the compressible shear layer growth rate, when normalized by the corresponding incompressible flow growth rate estimated at the same velocity and density ratio, is only a function of the convective Mach number,

$$\frac{\delta}{\delta'} = \frac{\frac{\delta}{x}(r, s, M_{c,1})}{\frac{\delta}{x}(r, s, M_{c,1} = 0)} \tag{1.5}$$

When this non-dimensional growth rate, calculated using the same velocity and density ratio, is plotted against $M_c$, a trend is revealed. The value of $\delta/\delta'$ drops from unity for $M_c < 0.3$ to a small constant value for $M_c > 1$ that appears to asymptote to a value roughly 20% of its incompressible value. This phenomenon clearly shows the challenge of an efficient supersonic mixing.

Some plausible explanations for this reduced mixing rates are now presented. A detailed discussion can be found in Morkovin.[5] The observed reduced turbulence and smaller growth rates observed from the experimental results can be the consequence of the fact

that these mixing layers extract less energy from the mean flow due to the compressibility effect. As first pointed by Papamoschou,[6] the zone of influence of a point in the mixing layer decreases as the convective Mach number increases. The streamwise and cross-stream communication necessary for the Kelvin-Helmholtz instability to grow is inhibited. As $M_c$ tends to 1, the center of the mixing layer can no longer communicate with the edges of the mixing layer itself. The reduction of the amplification rate of the Kelvin-Helmholtz instabilities at these higher convective Mach numbers is somewhat ameliorated by the existence of swept structures.
The effective convective Mach number of these structures is reduced by this sweepback, thus increasing their amplification rates. This result suggests that in the limit case of swept structures as in streamwise vortices, the convective Mach number should have little effect, and thus their contribution to mixing should remain unchanged. Therefore, the three-dimensionality should have a positive effect on the mixing-layer as $M_c$ increases.

## 1.4 Mixing Enhancement Techniques

### 1.4.1 Swirling base injection

As a result of the increased mixing-layer growth rates found in low speed swirling flows, several studies were initiated to investigate the effect of swirl on compressible mixing. The results of the relevant studies of this concept are summarized. It has been indicated in the previous paragraph that the compressibility effect should have a negligible effect on a streamwise vortex. The technique of adding a swirl to a jet creating a streamwise vortex was first suggested by Swithenbank and Chigier .[7] In response to this suggestion, Povinelli and Ehlers ,[8] examined sonic parallel injection, with and without swirl, into a M=2.7 air flow. In a similar study, Schetz and Swanson [9] studied coaxial injection into a M=3.5 freestream. Both studies concluded that the addition of swirl to a compressible flow did not enhance mixing.

On the other hand, several and recent studies of compressible mixing layers, indicated that swirling does enhance mixing. Naughton et al[10]investigated a M=3.0 air vortex injected into a $M = 3.5$ co-flowing stream. The addition of swirl in the flow increased mass entrainment by 30%. Cutler and Levey[11] and Levey[12] indicated that swirling flows

exhibited higher mixing-layer growth rates than that of the non-swirling flow. In addition, the amount of enhancement scaled with the degree of swirl. Naughton et al.[13] tried to quantify the growth rates of the mixing layers and to quantify the strengths of the supersonic streamwise vortices generated. He was able to vary the convective Mach number and the amount of swirl independently. The results of these surveys indicated that vortices of significant strength, with swirl numbers up to 0.10, were produced. By comparing these measured growth rates with the vortex strength, it was observed that the addition of swirl significantly increased mixing-layer growth rate and that this mixing enhancement scaled with the vortex strength and appeared to be independent of the convective Mach number. Although the degree of enhancement was less than that found by Levey,[12] the results of the two studies qualitatively agree and they are in contradiction with the results of Povinelli[8] and Schetz[9] previously mentioned.

### 1.4.2 Ramp Injectors

Ramp injectors have been widely studied for supersonic combustion applications. Numerous investigations have looked at wall ramp injectors as a viable means of providing enhanced fuel-air mixing ( Davis,[14] Northam,[15] Waitz,[16] Hartfield,[17] Riggins[18]). The ramp provides vortex shedding off the edges and a local separation at the base. This recirculation zone provides flameholding similar to a reward-facing step.

The fuel is injected through the base and into the counter-rotating vortex pair. Various ramp injectors' geometries have been studied in supersonic combustors. Northam[15] found higher combustion efficiencies with swept ramps (respect to an unswept ramp) and mixing performance similar to that of tangential injection. Stouffer[19] found that ignition in expansion ramps has a longer delay, but once started, the dynamic (i.e. the overall combustion efficiency) is higher than with compression ramps, leading to a smaller length of the combustor. The drawbacks of this design arise from the intrusive nature of the injector itself and the fact that they highly depend on maintaining their geometry intact. Interaction with the supersonic, high-enthalpy freestream, has the disadvantage of pressure losses and added drag. In addition, this also create hot spots which increase thermal loads on the system often exceeding the thermal limits of most practical material.

### 1.4.3 Aerodynamic Ramp Injector

In order to address the problems encountered in the description of the ramp injector and thus reduce the pressure and thermal losses associated with this injector, a new aerodynamic ramp injector was introduced. The aerodynamic ramp or simply aero-ramp injector concept is credited to Schetz.[20]
This injector design consisted of a three-by-three array of closely spaced, flush-wall jets with various transverse and yaw angles. The jets were arranged in order to generate multiple interactions which should lead to enhanced mixing.

These fuel-vortex interactions were to include skew-induced vortex generation, shock induced vortex generation, and vortex breakdown, all of which have been shown to be effective mixing enhancement mechanisms. In addition, the flush-wall design coupled with low angle injection avoids the excessive pressure losses usually associated with intrusive devices. Fuller at al.[21] investigated in detail the aeroramp performance. They found that increasing the jet-to-freestream momentum flux ratio from 1 to 2 significantly increased the performance of the aeroramp, whereas in a physical ramp arrangement the performance hardly changed. The aeroramp exhibited lower pressure losses than the physical ramp. The development of this injector model was carried further and a series of studies were made to study injector spacing, yaw and other parameters (Cox-Stouffer[22]). Jacobsen et al.[23] reported on the effect of injector toe-in angle using a simpler 3-hole aeroramp arrangement. From this investigation emerged that moderate toe-in angle (between 15 and 30 degrees) increases the penetration respect to the case with 0 degree angle. Jacobsen et al[24] also investigated the effect of jet swirl on the mixing and confirmed the positive effect on mixing. With a new 4-hole aeroramp injector, Jacobsen et al[25] showed that in a Mach 2.4 crossflow better mixing was achieved respect to a single-hole injector with the price of a slightly higher pressure losses and lower penetration.

### 1.4.4 Cavity Enhanced Mixing

Researchers have suggested that cavity flow oscillations can actually be used to provide enhanced mixing in supersonic shear layers. A shear layer develops instability waves in its initial region. This long wavelength Kelvin-Helmholtz instability which leads to large rollers are suppressed at high convective Mach numbers. Cavity flows can be categorized

into two basic flow regimes depending on the effect of the parameter $L/D$ (length-to-depth ratio). For $L/D < 10$, an open cavity, the shear layer formed at the separation corner spans the entire length of the cavity and reattaches along the cavity back face. Cavities, depending again on $L/D$, have two operational modes. Small aspect ratio cavities ($L/D < 2-3$) are responsible for a transverse oscillation mechanism, whereas in larger aspect ratio cavities, longitudinal modes become the dominant mechanism. When $L/D > 10$, a closed cavity, the shear layer reattaches to the floor resulting in a larger drag. Thus, these configurations are not favorite for scramjet applications, (Gruber[26]). An extensive overview of research on cavities is given by Ben-Yakar.[27]

### 1.4.5 Transverse Jet Injection

The subject of transverse injection of a gas into a supersonic main flow has been studied extensively.[28–31] A comprehensive review of the mixing of transverse jets and wall jets in supersonic flow including a substantial list of a references to earlier work has been presented by Schetz et al.[32]

The jet-free stream interaction produces a 3-D bow shock that in turn causes the upstream wall boundary layer to separate, providing a region where the boundary layer and the jet fluids mix subsonically upstream of the jet exit. Ben-Yakar[33] proposed the use of these recirculation regions as flame holders, however she admitted that other injector types would be more suitable for such use. The experimental studies performed by Fric and Roshko[34] of a jet injected in low-speed crossflow, illustrate four types of coherent structures: (1) The near-field jet-layer vortices; (2) the far field counter rotating vortex pair (CVP); (3) the horseshoe vortex which wraps around the jet column and (4) the downstream wake vortices originated from the horseshoe vortex. The origin of the jet vortical structure studied by Yuan et al.[35]revealed that the majority of the jet vortical structures arose from the Kelvin Helmholtz (K-H) instability of the jet-shear layer in the near field. They found that two kind of vortices originated from the jet exit boundary layer : (1) quasi-steady vortices that form in the skewed mixing layers (mixing layers formed from non-parallel streams) on each lateral edge of the jet leading to the formation of the CVP, and (2) regularly formed spanwise rollers on the upstream and downstream edges (large scale jet shear layer vortices) which dominate the near field mixing by the so called entrainment-stretching-mixing process.

## 1.5 Shock-Enhancement Mixing

One mixing enhancement strategy at hyper-velocities is the shock-enhancement mixing mechanism, in which the interaction between the mixing layer and an oblique shock creates strong axial vortices that stretch the fuel-air interface. Of course, scramjet combustors generally are well-populated with shock waves in any case. The interaction of a mixing layer composed of a light fluid accelerating in a heavy fluid with an oblique shock wave induces a misalignment between the density gradient in the mixing layer and the pressure gradient of the shock wave. This misalignment creates instability in the fluid interface and then turbulent mixing. Numerous investigations have looked at this mechanism as a viable means of providing enhanced fuel-air mixing(Gruber et al.,[26] Lee et al.,[36] Obata and Hemarson,[37]Smart an Kalhoran[38] ,Cattafesta and Settles,[39] Foster,[40] Menon and Martens[41]). Marble[42] et al and his exploratory study and observations based on shock tube investigations of the distortion and mixing induced by shock waves impinging on a cylindrical column of hydrogen embedded in air in conjunction with the subsequent work of Yang[43] will be reviewed and used to explain part of the results in Chapter 6.

## 1.6 Contribution of the Current Study

Due to the short fuel residence time inside a scramjet, which is on the order of a millisecond, achieving efficient supersonic combustion forms a challenging problem. Enhanced mixing and rapid combustion imply an increase in combustion efficiency and a reduction of the combustor length, thus reducing the skin-friction drag and increasing the net thrust. For cycle efficiency purposes, the process must also induce low total pressure losses. Mixing enhancement in high-speed flows also has application in a number of other fields such as thermal protection systems and vehicle control by jet thrusters.

The present investigation starts with the study of an aeroramp injector in a Mach 4 crossflow. The interpretation of the results leads to a natural extension of the investigation with the purpose to examine in detail two major physical phenomena that occur in a complex injector design such the aeroamp. The first is jet-shock interaction. The second topic is the interaction of the vortical structures that normally occur in scramjet combustors with those produced in the jet plume by jet injection into a supersonic cross

flow.

## 1.7 Outline of the Dissertation

This chapter has provided the background and motivation underlying this study.

Chapter 2 presents the experimental facilities and Chapter 3 the techniques employed. Chapter 4 covers the data-reduction process. Chapter 5 documents the effectiveness of the specific aeroramp injector design, initially proposed by Jacobsen[24] for ethylene injection into a M = 2.4 flow, now for hydrogen injection into a Mach 4 flow with heated helium used to simulate hydrogen fuel. The aim of Chapter 6 is to examine the interaction between a planar shock wave and a transverse jet of a light gas in a Mach 4 air crossflow. Chapter 7 is concerned with the interaction of the usual vortex structure produced by jet injection into a supersonic crossflow and an additional axial vortex typical of those that might be produced by the inlet of a scramjet or the forebody of a vehicle to be controlled by jet interaction phenomena. Finally, conclusions based on these results are given in Chapter 8.

# Chapter 2

# Experimental Facilities and Hardware

## 2.1 Test Facilities

Two separate test facilities, the supersonic wind tunnel (SST) and the supersonic free-jet facility (FJF), where used in this study. All mixing experiments were carried out in the SST, while the FJF was designed and used for the five-hole probe calibration.

### 2.1.1 Supersonic Wind Tunnel

Experiments were conducted in the Virginia Polytechnic Institute and State University unheated, blow-down supersonic wind tunnel with test section measuring 23 cm wide by 23 cm high and 30 cm long. A schematic of the wind tunnel nozzle and test section is shown in Fig. 1. The tunnel was configured with a convergent-divergent nozzle resulting in a nominal freestream Mach number of 4.

An Ingersoll-Rand, type HHE, four stage, water cooled compressor is used to compress the air supply which is then piped first through a dryer to remove moisture, then a separator to remove any oil. After the drying and filtering is completed, the air is stored in two tanks with a total volume of $23m^3$. During a tunnel run, the air is released from the tanks to the tunnel settling chamber by a computer-controlled pneumatic butterfly valve.

The tunnel digital PID feedback control is capable to maintain the nominal pressure with an accuracy of $\pm 1\%$.

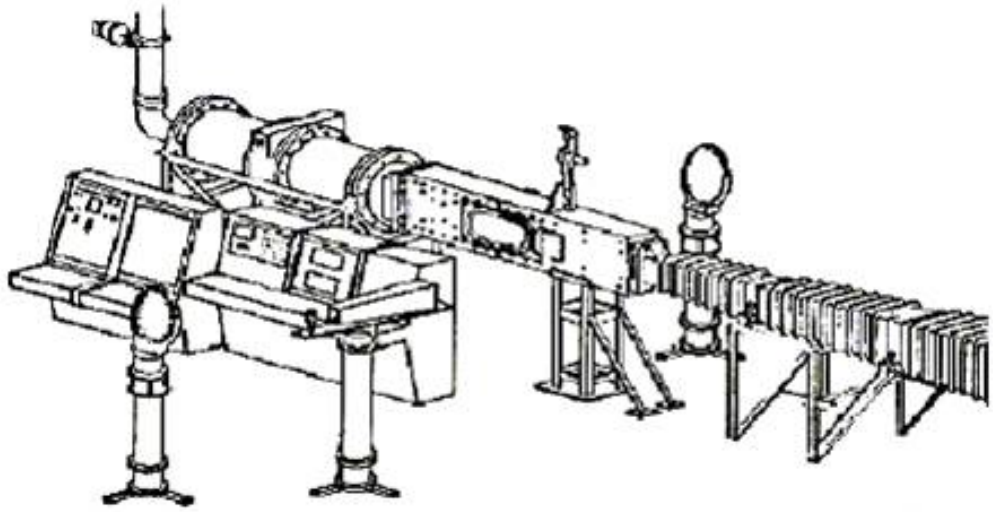

Figure 2.1: **Virginia Tech supersonic wind tunnel**

The boundary layer on the bottom wall of the Supersonic Wind Tunnel operating at a nominal free stream Mach number of 4 was investigated in order to characterize the freestream conditions.

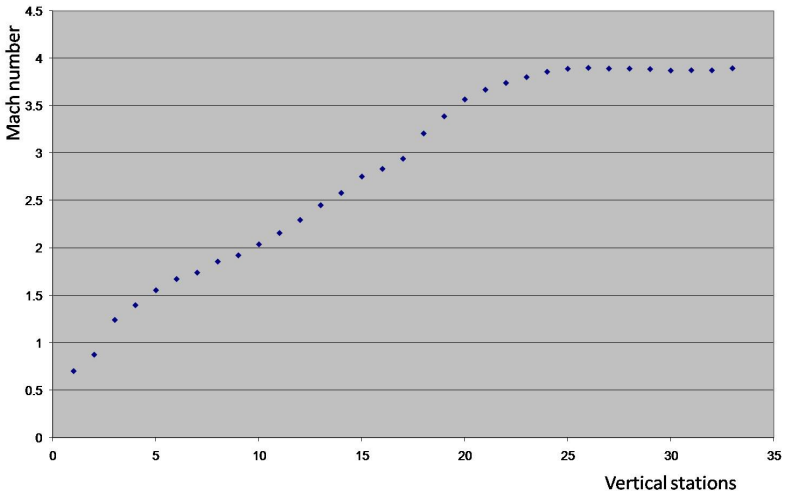


Figure 2.2: **Boundary layer profile (M=4 test section)**

An automated traverse system moved a measurement probe (refer to Chapter 3) up through the boundary layer, and the control computer recorded temperature and pressure data. These data in terms of Mach number and traverse incremental position are presented in Figure 2.2. The resulting boundary layer thickness at the measurement station is $18mm$.

### 2.1.2 Free-Jet facility

The other facility used in this study, the free-jet facility is shown in Figure 2.3. The facility was designed as part of the current program in order to perform a full calibration of the five-hole probe. The schematic is presented in Figure 2.4, and the details of the nozzle are in Figure 2.5. The air from the tank ( 300 psi ) is reduced by a valve to the specific level at which the overexpanded nozzle was set to work (180 psi). The M=3.1 nozzle was design with MOC (Method of Characteristics), and the plenum pressure (180 psi) was chosen based on the maximum pressure admissible by the miniature pressure transducers of the five-hole probe (50 psi, differential). The mass flow rate of the nozzle at the design plenum pressure, is the same produced by the compressor. If the compressor is left on during the run, the free-jet facility can operate continuously.

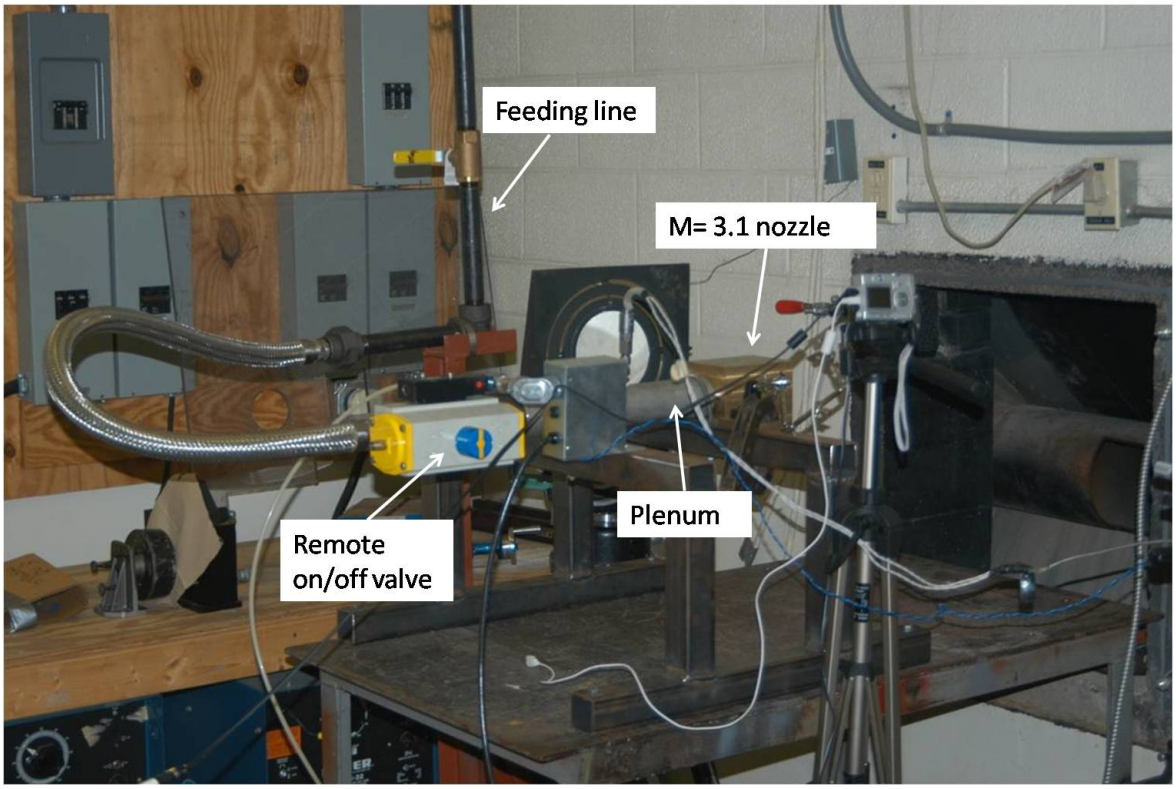


Figure 2.3: **Free-jet facility**

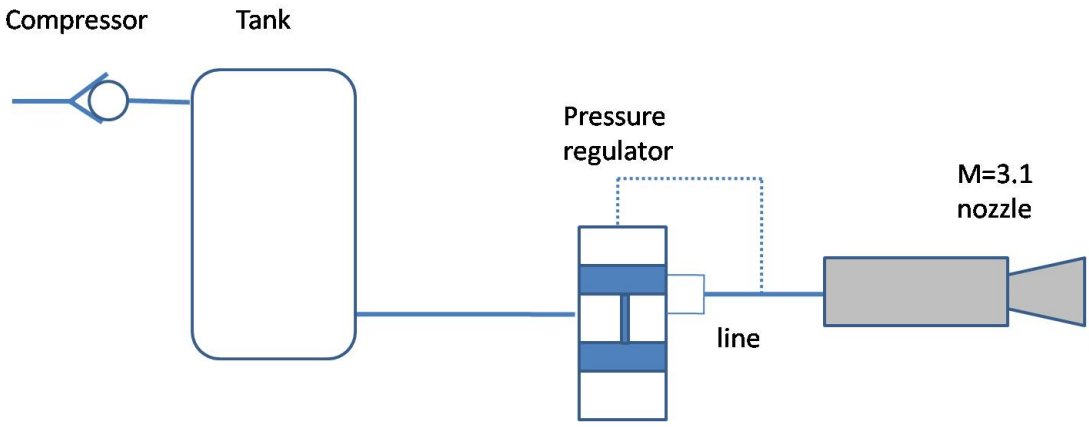


Figure 2.4: **Schematic of free-jet facility plant**

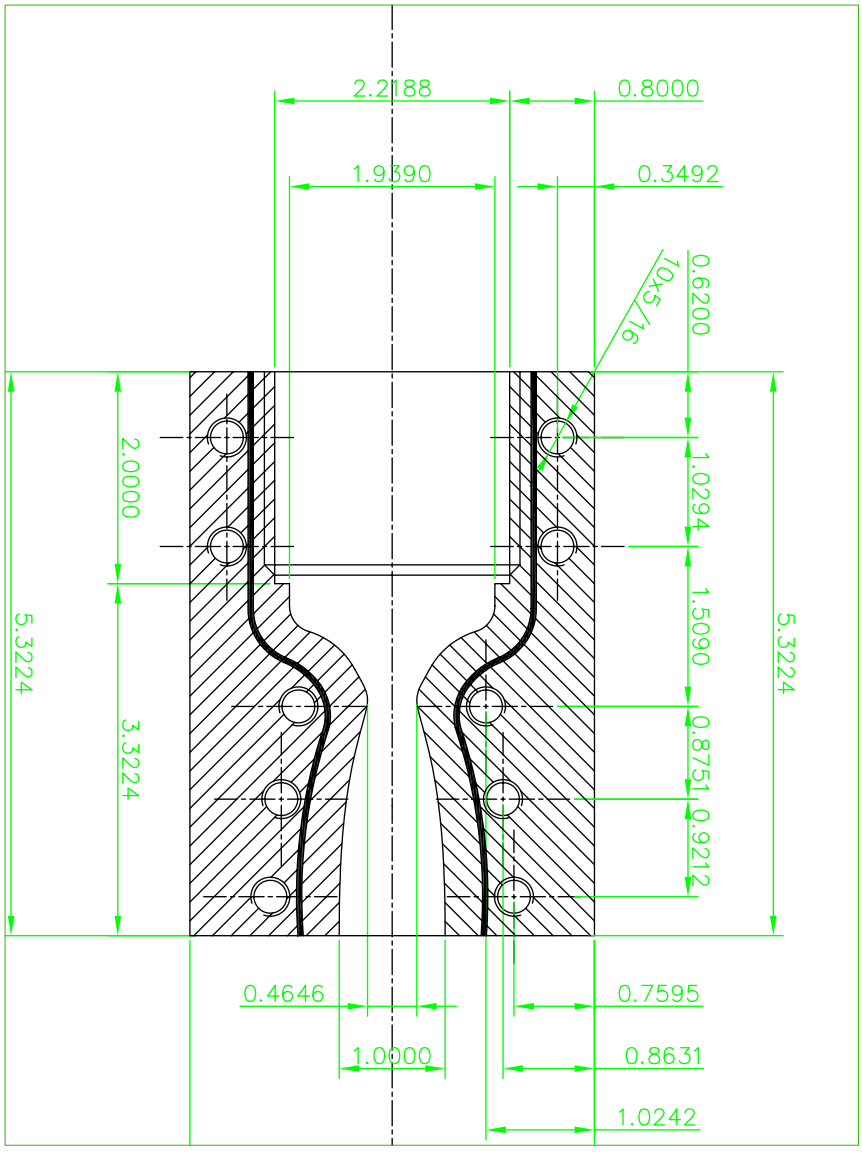


Figure 2.5: **Free-jet facility nozzle details**

## 2.2 Test Hardware

The following session discusses the injectors, the hardware used to generate the shock to examine the interaction between a planar shock wave and transverse jet, and the vortex generator for the studies of streamwise vortices interaction.

### 2.2.1 Injectors

Figures 2.7 to 2.10 show the two injector model inserts used in the present investigation. The top surface of the inserts is flush with the tunnel wall. The aeroramp injector (Figure 2.7 and Figure 2.8) had four holes, each one with a diameter $d_j$ of 1.61 mm and a corresponding equivalent jet diameter $d_{eq} = (A_j/p)^{0.5}$of 3.23 mm. The geometry consisted of two rows of two round holes, spaced 4 equivalent diameters, in the streamwise direction and 2 equivalent diameters between the holes. The first and second pair of injector holes had transverse-injection and toe-in angles of 20 and 40 deg and 15 and 30 degrees, respectively. This is the same aeroramp injector optimized by Jacobsen[24] for higher molecular weight ( $\mathbb{M} \approx 30$) injectants in a Mach 2.4 airstream. The single-hole (Figure 2.9 and Figure 2.10 ), circular injector used as a comparator had the same equivalent diameter ( $d_{eq} = 3.23mm$) and was transversely angled 30 deg relative to the downstream direction on the test section floor.

### 2.2.2 Shock

A two-dimensional shock generator (Figure 2.16) was used to generate a shock of 20 degrees which was impinged upon the jet at a series of stations downstream of the injection point. The wedge has an included angle of 12 degrees, and it is 8 inches wide at the leading edge. The Shock generator and its use will be discussed in further detail in Chapter 6.

### 2.2.3 Vortex generator

A vortex generator was designed for the studies of supersonic vortices interaction (Chapter 7). A diagram of the vortex generator mounted in the wind tunnel is shown in

Figure 2.11, while a picture of the vortex generator is shown in Figure 2.12. It consists of a straight half wing with a modified double-wedge airfoil section. It has a chord of 2 inches, a thickness of 0.21 inches and a span of 3.5 inches. The wing was designed to produce a vortex with circulation $\Gamma$ of the order of $1.9m/s^2$ The motivation behind this choice will be clear in Chapter 7. Figures 2.13 to 2.15 show the detailed drawings.

## 2.3 Test Matrix

All wind tunnel tests were performed at a nominal free-stream Mach number of 4.0. Free stream conditions were fixed at a total pressure of 1034 kPa with an ambient mean total temperature of approximately 295 K, producing a freestream Reynolds number of $5.77 \cdot 10^7$ per meter. These conditions resulted in a turbulent boundary layer with a thickness of approximately 20 mm at the point of injection.
A weak shock at the junction of the tunnel nozzle and the test section plate resulted in a Mach number of 3.8 at the injection station. Heated helium (in order to achieve temperature profiles analogous to the concentration) was used as the injectant to simulate hydrogen fuel. The injectant was heated to an average total temperature of 313K, and the average injection Mach number was sonic. The jet-to-freestream momentum flux ratio, , was set to 2.1. Recall that is defined by

$$\bar{q} = \frac{(\rho u^2)_j}{(\rho u^2)_\infty} \tag{2.1}$$

A Cartesian coordinate system was chosen with the origin on the wall surface along the test section centerline, as shown in Figure 2.6

The origin of the coordinate system is located on the wall in the middle of the injector array or single injector. The positive x-axis is in the free stream direction, the positive z-axis is in the vertical direction perpendicular to the wall, and the y-axis spans the test section.. All lengths are normalized by the effective diameter, $d_{eff}$, defined as:

$$d_{eff} = C_d^{0.5} d_{eq} \tag{2.2}$$

where $C_d$ is the injector discharge coefficient. The measured injector discharge coefficients

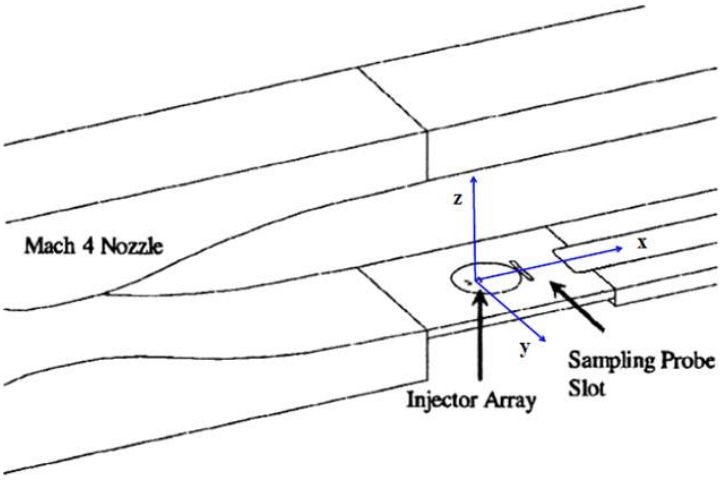


Figure 2.6: **Tunnel arrangement and coordinate system**

were 0.83 for the aeroramp and 0.88 for the single-hole injector. The equivalent jet diameter is defined as the diameter of a single circular orifice having the same area as the combined area of all four orifices. For the present aeroramp configuration, operating at$\bar{q} = 2.1$, the corresponding helium flow rate was 3.4 g/s. For better comparison, experiments were performed by maintaining the same injectant flow rate.

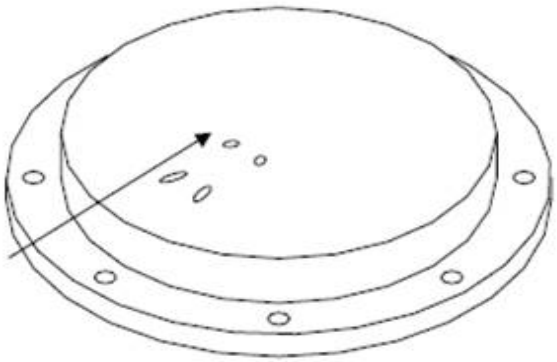

Figure 2.7: **Aeroramp injector**

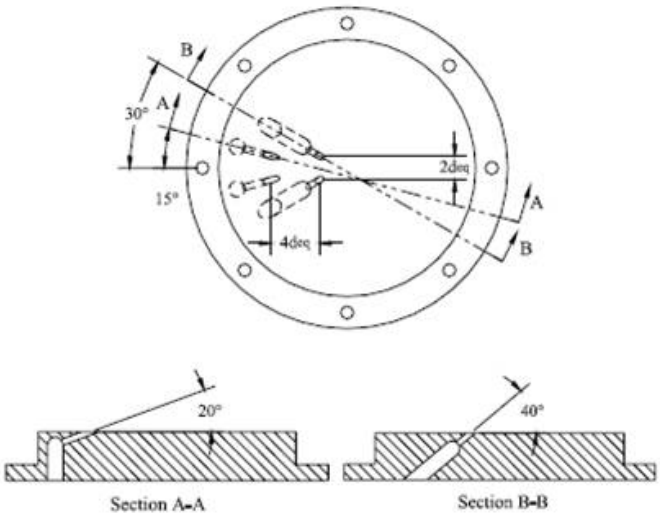


Figure 2.8: **Aeroramp injector. Section.**

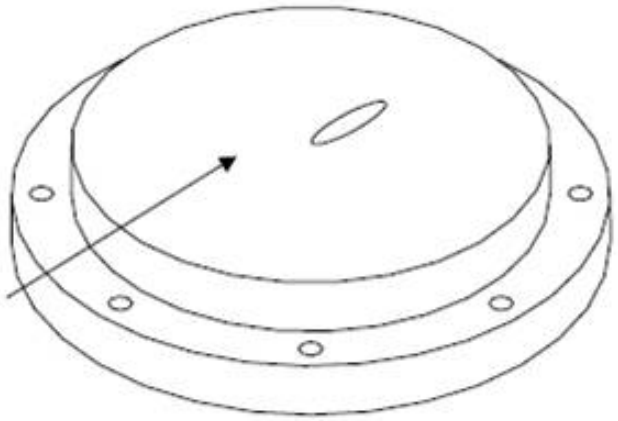

Figure 2.9: **Single-hole injector**

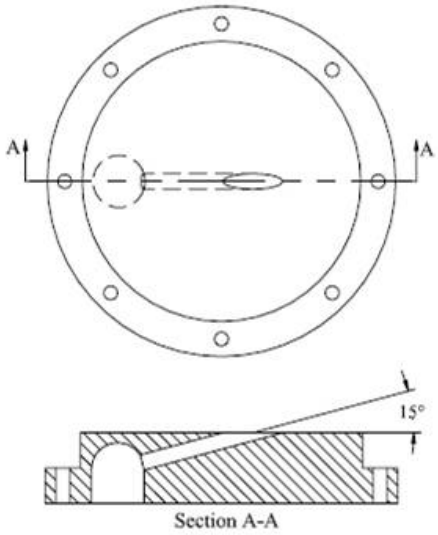


Figure 2.10: **Single-hole injector. Section.**

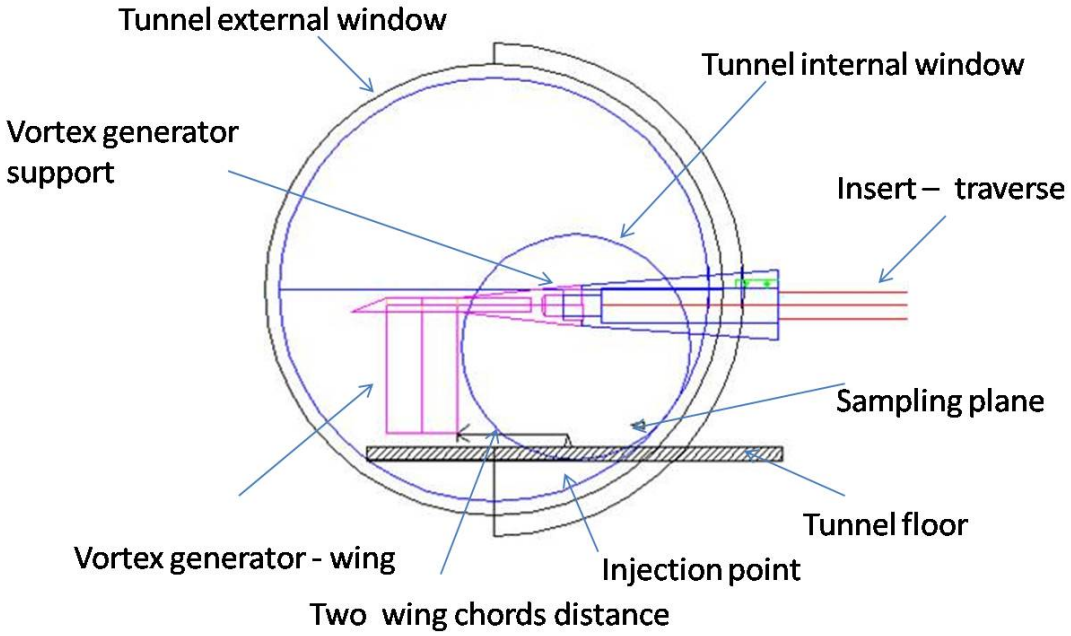


Figure 2.11: **Schematic of the vortex generator installed in the wind tunnel**

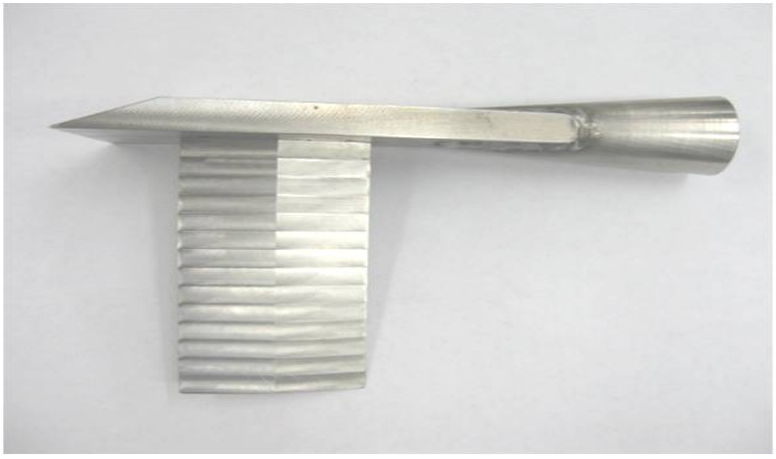

Figure 2.12: **Picture of the vortex generator outside the wind tunnel**

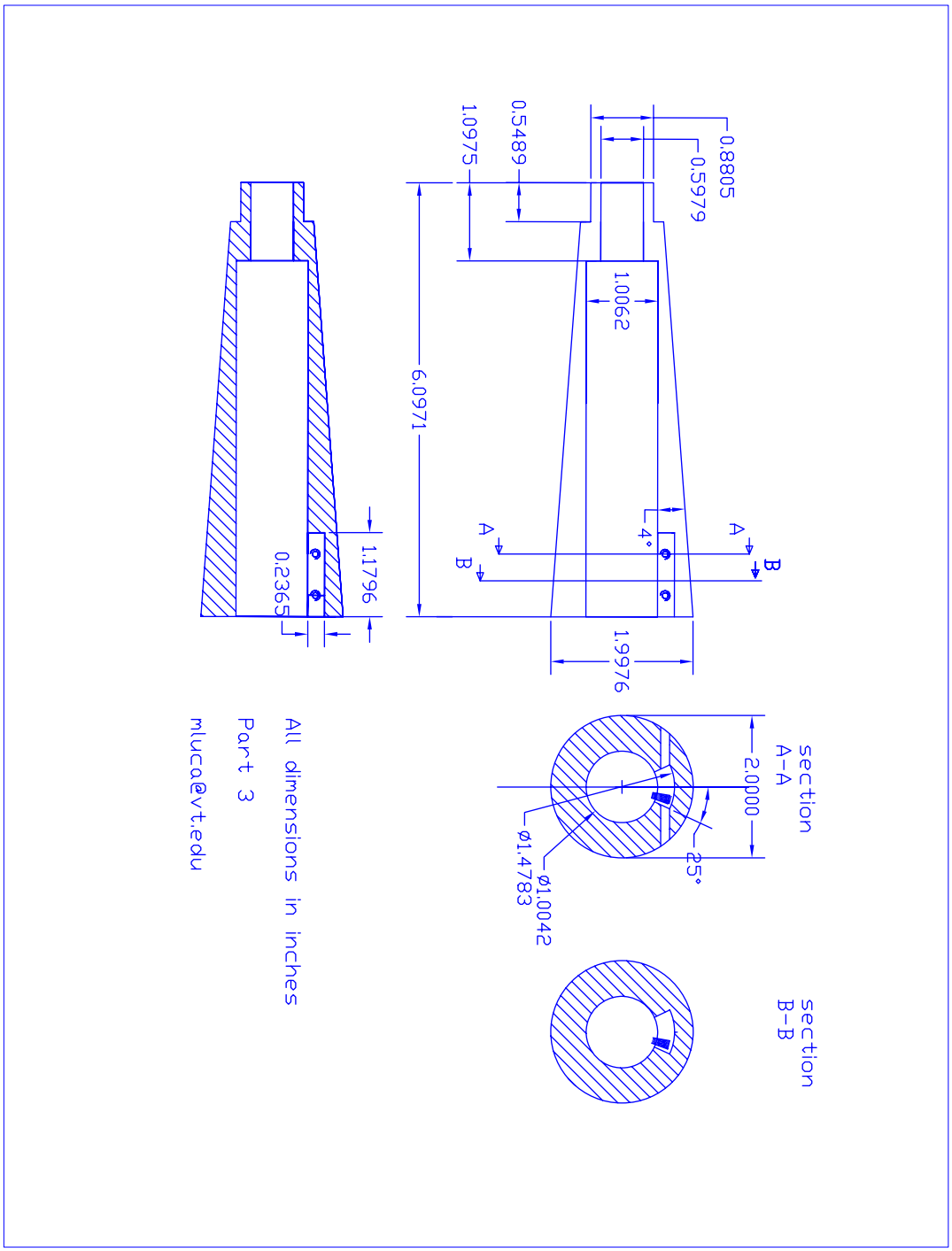


Figure 2.13: **Vortex generator support details**

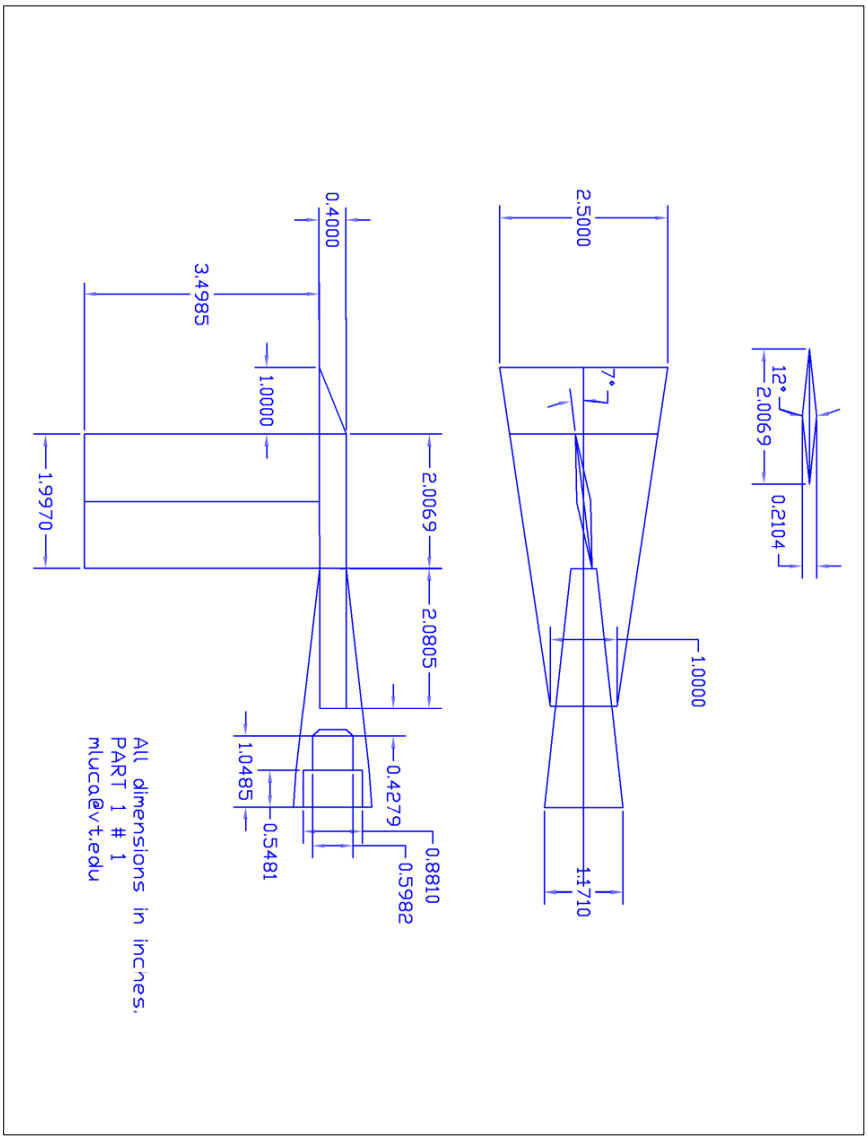


Figure 2.14: **Vortex generator details**

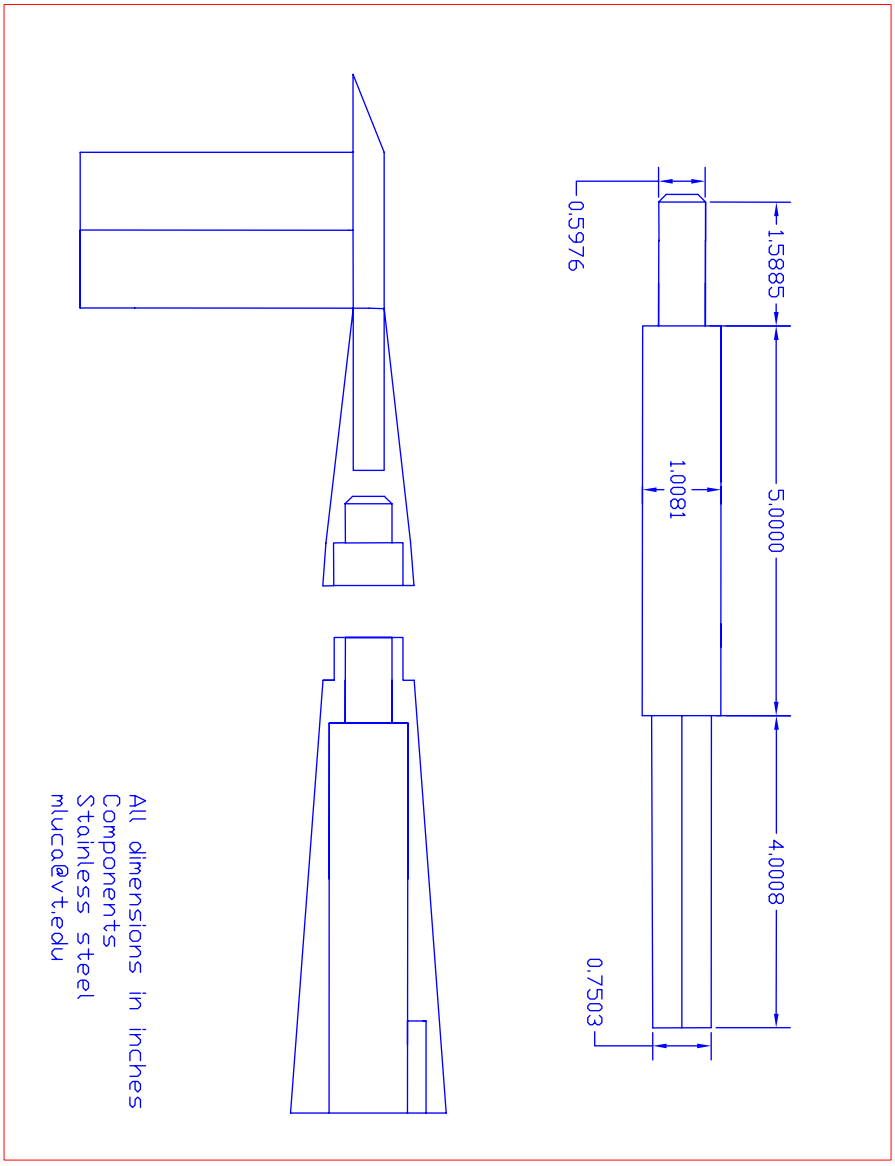


Figure 2.15: **Vortex generator assembly**

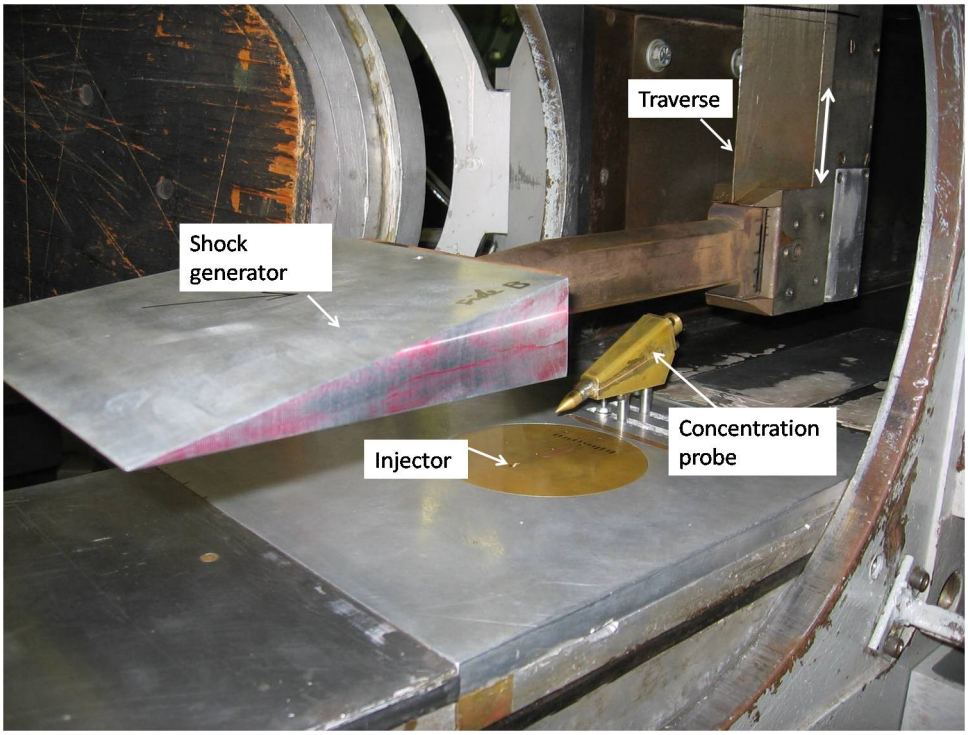


Figure 2.16: **Picture of the shock generator in the supersonic wind tunnel**

# Chapter 3

# Experimental Methods

To accomplish the experimental study, several measurement techniques were employed, including both intrusive flowfield surveys and non-intrusive optical diagnostics. The following sections discuss these techniques.

## 3.1 Gas Sampling

Since we are studying mixing, accurate gas composition measurement is critical. Mean species concentration measurements were obtained using an integrated sampling probe and gas analyzer designed specifically for use in supersonic flow. The fundamental concepts and design of this probe were developed at Virginia Tech by Prof. W. Ng and his students.[44] The concentration probe is an aspirating type attached to a vacuum pump. The unit consists of a constant temperature hot-film sensor operating in a channel with a choked exit. The housing was designed to fit around the body of a TSI 1210-50 platinum sensor. The hot film has a diameter of $50.8\mu m$ and an active sensor length of 1.02 mm, and was used in conjunction with a Dantec Type-56C17 constant temperature anemometer fitted with a DISA Type-56C01 CTA standard bridge. The overheat ratio is the ratio of the hot film resistance at operating temperature to its resistance at ambient temperature. For the current work, an overheat ratio of 1.24 was used. The probe is designed with a diverging channel between the tip and the sensor plane. The inlet hole at the tip of the probe has the same diameter as the choked orifice, d=0.63 mm. These

diameters are chosen so as to preclude the occurrence of a standoff shock at the probe tip. Flow visualization from spark schlieren verified this design intention. The internal probe diameter diverged from 0.63 mm at the inlet to 3.8 mm at the sensor plane, causing a normal shock to occur inside the probe in the diverging channel. In this fashion, a stream tube equal in area to the probe capture area can enter the probe undisturbed. The concentration probe was calibrated to measure the helium molar fraction uniquely related to a given pressure, temperature and rate of heat transfer sensed at the hot-film operating plane. The hot-film responds to local mass flux variations. The absolute measurement uncertainty in helium mass fraction was estimated to be approximately $\pm 7\%$. A photograph is given in Figure 3.1.

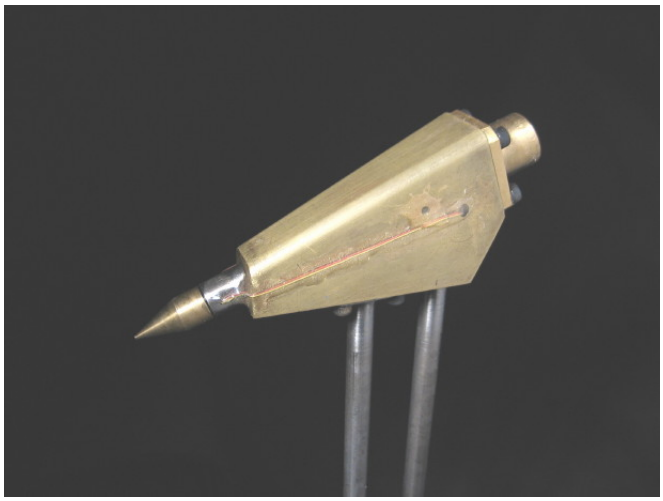

Figure 3.1: **The new concentration probe**

### 3.1.1 Principle of Operation

Figure 3.2 illustrates a schematic of the probe. (Refer to Appendix D for further details and the detailed drawings).

The sensor plane includes a thermocouple, pressure tap, and a hot film. The continuity of the mass flow can be expressed as

$$\rho u = P_t \sqrt{\frac{\gamma}{RT_t}} \left[1 + \frac{\gamma - 1}{2} M\right]^{-\frac{\gamma+1}{2(\gamma-1)}} \tag{3.1}$$

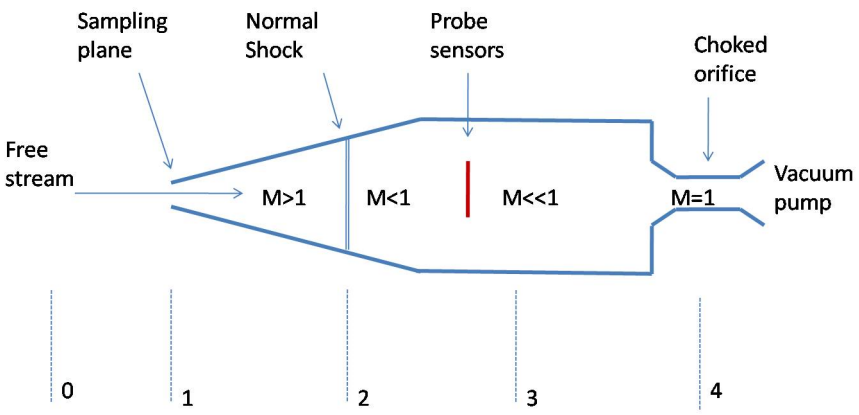


Figure 3.2: **Schematic of the concentration probe**

Which in case of choked orifice (throat) ($M = 1$) reduces to:

$$(\rho u)^* = \frac{P_t C^*}{\sqrt{T_t}} \tag{3.2}$$

Where $C^*$ denotes the critical ( sonic conditions , and designated with $*$) fluid function defined by

$$C^* = \sqrt{\frac{\gamma \mathbb{M}}{\mathbb{R}}} \left( \frac{2}{\gamma + 1} \right)^{\frac{\gamma+1}{2(\gamma-1)}} \tag{3.3}$$

In which $\mathbb{M}$ is the molecular weight, and $\mathbb{R}$ is the universal gas constant. From the continuity of the mass flow through the probe it is possible to relate the mass flux at the sensor plane in terms of the critical conditions, the sensor plane area, and the flow properties as:

$$\rho u = \frac{P_t C^*}{\sqrt{T_t}} \frac{A^*}{A_c} \tag{3.4}$$

Hence, since we measure the pressure, the temperature and the geometry is known, the mass flow is a function of the gas composition alone. The rate of heat transfer of the hot film in the measurement plane is given by:

$$q_f = I_f^2 R_f \tag{3.5}$$

Where $R_f$ is the film resistance and $I_f$ is the film current. The relation between the volt-

age response and the film current is, for a constant temperature anemometer, expressed as:

$$I_f = \frac{V}{R_f + R_s} \tag{3.6}$$

Where $R_s$ is the series bridge resistance. In order to relate the hot-film heat transfer rate to the difference between the film and the fluid temperatures, the Nusselt number is introduced as:

$$Nu = \frac{q_f}{\pi k l \left(T_f - T_t\right)} \tag{3.7}$$

Where $l$ is the active sensing length of the hot-film and $k$ is the thermal conductivity of the gas mixture. It is now possible to rewrite the Nusselt number as:

$$Nu = \left(\frac{R_f}{R_f + R_s^2}\right) \frac{V^2}{\pi k l \left(T_f - T_t\right)} \tag{3.8}$$

The Nusselt number can be formulated in terms of the Reynolds number (based on the diameter of the film, $d$) as:

$$Nu = a \left(\rho u \frac{d}{\mu}\right)^b \tag{3.9}$$

In this equation, $a$ and $b$ are empirically determined constants that depends only on the gas composition. The governing equation for the anemometer voltage response, combining Equation 3.8 and Equation 3.9, can be expressed as:

$$V^2 = \frac{\left(R_s + R_f\right)^2}{R_f} \pi l k a \left(\frac{d}{\mu} \frac{P_t}{\sqrt{T_t}} \frac{A^*}{A} C^*\right)^b \left(T_f - T_t\right) \tag{3.10}$$

In this equation, the parameters $C^*$, $k$, and $\mu$ are (as $a$ and $b$) properties of the gas mixture and therefore function of the helium concentration $\alpha_{He}$. Since the anemometer operates at constant temperature ( $T_f$) and therefore constant resistance it is possible to verify that Equation 3.10 can be written in a functional form as

$$V = f\left(P_t, T_t, X_{He}\right) \tag{3.11}$$

It is possible to recognize that for a given total pressure and total temperature, Equation 3.11 shows that the helium concentration is uniquely determined by the anemometer response voltage.

### 3.1.2 Calibration

The calibration phase is necessary to find the experimental constants, $a$ and $b$, used in Equation 3.10. These constants depend on the concentration of the mixture. For this purpose, a vessel was filled with a known helium concentration determined by the partial pressures of air and helium , i.e.,

$$X_{He} = \frac{P_{He}}{P_{mixture}} \tag{3.12}$$

The calibration tank was connected to an air cylinder and a helium cylinder. Valves allowed filling the tank with the desired quantities of each gas. A vacuum pump was also connected to the tank. It was used to empty the tank of any residual gases before starting a new mixture. A fan in the tank was used to enhance the mixing between the two gases. Measurements were taken of total pressure, total temperature and the hot-film voltage at several different vessel pressures. This procedure was repeated for several different helium concentrations. Figure 3.3 shows a set of curves and data from a typical calibration.

## 3.2 Aerothermodynamic Sampling

### 3.2.1 Pitot Pressure Probe

The Pitot probe had a $1.59mm$ outer diameter and $1.04mm$ inner diameter, which gave a capture area of $0.85mm^2$. The Pitot probe was attached to a Statham 0-3.40 atm pressure transducer by a $15cm$ length of flexible Tygon tubing and pressure fittings. The output

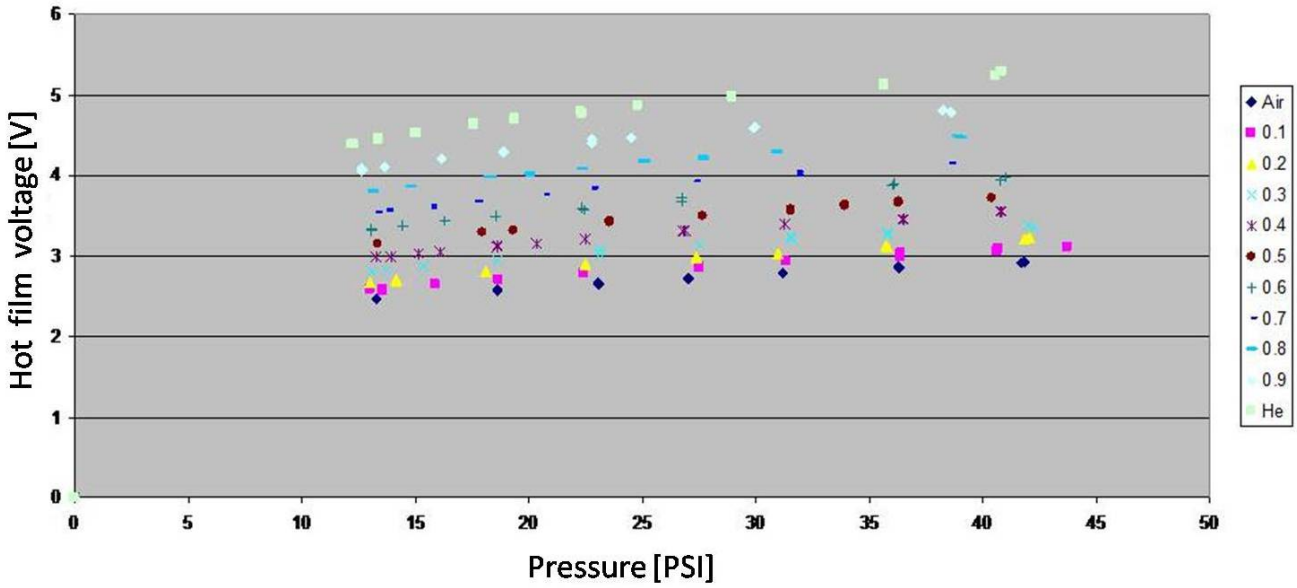


Figure 3.3: **Calibration**

voltage was amplified by a Measurements Group 2310 Signal Conditioning Amplifier and inputted into the data acquisition system.

### 3.2.2 Cone-Static Probe

The cone-static probe consisted of 1.59-mm-outer-diameter pipe with a 10-degree nominal semivertex angle. There were four small ports (diam. $= 0.38mm$) drilled normal to the cone surface. The four holes which led to a common chamber were located 90 deg. apart around the cone. The cone-static probe was attached to a Statham 0-20.4 atm pressure transducer by a $15cm$ length of flexible Tygon tubing and pressure fittings. The output voltage was amplified by a Measurements Group 2310 Signal Conditioning Amplifier and inputted into the data acquisition system.

### 3.2.3 Total Temperature Probe

Temperature profiles were measured with a sampling rake consisting of three $1.59mm$ outer-diameter tubes spaced $6.4mm$ apart with thermocouples inside. Each tube had an inner diameter of $1.04mm$ giving each probe a $0.85mm^2$ capture area. The total temperature probes each had four small holes (diam. $= 0.23mm$) drilled around their tubes. This was done to improve the recovery factors of the probes. Each total temperature probes capture to recovery area ratio was 5 to 1 resulting in a recovery factor of 0.98. Exposed junction type-E thermocouples with $0.25mm$ diameter beads were placed inside the three total temperature probes. The millivolt signals from the thermocouples were read directly into the data acquisition system.

## 3.3 Aerothermodynamic Sampling Traverse

The traverse used in the aerothermodynamic sampling experiments used a 4-Phase stepper motor made by Rapid Syn (Model 34D-9209A) and an American Precision Industries (Model DMA-64) stepper motor controller. The step angle was 1.8-deg. The tunnel control program was generally set to move 240 steps at speed of 600 steps a second up over 8 seconds stopping at 27 Locations ( 25-mm) along the way, and then 600 steps per second down to the original position. At each step, the position was maintained for approximately 300 ms. The data for each steps resulted from the average of the last 25 sample of the given step. The traverse motor was powered by a 24-volt DC power supply. The position of the traverse is measured by an LVDT (Linear Variable Differential Transformer). The LVDT is calibrated with dial calipers and a voltmeter. The dial calipers allow an accuracy of 0.0025-mm, which is sufficient for the experiments performed.

## 3.4 The Conical Five-hole probe

In support of the ongoing vortex dynamics research in supersonic streams at Virginia Tech, a customized Aeroprobe Inc., L-shaped five-hole probe was utilized. The early experimental investigation by Centolanzi[45] with a $20^o$ half angle conical probe demonstrated that accurate and simultaneous measurements of the Mach number components,

pressure and flow angularity in three-dimensional supersonic flow could be achieved with such an instrument. There are several characteristics of conical five-hole probe that must be considered when making flowfield surveys in a blowdown facility such as the VT supersonic tunnel. Metwally[46] used a five-hole probe with a tip diameter of $1.67mm$ to investigate the structure of supersonic streamwise vortices. However, his design routed $0.7m$ long tubing to the pressure transducers located outside the wind tunnel, thereby limiting the time response to a step input to about 1 sec.

The probe used in the present investigation is depicted in Figure 3.4. The conical probe tip is $0.065in$ in diameter with a semivertex angle of 30 degrees. The pressure ports are of 0.0165 (I.D.). The numbering convention of the pressure orifices is shown in Figure 3.5. The cone angle is machined to a high order of accuracy. The probe uses piezoresistive Endevco miniature transducers ( Model 8507-C-50). They where chosen for their smaller size, large temperature-compensation range, fast time-response, and high sensitivity. The probe has a 99% time-response to a step input of 11 milliseconds. Power to the module is Auto Sensing 100 - 240 VAC. Internal power supply output is $\pm$13.5 VDC. The 13.5 VDC power is filtered through a two-stage active filter then regulated to 10 V for sensors, and $\pm$12Vdc for Amplifier modules. Individual amplifier gain is set for the full range of the sensors to $\pm$ 5 VDC ($\pm$ 3 VDC minimum).

The probe was calibrated in the Mach 3.1 VT- Supersonic Free Jet facility with the calibration hardware shown in Figures 7.2 and 7.3. The free-jet facility was designed by the author for this specific project, in order to determine uniquely the local values of Mach number, total pressure, and flow angularity as functions of the measured orifice pressures $P_1$ through $P_5$ - see Figure 3.4 for the orifice numbering convention-. This is accomplished as follows. First, the probe is mounted in the facility using the support mechanism shown in Figures 7.2 and 7.3. This support mechanism provides two angular degree of freedom: the pitch angle $\alpha$ and the yaw angle denoted as $\beta$. Figure 3.6 shows the coordinate system of the probe. For experimental and data reduction purposes, we chose to transform the coordinate system described above and used in the calibration process into the spherical coordinate system defined by the pitch angle $\theta$ and the roll angle $\phi$. As Figure 3.6 clearly shows, $\theta$ is the angle between the probe axis and the local velocity vector, while $\phi$ is the angle between the $(x, y)$ plane and the $(V, x)$ plane. Pitch angle $\alpha$ and yaw angle $\beta$ uniquely specify the local flow direction. The calibration device allows for variations of both $\alpha$ and $\beta$ during the free-jet facility (continuous) run.

The probe was calibrated in $\alpha$ from $-18^0$ to $+18^0$ in increments of $0.9^0$ up to $9^0$ and in increments of $1.8^0$ for the remaining points. The yaw angle $\beta$ from $-18^0$ to $+18^0$ in increments of $0.9^0$ up to $9^0$ and in increments of $1.8^0$ for the remaining points.

This procedure , completely automatic, require around one hour of continuous run of the supersonic facilty . The full calibration map, given in chapter 5, consists of 961 points and is among the finest of all the supersonic calibrations described in the literature.

### 3.4.1 Five-Hole Probe Traverse

This system consisted of two Velmex, Inc. UniSlide Assemblies linear traverses mounted to each other, operated by 200-steps per revolution Warner Electric stepping motors. This enabled movement in the downstream and vertical directions. The two traverses were operated by a Velmex, Inc. stepping motor controller, which was in turn operated by the PC via LabView.

## 3.5 Shadowgraph Photography

A standard shadowgraph technique was employed to obtain detailed visualizations of the flow structures for several purposes ranging from the determination of the shock position in the jet-shock interaction experiments to the validation of iso-kinetic sampling capability of the concentration probe. The shadowgraph method depends upon the relative deflection of a light beam by gradients in the refractive index of the gas through which the beam of light passes. The index of refraction of a given mixture of gases is a function of the density. When a gradient in density is present in the flow, the rays of a collimated beam passing through the medium will be curved in the direction of increasing density and the screen will show a pattern of bright and dark regions where the rays have converged of diverged respectively. For three-dimensional flows, the resulting two-dimensional image is an integration of all effects in the path of the light. In the present investigation the light source system consisted of a General Radio Model 1538-A Strobatac, convex lens (f  7 inches), and adjustably-mounted light slit. For the beam collimation a 12 inches parabolic mirror with a focal length of 80 inches was utilized.

## 3.6 Data Acquisition System

General data acquisition was performed with a personal computer running with a Windows-98 operating system and a 16-bit, 16-channel single-ended A/D converter made by National Instruments, Model AT- MIO-16XE-50. To reduce signal noise, the A/D converter was used in an 8-channel differential input mode. The converter was configured with a National Instruments, Model AMUX-64T multiplexer board to increase the total number of usable differential channels to 32. The multiplexer was also equipped with an onboard cold junction compensator for temperature measurement. To minimize signal noise, the multiplexer was placed in a metal box, which was grounded to a copper water pipe in the room. The data acquisition system used LabVIEW software to process and record the input signals. During an experiment, the input signals were sampled at a rate of 500 Hz.

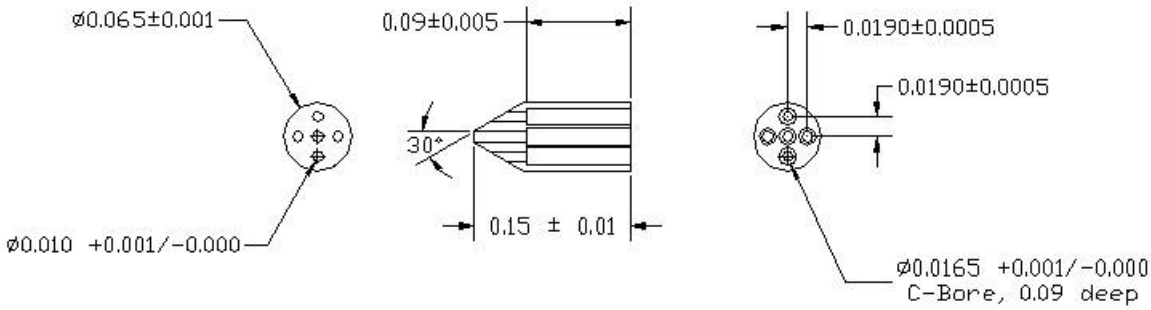


Figure 3.4: **Detail of conical five-hole tip (all dimensions are in inches)**

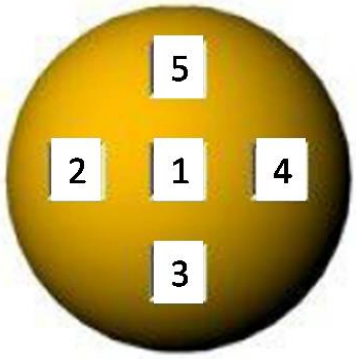


Figure 3.5: **The numbering convention of the pressure orifices**

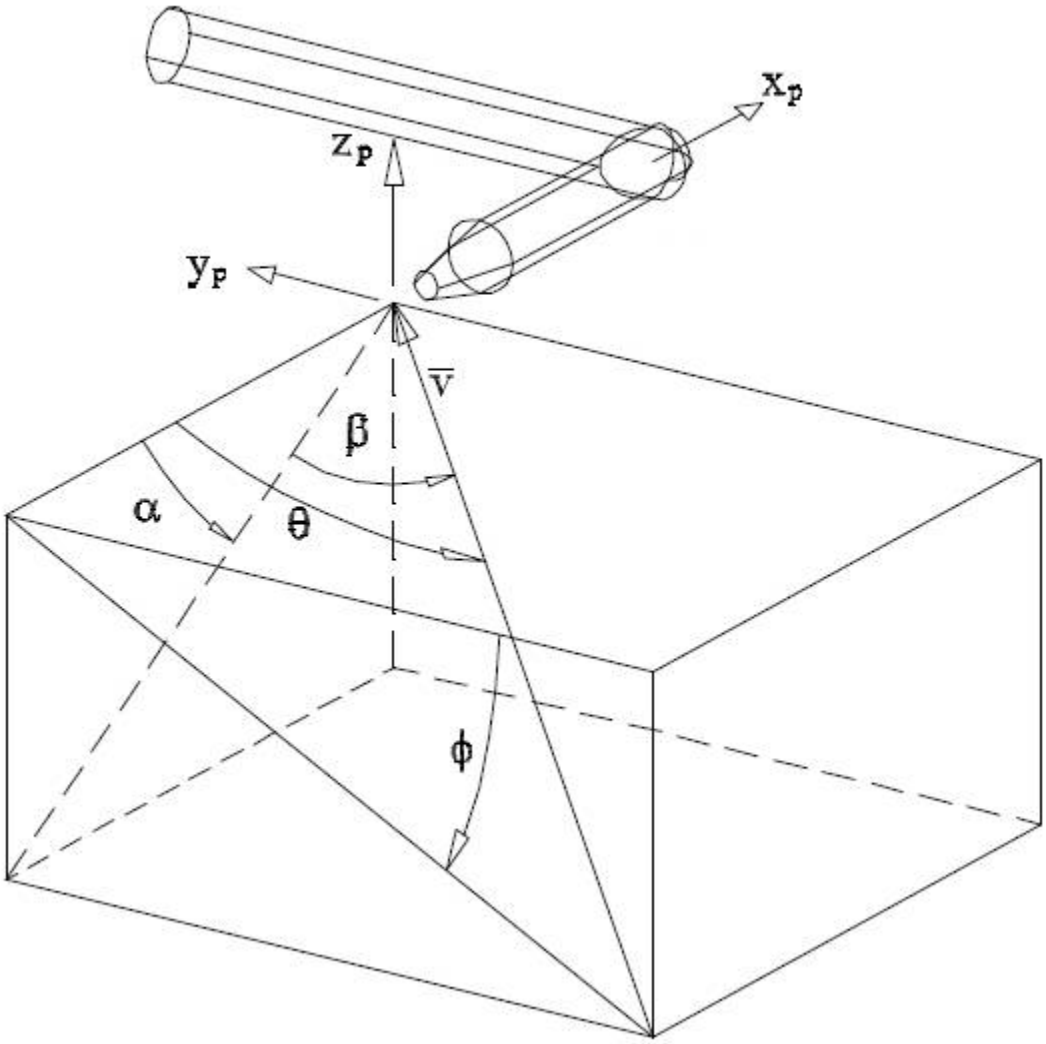


Figure 3.6: **Coordinate system associated with conical five-hole probe**

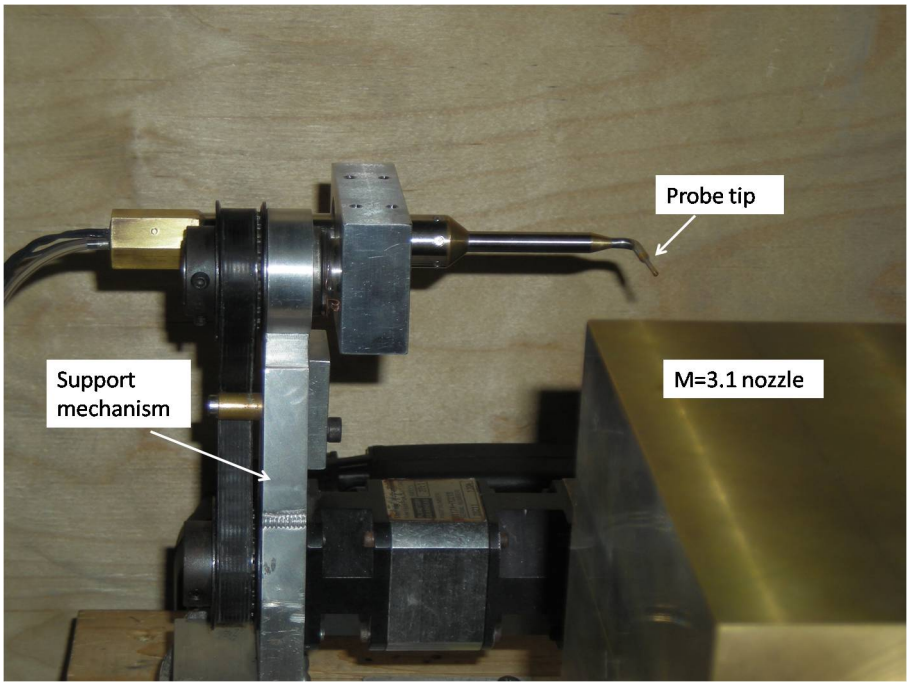


Figure 3.7: **Five-hole probe supersonic calibration in the Virginia Tech free-jet facility**

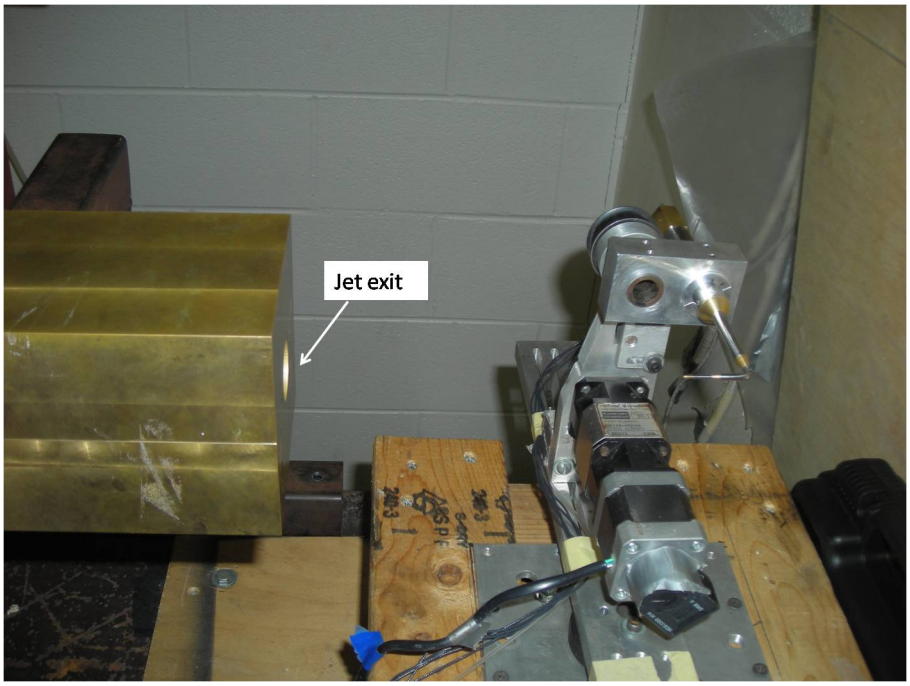


Figure 3.8: **Another view of the five-hole probe supersonic calibration setup**

# Chapter 4

# Data Analysis

## 4.1 Introduction

The results of the calibrations and the reduction of the data obtained by the experimental techniques discussed in Chapter 3 are presented in the following sections.

## 4.2 Conical Five-Hole Probe

Through a calibration process, the conical five hole relates the five pressure measurement to local flow quantities as flow angularity, Mach number and total pressure. The result of the angularity calibration described in Chapter 3 is shown in Figure 4.1. Surface pressure data were organized in terms of non-dimensional pitch and roll coefficients, defined as :

$$C_{p\eta} = \frac{P5 - P1}{q} \tag{4.1}$$

$$C_{p\xi} = \frac{P4 - P2}{q} \tag{4.2}$$

where $P2$,$P3$,$P4$,$P5$ are the four peripherical cone pressures, and $q$ is the dynamic pressure. In this figure, the calibration points, each of which represents a unique combination of pitch, $\theta$, and roll, $\phi$, are plotted versus the flow angularity parameters described above.

The flow angularity curve is independent of Mach number, as demonstrated by the results of various researchers(see Appendix C). In addition to the flow-angularity map, another important characteristic of the probe was determined with the probe aligned with the flow at different Mach numbers. The result is presented in Figure 4.2 and represents the relation between the Mach number and the ratio $P_A/P1$, where $P1$ is the central port pressure and $P_A$ is the average of the four peripheral cone pressures. The Mach number found from the ratio $P1/P0$ where $P0$ is the local total pressure agreed with normal shock theory for the total pressure ratio across a normal shock. This is expected since the probe tip is a slender blunt body. Appendix C presents a detailed analysis of the bluntness effects of the probe and the deviation of $P_A/P1$ with respect to the pointed cone solution and a way to predict the curve based on the results of the Krasnov[47] analysis.

It should be emphasized that the calibration curves shown in Figure 4.1 and Figure 4.2 are for $\theta = 0$. During use, however, the pitch angle will not be zero. The calculated values of $P_A/P1$ and $P1/P0$ must then be corrected for flow angularity. The measured values of $P_A/P1$ and $P1/P0$ are corrected by dividing them by the correction factors corresponding to the values of the flow angularity parameters. Figure 4.3 shows the correction factors obtained in the present calibration.

The data reduction process needed to convert the raw cone surface and Pitot pressure data into incoming flows properties follows that of Centolanzi.[45] The first iteration of the incoming Mach number is obtained from the measured $P_{AV}/P1$ ratio utilizing calibration data for the zero angle of attack case (Figure 4.2). The resulting Mach number is then used in conjunction with the pressure readings from the probe to compute the pitch and roll coefficients,$C_{p\eta} = \frac{P5-P1}{q}$ and $C_{p\xi} = \frac{P4-P2}{q}$. From the angularity map ( Figure 4.1) the associated pitch and roll angles are then evaluated. The three Mach number components can be related to the incoming Mach number via a combination of pitch, $(\theta)$, and roll, $(\phi)$, angles:

$$M_x = -Msin(\theta)sin(\phi) \tag{4.3}$$

$$M_y = -Msin(\theta)cos(\phi) \tag{4.4}$$

$$M_z = Mcos(\theta) \tag{4.5}$$

Since $P_{AV}/P1$ and $P1/P0$ are functions of the local direction of the flow, additional iterations may be required to correct the initial estimate of the incoming Mach number. Correction factors as shown in Figure 4.1 are used to proceed in subsequent iterations. The process is then repeated until the variation in the inferred flow angularity parameters between two consecutive iterations is within a user-defined tolerance, at which point a convergent solution is obtained. The entire data reduction process is automated in a Matlab computer code.
Estimated uncertainties associated with the five-hole conical probe measurements are in Table A.1:

Table 4.1: Estimated five-hole probe uncertainties

| Total pressure, % | Static presure, % | $M_x$% | $M_y$% | $M_z$% |
|---|---|---|---|---|
| 4 | 3 | 2 | 2 | 4 |

## 4.3 Gas Composition

The concentration probe hot-film voltage is related to the Reynolds number by:

$$V_2 = \frac{(R_s + R_f)^2}{R_f} \pi l k \alpha \left( \frac{d}{\mu\sqrt{T_t}} \frac{P_t}{} \frac{A^*}{A} C^* \right)^{\beta} (T_f - T_t) \tag{4.6}$$

where $R_s$, $R_w$, and $l$, are known, $k$ is a function of the gas composition, and $T_t$ was was measured with an internal thermocouple located at the sensor location. Constants a and b were determined from the concentration probe calibration curves. For each vertical traverse location, a file was generated containing the probe location, sensor voltage, internal probe total pressure and total temperature. At each point, a computer routine used Equation 4.6 with $P_t$ and $T_t$ to calculate the upper and lower voltage bounds, at any given calibration level. The program then would start with the calibration curve of the lowest helium concentration, and sequentially search for the two curves that bounded the voltage at the appropriate pressure. The experimental helium concentration was found

by interpolation from the bounding curves. Once all the lateral stations per axial location were reduced, they were put together, and contour plots were generated.

## 4.4 Mean Flow Data Reduction

A second code matched the previously calculated helium concentration data to the cone-static pressure, Pitot pressure, and total temperature data points in order to calculate profiles for Mach number, density, velocity, mass flux, as well as the flowfield static quantities. Since the ratio of specific heats,$\gamma$, is needed to calculate most of the quantities, it is considered first, and values of $\gamma(y,z)$ and $R(y,z)$ were computed based on the local helium concentration. The specific gas constant ,$R$, for the local helium mole fraction, $X_{He}$ is given as:

$$R = \frac{\mathbb{R}}{X_{He}\mathbb{M}_{He} + (1 - X_{He})\,\mathbb{M}_{air}} \tag{4.7}$$

In order to calculate the ratio of specific heats, $\gamma$, the static temperature $T$ is guessed for the first approximation.

$$R = \frac{\mathbb{M}_{He}X_{He}C_{p,He} + \mathbb{M}_{air}\,(1 - X_{He})\,C_{p,air}}{X_{He}\mathbb{M}_{He} + (1 - X_{He})\,\mathbb{M}_{air}} \tag{4.8}$$

Next, the remaining flow quantities,$M$, $P$ and $P_t$, can be calculated. The Rayleigh-Pitot formula relates $P/P_{t,Pitot} to \mathrm{M}$ *and.*

$$\frac{P}{P_{t,Pitot}} = \left[\frac{(\gamma+1)\,M^2}{2}\right]^{\frac{\gamma}{\gamma-1}} \left[\frac{\gamma+1}{2\gamma M^2 - (\gamma-1)}\right]^{\frac{1}{\gamma-1}} = f\,(M,\gamma) \tag{4.9}$$

This formula assumes a normal shock in front of the Pitot probe tip. The Taylor-Maccoll equation for the supersonic flow over a cone is a 2nd order, non-linear, ordinary differential equation. This equation was solved numerically for a large range of Mach numbers with $\gamma$ varying form 1.4 to 1.66. Using the Taylor-Maccoll solution, it is possible to evaluate the quantity:

$$\frac{P_c}{P} = f(M,\gamma) \tag{4.10}$$

Taking the ratio of Equation 4.10 and Equation 4.9, one obtains:

$$\frac{P_c}{P_{t,Pitot}} = f(M, \gamma) \tag{4.11}$$

The left-hand side of Equation 4.11 is known, since $P_c$ and $P_{t,Pitot}$ were experimentally measured. For each value of $\gamma$ , a table with the pressure ratio $P_c/P_{t,Pitot}$ and the corresponding Mach number was created using the numerical solution of Equation 4.11.

By comparison with the experimental pressure ratio, the local Mach number was determined. The local speed of sound, velocity and density were then calculated by use of their respective perfect gas relations. All calculations assumed a calorically perfect gas (with constant specific heats). A new value of temperature T can be calculated with the obtained Mach number using the adiabatic flow relation:

$$T = T_t \left(1 + \frac{\gamma - 1}{2} M^2\right)^{-1} \tag{4.12}$$

The entire process is then iterated until convergence.

For a specific Mach number, depending of the ratio of specific heats, the cone-shock will become detached, and the above reduction method will be rendered invalid. This condition was indicated when $P_c/P_{t,Pitot}$ was greater than a critical value determined by the cone solution. When this occurred, the static pressure, $P$, was interpolated from the nearest noncritical points. The ratio of static to Pitot pressure, $P/P_{t,Pitot}$, was then compared to the value for sonic flow expressed as :

$$\left(\frac{P}{P_{t,Pitot}}\right) = \left(\frac{\gamma + 1}{2}\right)^{\frac{-\gamma}{\gamma - 1}} \tag{4.13}$$

If $(P/P_{t,Pitot}) < (P/P_{t,Pitot})_{crit})$ the flow was supersonic and the Mach number was calculated using the Rayleight- Pitot formula. If$(P/P_{t,Pitot}) > (P/P_{t,Pitot})_{crit})$, the flow was subsonic so $P_{t,Pitot} = P_t$ and the Mach number can be calculated with the isentropic relation:

$$M = \left[\frac{2}{\gamma - 1}\left(\left(\frac{P}{P_t}\right)^{\frac{1-\gamma}{\gamma}} - 1\right)\right]^{\frac{1}{2}} \tag{4.14}$$

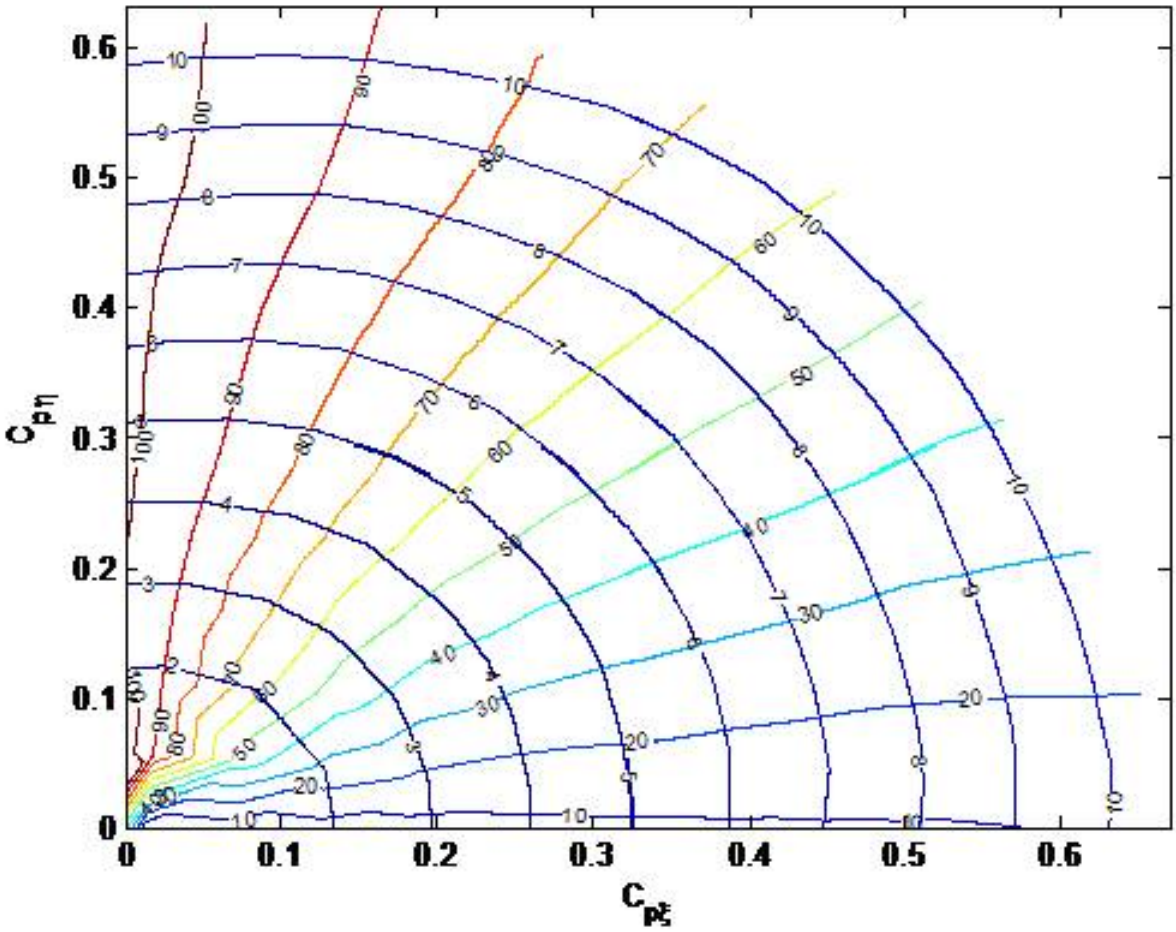


Figure 4.1: **Conical five-hole flow angularity calibration at M=3.1**

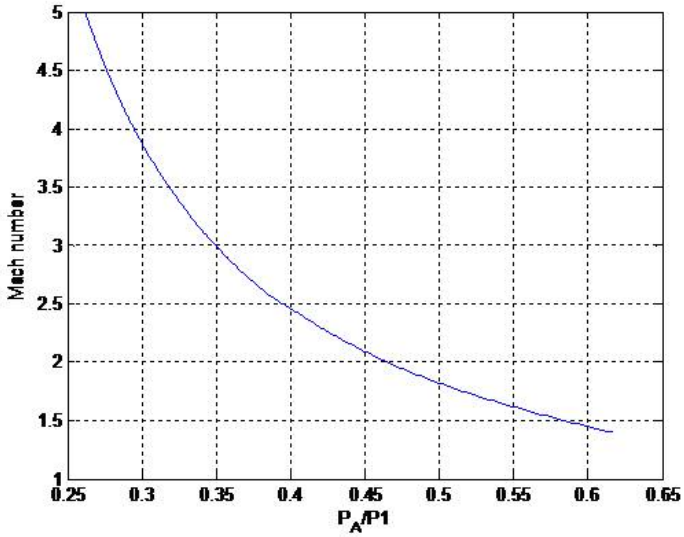


Figure 4.2: **Mach number vs. the measured five-hole probe**

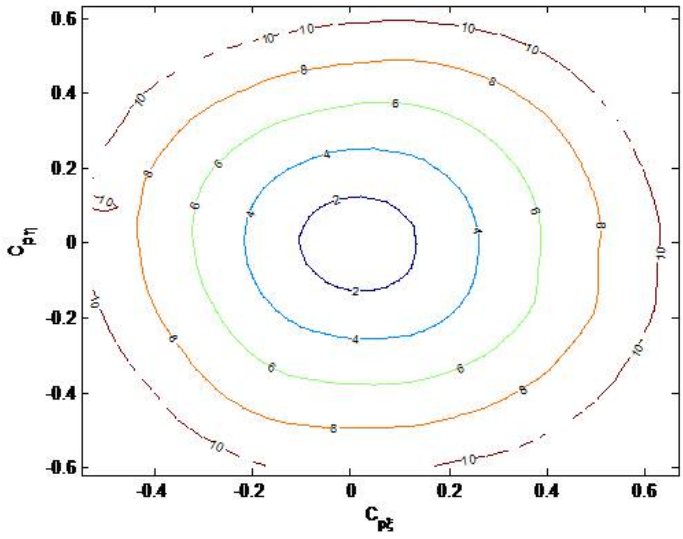


Figure 4.3: **Correction factors**

# Chapter 5

# Investigation of Light-Gas Injectors in a Mach 4 Crossflow

## 5.1 Overview

An experimental study of an aerodynamic ramp (aeroramp) injector, initially proposed by Jacobsen[24] for higher molecular weight ($\mathbb{M} \approx 30$) injectants in a Mach 2.4 airstream, was conducted with light gas injectants in a Mach 4 airstream. The aeroramp consisted of an array of two rows with two columns of flush-wall holes that induce vorticity and enhance mixing. The holes were spaced four diameters apart in the streamwise direction with a two diameter transverse spacing between them. For comparison, a single-hole circular injector with the same area angled downstream at 30 degrees was also examined. Test conditions involved sonic injection of helium heated to 313 K, to safely simulate hydrogen into a nominal Mach 4 air cross-stream with average Reynolds number $5.77 \cdot 10^7$ per meter at a jet to freestream momentum flux ratio of 2.1. Sampling probe measurements were utilized to determine the local helium concentration. Pitot and cone-static pressure probes and a diffuser thermocouple probe were employed to document the flow.

## 5.2 Experimental Results

All plots presented are from measurements taken at a station $16.4d_{eq}$ downstream of the injector. The plots extend $5d_{eq}$ on either side of the injector centerline, and data were acquired to an elevation of $18d_{eq}$ above the tunnel floor. A height of $16.4d_{eq}$ was found to adequately capture the flow characteristics for total temperature, mass fraction and Mach number, so data is only presented in this region. The uncertainty in probe position was $\pm 0.3 and \pm 0.2mm$ in the cross-stream and vertical positions, respectively.

### 5.2.1 Total Temperature Contours

Total temperature profiles of the aeroramp injector are presented in Figure 5.1. These figures show the results from the aero-thermodynamic measurements using the triple-rake, total temperature probe. The local total temperature profiles are normalized by the freestream total temperature, and both profiles are set to the same non-dimensional scale for ease of comparison. These isothermal contours illustrate the total temperature field produced by the injection process near the plume of the injector and allow for a qualitative and quantitative assessment of the penetration and mixing produced by the injectors. An interesting feature of the single-hole injector temperature profile,(Figure 5.2), is the horseshoe-shaped structure. This shape is often associated with a vortex structure generated by the interaction of a jet in a crossflow and is the main mechanism for mixing enhancement for this type of injectors. The aeroramp also generates vorticity from the interference effects of the multiple jet interactions and the toe-in angles of the individual jets. At this point, one might be tempted to estimate mixing performance assuming an analogy between the temperature and the concentration fields. The temperatures in the plume from the aeroramp are lower than those in the circular injector plume, indicating more rapid mixing of the heated helium injectant. One source of error in such an analysis is the total heat loss from the fuel injected from the aeroramp with respect to that injected from the single-hole injector. In the case of the aeroramp, there are four copper feed tubes, each supplying one specific orifice, compared to the single-hole injector, with a single large supply tube. Another factor making such a comparison less than useful is the interaction between vorticity and total temperature as represented by the Crocco's theorem.

### 5.2.2 Total Pressure Contours and Total Pressure Loss Parameter

Total pressure profiles of the aerodynamic-ramp and single-hole injectors are shown in Figure 5.3 and Figure 5.4. These plots show the results from the aero-thermodynamic measurement experiments. The local total pressure profiles are normalized by the freestream total pressure ($1034kPa$), and both sets of profiles are set to the same non-dimensional scale for ease of comparison. These isobar contours illustrate the total pressure field produced by the injection process and allow for a qualitative and quantitative assessment of the losses incurred by the injectors. It can be seen that the aeroramp produced higher local pressure losses in a larger area compared to the single-hole injector. However, the shock from the aeroramp is weaker than that of the single-hole injector. This can be seen in the Mach number profiles below. The overall total pressure losses are quantified using the overall total pressure loss parameter, which involved numerical integration of the mass-flow-weighted total pressure field over the sampled area. The overall total pressure recovery, $P_{t,rec}$, is defined as[21]

$$P_{t,rec} = \frac{\int \rho u P_t dA}{\int \rho_\infty u_\infty P_{t,\infty} + \rho_j u_j P_{t,j} A_j} \tag{5.1}$$

Then, the total pressure loss parameter is defined as follows, $\Pi = 1 - P_{t,rec}$. A parameter value of $\Pi = 0$ indicates no total pressure loss and, $\Pi = 1$ indicates complete total pressure loss.

Table 5.1 presents the results for the total pressure loss parameter. These results show the aeroramp injector to have only very slightly higher overall losses compared to the single-hole. At first glance, this appears in contradiction with the total pressure profiles in Figure 5.3 and Figure 5.4 and the comments above. However, because the overall total pressure loss parameter is a mass-flow-averaged quantity, the parameter is not assessed on local total pressure alone, but on local density and velocity as well. It turns out that the plume of the aeroramp injector has a higher velocity field in the jet plume. This high

velocity field significantly offsets the lower local total pressure.

### 5.2.3 Mass Fraction Contours

Helium concentration data are presented in the form of mass fraction contour plots. Also indicated are the numerical magnitude of the maximum mass fraction ($\alpha_{max}$) and the location of this local maximum in the plume with an $\times$ on the contours plots. The minimum contour line ($\alpha = 0.02$) represents the minimum value of concentration measurable in the experiment. The centroid of the lean limit mass fraction for homogeneous H2-air deflagration at ambient conditions ($\alpha = 0.00292$) corresponds to the plume center of mass, and the symbol $\bullet$ marks this position. The contour plots for the aeroramp injector can be seen in Figure 5.5. The core of the jet, defined by the maximum helium mass fraction, is located at approximately $y/d_{eff} = 0.68$ at an elevation of $z/d_{eff} = 1.7$. Figure 5.6, is the plume cross-section for the single-hole injector. The core of the jet is above the injector centerline at an elevation of $z/d_{eff} = 2.73$. The core of the jets, for both injectors, is inside the boundary layer. At this axial location the boundary layer is about 18 mm as determined in the shadowgraphs. An initial inspection of Figure 5 shows a wider injectant spread for the aeroramp, and a higher penetration for the single-hole injector. The profiles show the aeroramp having approximately the same maximum mass fraction and plume area as the single-hole injector, and they also qualitatively show the same mixing extent. Results for these items will be presented subsequently. For the single-hole injector, the characteristic horseshoe-shaped structure of the plume, associated with a vortex generated by the jet-freestream interaction, is beginning to appear at the measurement plane. The aeroramp, on the other hand, produces a wide horizontal region of maximum mass fraction at approximately a constant height of $2d_{eff}$. In general, the aeroramp injector generates vorticity not only by jet-freestream interaction, but also from the combined effects of the multiple jet interaction, the toe-in angles of the jets, and additional vorticity generated by the multiple jet bow shocks (Crocco's Theorem). In the present investigation, there is no evidence of a significant counter-rotating axial vortical motion, usually identified by the formation of two primary cores in the aeroramp results.

### 5.2.4 Jet interaction Characteristics

A quantifiable measure of the penetration of the fuel plume into the main flow is given by the location of the center of mass in a cross-sectional plane (y-z) of the flow[48]

$$z_{cm} = \frac{\int_A \rho u c z \, dA}{\dot{m}_{j,probe}} \tag{5.2}$$

The results presented in Table 5.1 show the single-hole injector penetrates higher than the aeroramp, as expected, based on considering the higher momentum value in the z-direction. Table 1 also presents the results for the plume width, $y\pm$, defined by the distance between the plume core and the stoichiometric side edges, respectively. The aeroramp produces a significantly larger amount of lateral mixing. The overall plume area is defined here as the total area of the plume that has an $\alpha$ greater or equal to the stoichiometric value for hydrogen, namely 0.0292. Results from this study are presented in Table 5.1. The over-stoichiometric-plume areas are normalized by $A_u$, the area of an isentropically expanded jet with a static pressure equal to that of the freestream. The results show that the over-stoichiometric-plume area of the aeroramp injector array is larger than that of the single-hole injector. In a non-reacting simulation of a supersonic combustor, it is useful to know the mixing efficiency of the injection process. This predicts how well the fuel would burn in an actual scramjet combustor with the same pressure field. The mixing efficiency, $\eta_m$, is the total mass of fuel which would react assuming steady, isentropic, quasi 1-D flow divided by the total mass flow rate of fuel. This is given by:[49]

$$\eta_m = \frac{\int \rho u \mathbb{Z} \, dA}{\int \rho u c \, dA} \tag{5.3}$$

where $\mathbb{Z}$ is the local injectant mass fraction which would react if the injectan were $H_2$ assuming

$$\mathbb{Z} = \begin{cases} \alpha, & \text{if } \alpha \leq \text{f;} \\ (1-\alpha)\,\frac{f}{1-f}, & \text{if } c > \text{f;} \end{cases} \tag{5.4}$$

Table 5.1 presents the results, which show that the mixing efficiency value of the aeroramp

injector model is slightly higher than that for the single-hole injector.
The injectant mass flow (denominator of Equation 5.3) was compared with the injectant mass flow rate actually measured during the experiments. This analysis shows the uncertainty in conservation of mass of $\pm 17\% and \pm 18\%$ for the single-hole injector and the aeroramp, respectively. One cause for this uncertainty is the relatively sparse grid spacing. Other causes include errors in $\rho$, $u$ and $\alpha$ as described previously.

Table 5.1: Parameters

| Parameter | Aeroramp | Single-hole |
|---|---|---|
| $A/A_u$ | 25 | 26 |
| $z^+$ | 2 | 1.75 |
| $\eta_m$ | 0.22 | 0.20 |
| $\Pi$ | 0.389 | 0.378 |
| $y^{\pm}$ | 7.9 | 6.9 |

### 5.2.5 Mach Number Contours

Once the local mass fraction is known, it is possible to calculate the Mach number. Mach number contours of the aeroramp injector flow fields are shown in Figure 5.7 and Figure 5.8 respectively. The Mach number is about equal to its freestream value at the top of the profile. Each contour has a point corresponding approximately to the edge of the jet. The sharp decrease in Mach number is caused by mixing of low Mach number gas from the jets with the higher Mach number gas from the free stream, viscous forces in the boundary layer and the variation of the jet bow shock strength.

### 5.2.6 Summary

The main conclusions drawn from these studies are as follows:

1) The mixing efficiency value of the aeroramp was only slightly higher than that of the single-hole injector at these conditions.

2) The aeroramp injector showed somewhat higher local total pressure losses at some places in the plume than the single-hole injector. This was due to the higher angle of

injection of the first row of the aeroramp array and the multiple shock structures from the two rows of jets. Although the local total pressure losses appeared more substantial, the mass averaged total pressure loss parameter showed that the aero-ramp had the same overall losses in the area studied.

3) The aeroramp had a plume area comparable with the plume area of the single-hole injector. The aeroramp produced a larger amount of lateral mixing. This was due to the greater cross-stream distance between the individual injector holes.

4) The core of the jet, i.e. maximum helium mass fraction, was higher for the single-hole injector as expected considering the higher momentum value in the z direction. The plume center of mass was higher for the aeroramp injector.

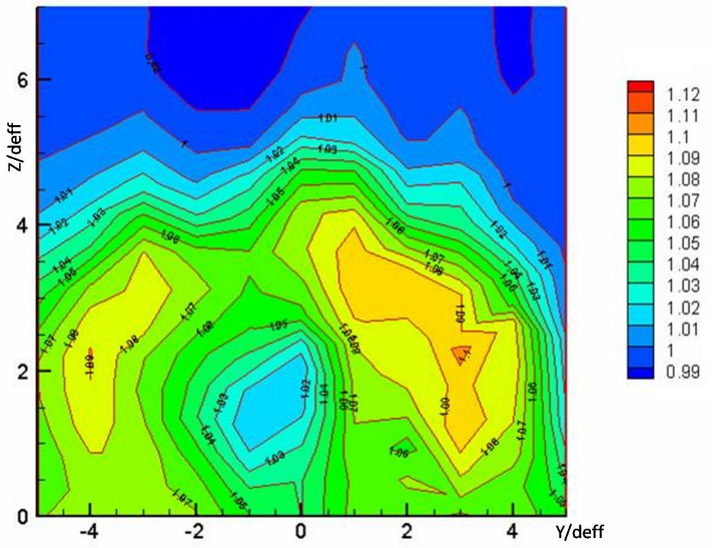


Figure 5.1: **Normalized total temperature contours, $T_t/T_{t,\infty}$ for the aeroamp injector**

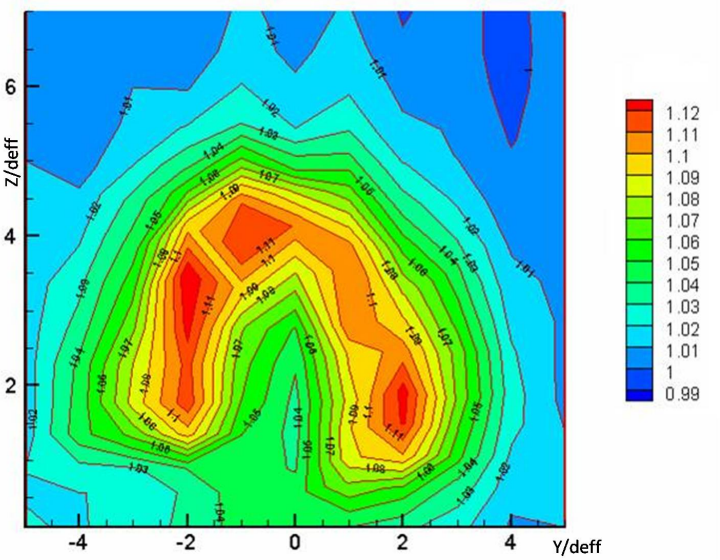


Figure 5.2: **Normalized total temperature contours, $T_t/T_{t,\infty}$, for the single-hole injector**

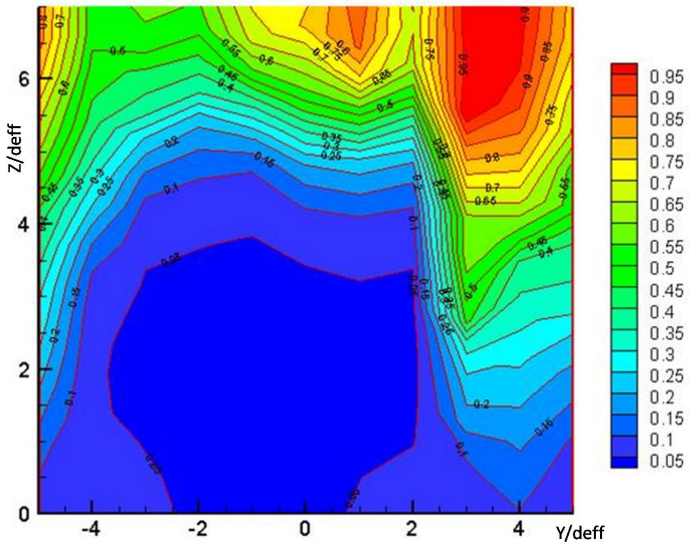


Figure 5.3: **Normalized total pressure contours, $P_t/P_{t,\infty}$, for the aeroramp**

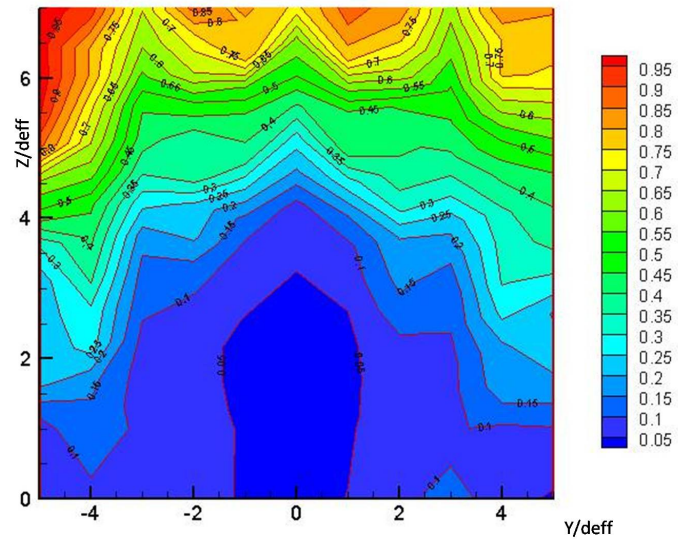


Figure 5.4: **Normalized total pressure contours, $P_t/P_{t,\infty}$, for the single-hole injector**

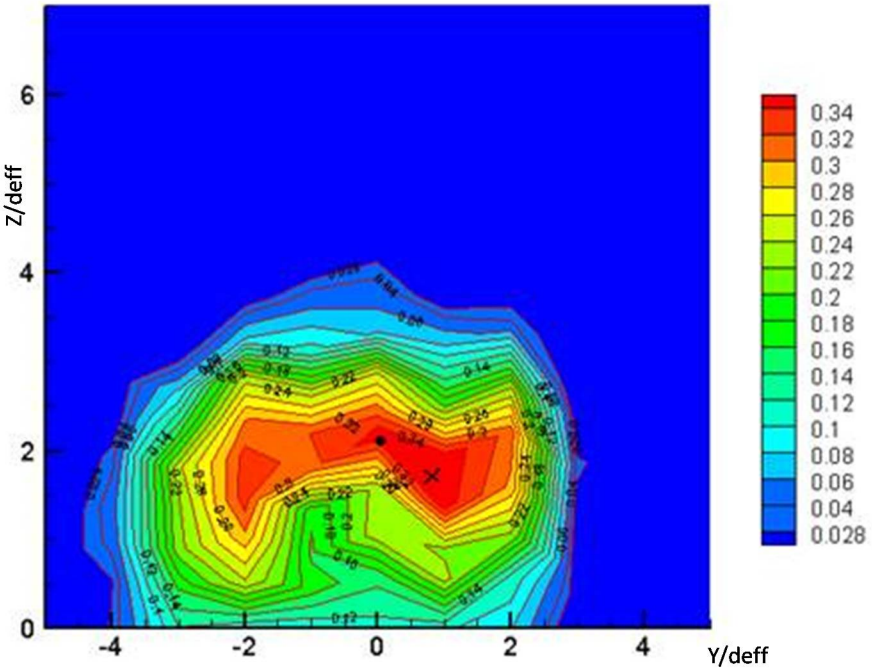


Figure 5.5: **Aeroramp injector mass fraction contours**

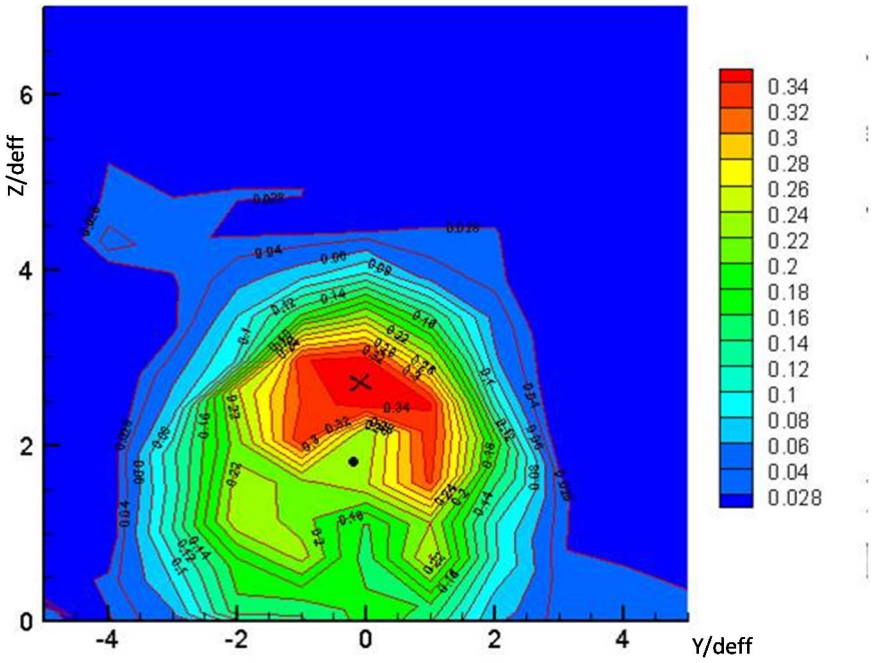


Figure 5.6: **Single-hole injector mass fraction contours**

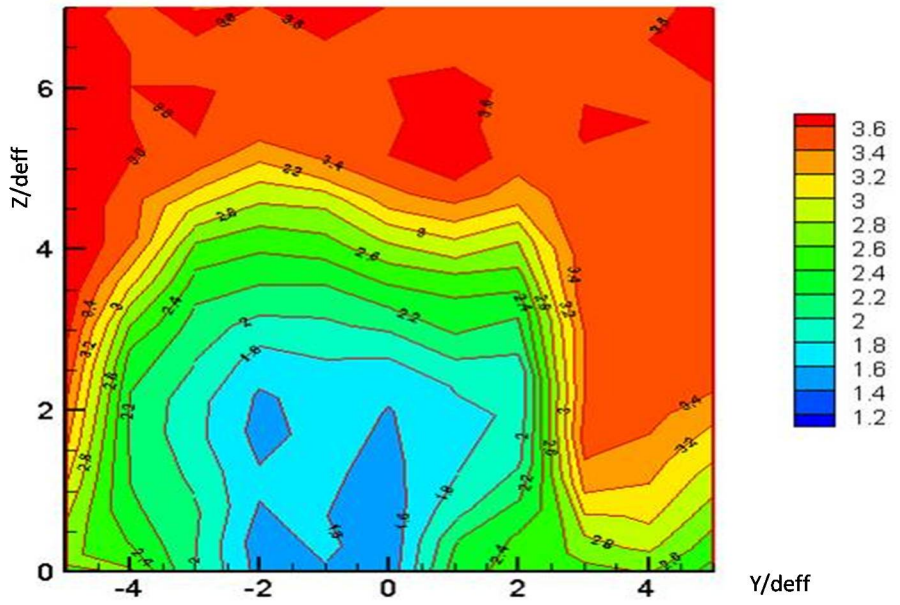


Figure 5.7: **Aeroramp injector Mach number contours**

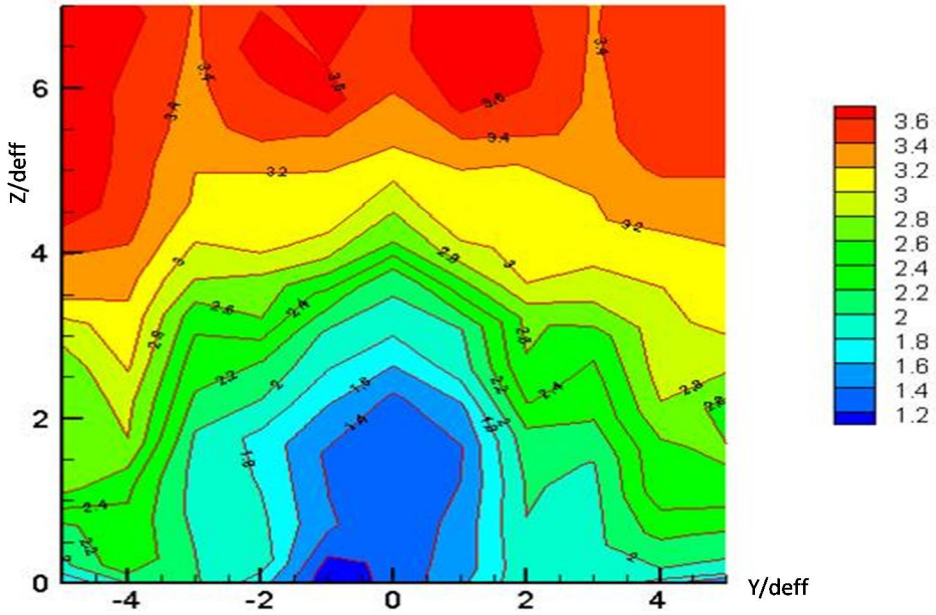


Figure 5.8: **Single-hole injector Mach number contours**

# Chapter 6

# Shock Wave / Transverse Injection Interaction

## 6.1 Background: The Richtmayer-Meshokov Instability, RMI

When the pressure gradient in a gas is not aligned with the density gradient, vorticity may be generated in the gas. If the gas undergoes on isentropic change of state, the direct relationship between pressure and the density guarantees the colinearity and no vorticity is generated. When, however, the density gradient is in part due to a variation of gas composition,the two gradients will be not aligned. A convenient analytical statement of this phenomenon is contained in Bjerknes theorem:

$$\frac{d\Gamma}{dt} = \int \frac{1}{\rho^2} \left( grad(\rho) \times grad(p) \right) dA \tag{6.1}$$

where $\Gamma$ is the circulation about a closed contour fixed with the fluid.

When a light fluid accelerates a heavy fluid, the misalignment of the pressure and density gradients gives rise to an instability of the interface and eventually produces the turbulent mixing of the fluids. This phenomenon is called the Rayleigh-Taylor instability

(RTI) if the acceleration is sustained and the Richtmyer-Meshkov instability (RMI) if the acceleration is driven by a shock or if it is impulsive.

Consider a cylindrical mass of low density gas embedded in a higher molecular weight gas. The discontinuity between light and heavy gas produce a radially outward density gradient around the circumference of the jet. The shock passage over this structure, which can be considered very fast in comparison with other processes, provides the pressure gradient and deposits a distribution of vorticity over the boundary. The baroclinic term, i.e., the cross product of pressure and density, will vary along the length of the interface due to the varying angle (included angle) between the gradients. The magnitude of vorticity will be greatest where the pressure and density gradients are most misaligned.The dynamics of this vorticity leads to roll-up of vortices of opposite sign.
Marble[42] first saw that the two dimensional, unsteady flow was a good analog for three-dimensional, steady flow produced when an oblique shock impinges on a light gas jet immersed in a co-flowing and supersonic air stream. Yang[43] et al. utilized this analogy in order to numerically simulate families of two-dimensional, unsteady shock induced vortical flows.

A complementary explanation of the results obtained in this investigation will be based on viewing the flow evolution from the context of vortex dynamics.

## 6.2 Objective of The Present Investigation

An experimental and computational study of the interaction of transverse injection with impinging shock waves was conducted. The examined gaseous injector was circular in geometry and angled downstream at 30 degrees to the horizontal. Test conditions involved sonic injection of helium heated to 313 K, to safely simulate hydrogen into a nominal Mach 4 air cross-stream with average Reynolds number $5.77 \cdot 10^7$ per meter at a jet to freestream momentum flux ratio of 2.1. A wedge upstream of the injector created a 20 degrees oblique shock which intersected with the jet plume at three different locations downstream of injection. Sampling probe measurements were utilized to determine the local helium concentration. Pitot and cone-static pressure probes and a diffuser thermocouple probe were employed to document the flow.
A pictorial description can be found in Figure 6.1. The three locations of shock impingement are labeled and designated cases 1, 2 and 3 corresponding to surface impact locations of 2 diameters, 8 diameters and 16 jet diameters respectively.

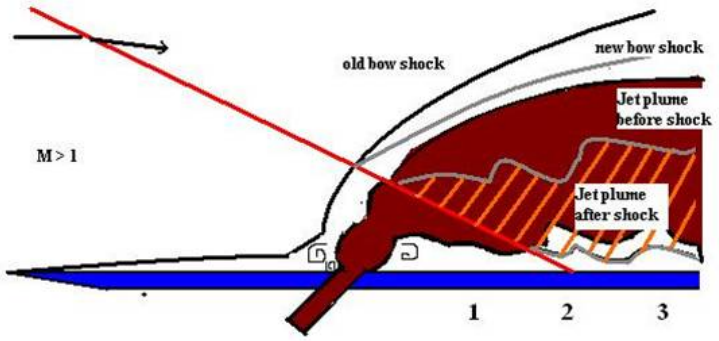


Figure 6.1: **Schematic of shock-jet with locations of shock impingement**

The re-orientation of the vorticity and the generation of the compressible vortex pair that results from viscous and impulsive forces acting at the periphery of the jet interact with the baroclinic generation of vorticity. Vorticity will be added or subtracted (depending on the sign) to the system. The new vorticity distribution can be expected to change the dynamics and the efficiency of the supersonic mixing process.

## 6.3 Experimental Results

### 6.3.1 Total Temperature and Mass Fraction Contours

Total temperature and mass fraction contours are presented in Figures 6.2 to 6.4 and Figures 6.5 to 6.7 respectively. The local total temperature profiles are normalized by the freestream total temperature. These isothermal contours illustrate the total temperature field produced by the injection process and allow for a qualitative assessment of penetration and mixing produced in the three cases under investigation. A distinctive feature is the horseshoe-shaped structure. This shape is associated with the counter-rotating vortex pair (CVP) structure generated by the interaction of a jet in a crossflow. The trend of the total temperature contours in the plume shows clearly that an attempt to estimate the mixing characteristics based upon this parameter can lead to a misinterpretation of the actual physics. This is known as the Ranque-Hilsch effect of the energy separation and has its foundation on Crocco's theorem relating changes in total temperature to vorticity.

As qualitatively shown in the plots and quantitatively reported in Table 6.1, Case 1 represents the situation that is most sensitive to the effects of the shock. In fact, the maximum concentration is the lowest at $\alpha_{max} = 0.30$, and the mixing efficiency is of the order of 24. Cases 2 and 3 are almost identical in terms of maximum concentration (almost the same value of the case without shock) and in terms of mixing efficiency. The explanation of this result will be proposed in the vortex dynamics section below.

### 6.3.2 Mach Number and Pitot Pressure Contours

Once the local mass fraction is known, it is possible to calculate the Mach number. Mach number contours of the flow fields for all the three cases are shown in Figures 6.8 to 6.10. Even in this complex three-dimensional situation in which the planar shock impinges upon the bow shock generated by the transverse injection of helium, it is possible to recognize the edge of the jet. The sharp decrease in Mach number is caused by the mixing of low-Mach number gas from the jet and the high-Mach number gas from the freestream, viscous forces in the boundary layer, and the variation of the jet bow shock strength. Case 1 is subjected to both the incident and reflected shock, and the Mach number is

lowest compared with the other cases. Cases 2 and 3 are similar only the incident shock effect is captured in the measurement plane.
Since $P_t$ are reduced data,the measured total pressure from the Pitot tube $P_{t2}$ was used in the plots in Figures 6.11 to 6.13. The local total pressure profiles are normalized by the freestream total pressure (1034 kPa), and both sets of profiles are set to the same non-dimensional scale for ease of comparison. These isobar contours illustrate the total pressure field produced by the injection process and allow for a qualitative and quantitative assessment of the losses incurred by the injectors. Of course, it makes little to sense to report total pressure losses from the injectors here because the impinging shock introduces additional losses.

Table 6.1: Parameters

| Parameter | Baseline case | case1 | case2 | case3 |
|---|---|---|---|---|
| $A/A_u$ | 5.07 | 3.6 | 3.8 | 4 |
| $z^+$ | 2 | 1.36 | 1.29 | 1.35 |
| $\eta_m$ | 0.20 | 0.24 | 0.19 | 0.18 |
| $y^{\pm}$ | 6.91 | 5.92 | 6.46 | 6.36 |
| $\alpha_{max}$ | 0.34 | 0.30 | 0.35 | 0.37 |

### 6.3.3 Shock - Generated Vorticity

We are now considering a transverse fuel jet accompanied with streamwise vorticity in closed domains with associated reflected shocks. Consider Figures 5.14 to 5.21 from the numerical simulations [courtesy of Campioli[50]]. We focus in the left part of the vortex pair, which has $\omega > 0$ and induces a strong vortex layer on the wall with $\omega < 0$. The action of the primary vortex makes the layer roll into a secondary vortex which has the core connected to the near-wall shear layer by a feeding sheet. This vortex-wall interaction is common for both the cases under investigation (i.e. Shock and No-Shock). Let's consider the jet (i.e. the counter-rotating vortex pair) passing throughout an oblique shock wave. Consider the left half-plane of Figures 14 to 21 referring to the shock case. The vortex core is an approximately circular region of light gas surrounded by a heavy gas having a strong initial counterclockwise vorticity. In the absence of this vorticity, the core would behave like the idealized cylindrical mass of low density gas embedded in a higher molecular weight gas described in the previous paragraph. The vorticity deposited

in its outer half would develop into a clockwise outer vortex, and the vorticity deposited in its inner half would develop into a counterclockwise inner vortex. . However, due to the vectorial nature of the vorticity (that allows the algebraic summation) one can expect that the core's strong initial counterclockwise vorticity suppresses the outer half's development and enhances the inner half's development. This partitioning of the initial vortex core increases the stretching beyond the case with no shock (stretching, through gradient intensification, makes diffusive effects become important, i.e. mixing). Consider now the shock/transverse injection interaction in the position where the developing vortical structure has not yet stabilized into a vortex pair. Again, the shock generates additional vorticity of both positive and negative sense, and it is the preferential coalescence of same-sense vorticity that determines the relative dynamics. The earlier the reflected shock hits the jet plume, the less stable is the original vortex pair and greater is the magnitude of the additional vorticity due to the shock. As the interface thickness increases downstream of the jet exit, the local density gradient decreases, and stretching rate decreases.

The expectation of greatly increase stretching for this situation is confirmed by the experiments and computations. It is possible to note the similarity between the vorticity contour at $8_{deq}$ for the case with shock and the contour at $16d_{eq}$ for the No-shock case. This shows how the dynamics of the shock case at $2d_{eq}$ is faster than the case without a shock. The superior stretching is confirmed by the greater dissipation rate at $16d_{eq}$.

The shock-vortex interaction generally leads to three-dimensional curvature of the shock front because of the strong gradients of total pressure and Mach number in a streamwise vortex (Houwing[51]).

Theoretical inviscid analysis has shown that the magnitude of the vorticity component tangential to a shock front is increased during interaction with a shock wave, while the magnitude of the normal component is unchanged. To gain a better understanding of how mixing is increased in the presence of shocks, an analysis of the vorticity change across the shocks was completed in conjunction with the numerical work of Campioli.[50] The analysis utilized two planes parallel to the shock, one just before and one just after. Through a coordinate transformation, the in-plane and normal to the shock vorticity components were calculated.

The vorticity over each plane of equal area was integrated, and the integrated quantity before the shock was subtracted from the integrated quantity after the shock. The change in vorticity magnitude and in-plane vorticity across the shock for each case can be found

in Campioli et al.[50] Case 1 showed the largest increase in both vorticity magnitude and in-plane vorticity. Case 1 has the largest density gradients, since the shock impingement is closest to the point of injection. Also, at 2 diameters behind the injector, the plume is nearly perpendicular to the shock which gives the largest cross product of density and pressure gradients. The larger non-aligned gradients created the largest change in vorticity due to baroclinic effects. For case 3, with the shock impingement at 16 diameters behind the shock, the plume and the shock have a smaller interior angle with respect to each other which makes the cross product of the gradients smaller than case 1.

### 6.3.4 Summary

The main conclusions drawn from these studies are as follows:

1) The addition of a shock behind gaseous injection into a Mach 4 crossflow enhances mixing.

2) The closer the shock to the injection point, the larger the effect on mixing and vorticity. The earlier the reflected shock intersects the jet, the less stable is the original jet vortex pair and the greater is the influence and the magnitude.

2) The results show no benefit from the impinging shock far from the injection point compared to the baseline case.

3)The vortex dynamics analysis helped in the interpretation of the results and showed faster mixing for the cases with shocks.

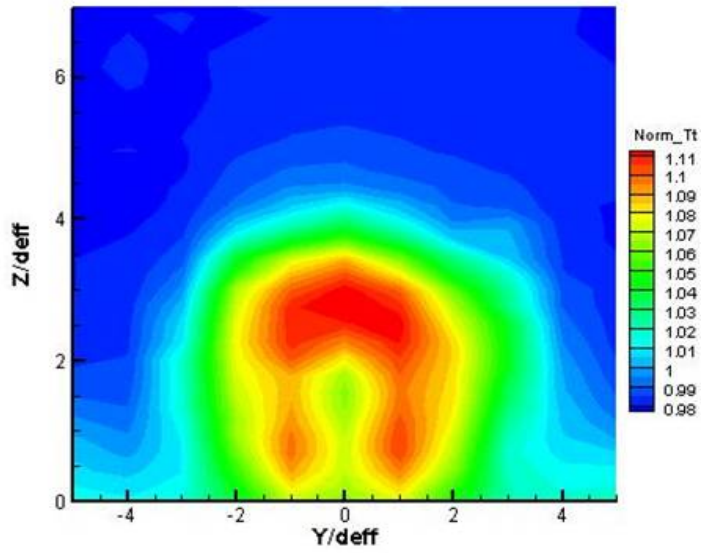


Figure 6.2: **Normalized Total Temperature Contours in the (y-z plane) at $x/d_{eff} = 16.4$ :Case 1 (Shock at $x/d = 2$)**

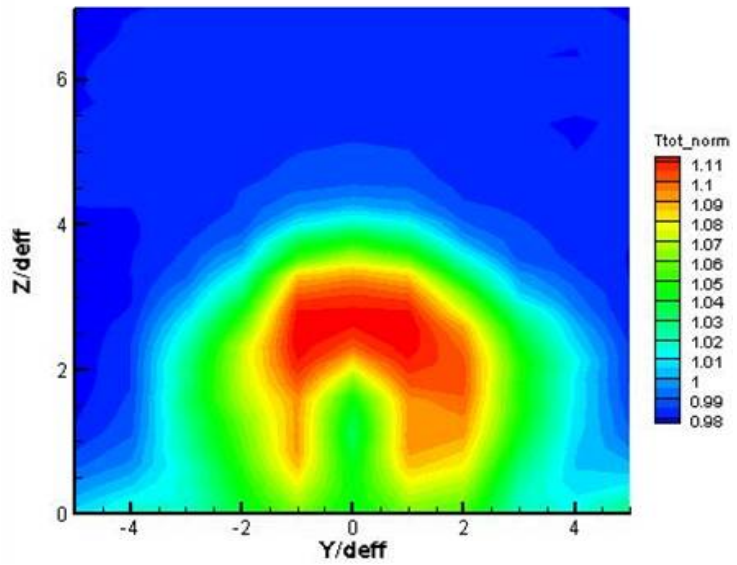


Figure 6.3: **Normalized Total Temperature Contours in the (y-z plane) at $x/d_{eff} = 16.4$ :Case 2 (Shock at $x/d = 8$)**

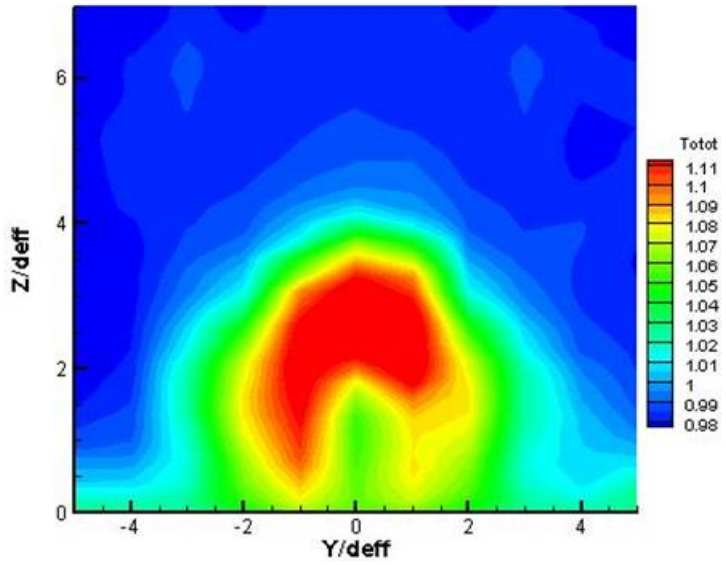


Figure 6.4: **Normalized Total Temperature Contour sin the (y-z plane) at** $x/d_{eff} = 16.4$ **:Case 3 (Shock at** $x/d = 16$**)**

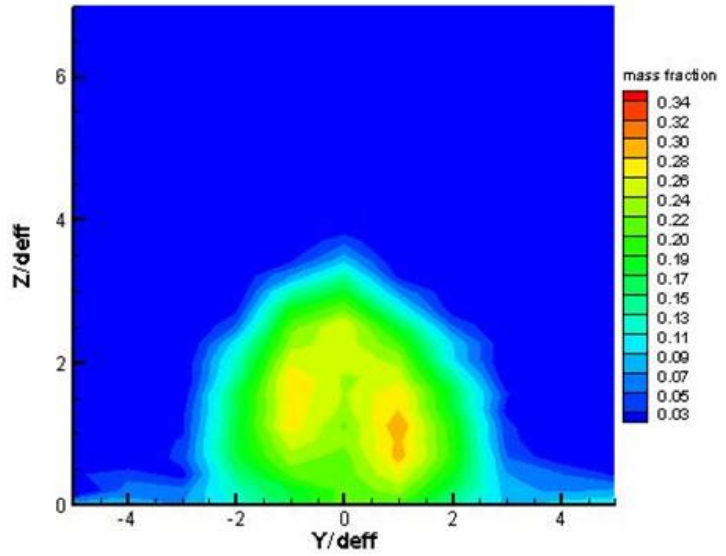


Figure 6.5: **Mass Fraction Contours in the (y-z plane) at** $x/d_{eff} = 16.4$ **:Case 1 (Shock at** $x/d = 2$**)**

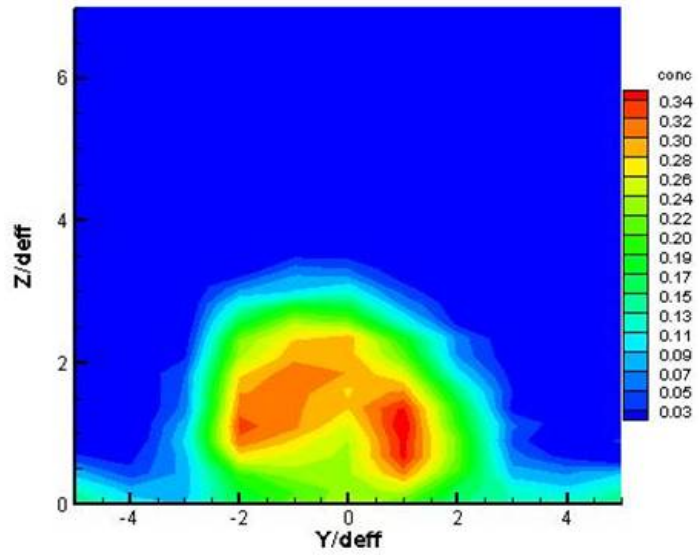


Figure 6.6: **Mass Fraction Contours in the (y-z plane) at $x/d_{eff} = 16.4$ :Case 2 (Shock at $x/d = 8$)**

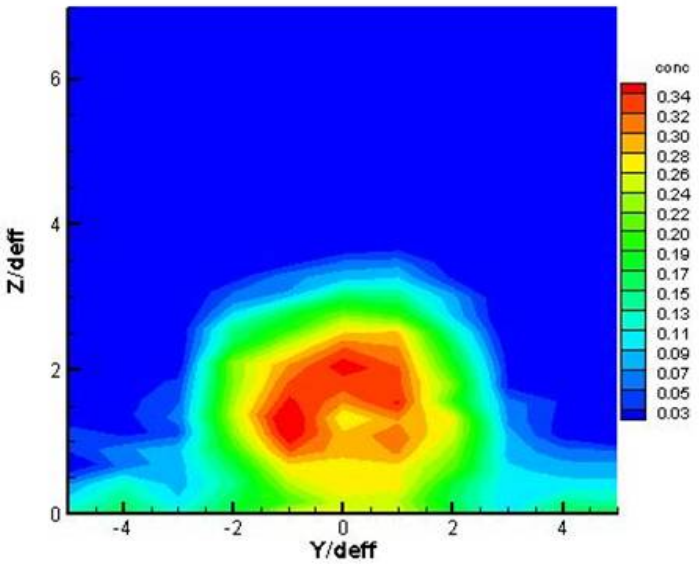


Figure 6.7: **Mass Fraction Contours in the (y-z plane) at $x/d_{eff} = 16.4$ :Case 3 (Shock at $x/d = 16$)**

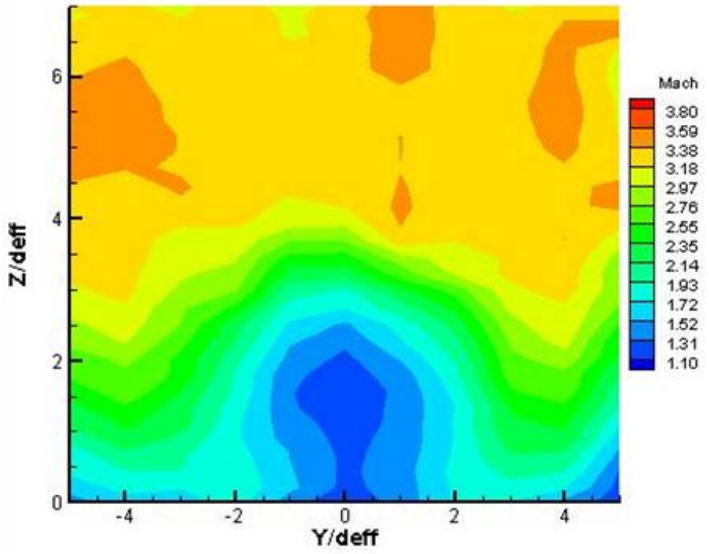


Figure 6.8: **Mach Number Contours in the (y-z plane) at $x/d_{eff} = 16.4$ :Case 1 (Shock at $x/d = 2$)**

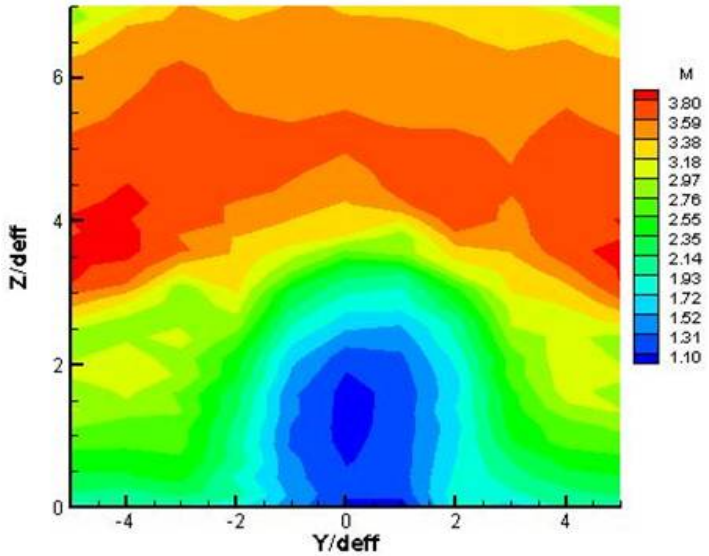


Figure 6.9: **Mach Number Contours in the (y-z plane) at $x/d_{eff} = 16.4$ :Case 2 (Shock at $x/d = 8$)**

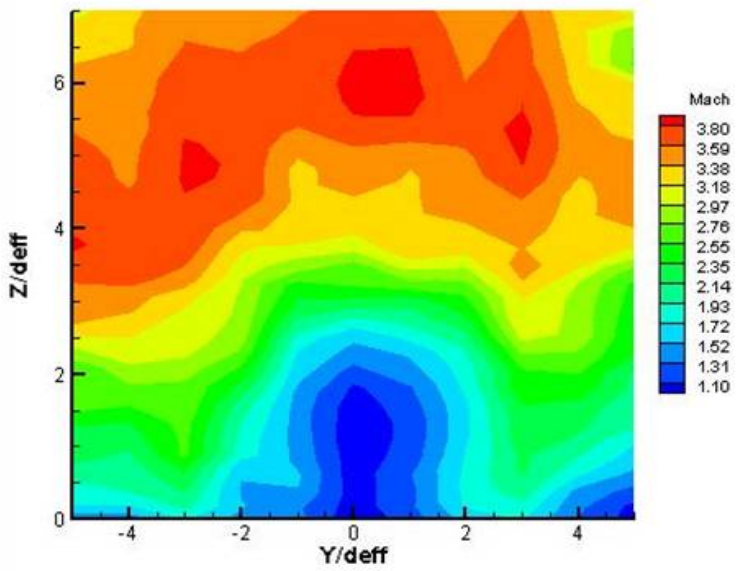


Figure 6.10: **Mach Number Contours in the (y-z plane) at $x/d_{eff} = 16.4$ :Case 3 (Shock at $x/d = 8$)**

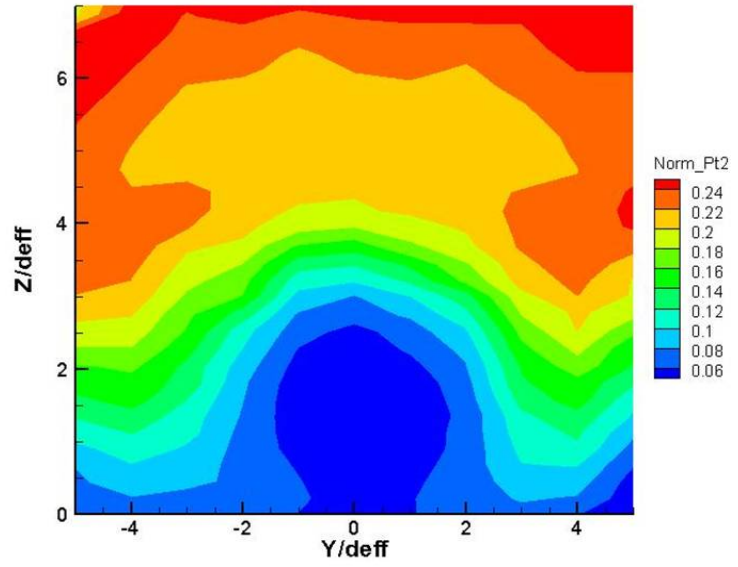


Figure 6.11: **Normalized Pitot Pressure in the (y-z plane) at $x/d_{eff} = 16.4$ :Case 1 (Shock at $x/d = 2$)**

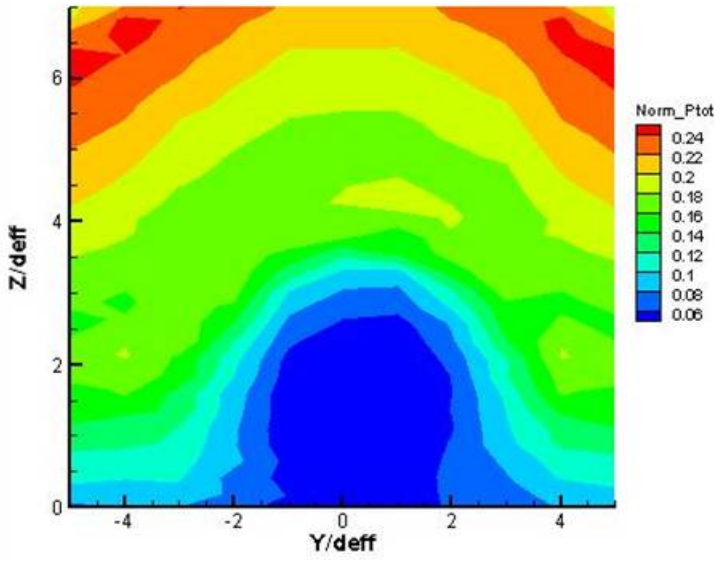


Figure 6.12: **Normalized Pitot Pressure in the (y-z plane) at $x/d_{eff} = 16.4$ :Case 2 (Shock at $x/d = 8$)**

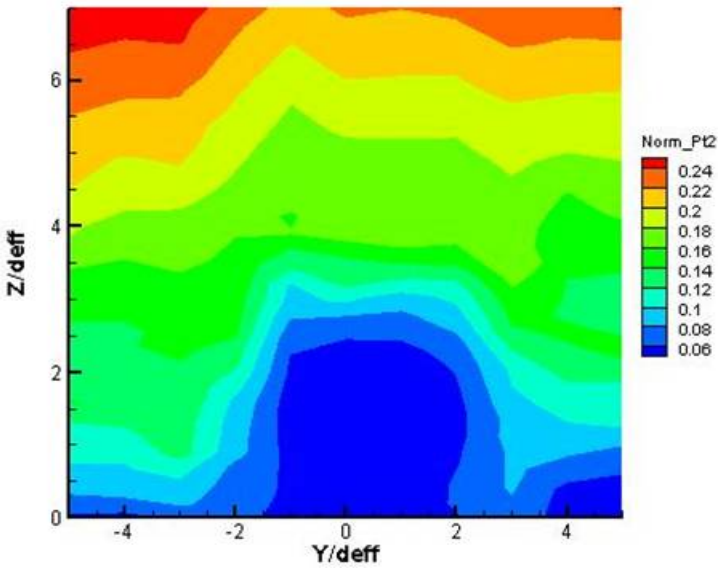


Figure 6.13: **Normalized Pitot Pressure in the (y-z plane) at $x/d_{eff} = 16.4$ :Case 3 (Shock at $x/d = 16$)**

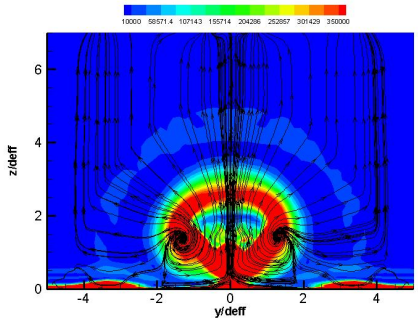


Figure 6.14: NoShock at 4

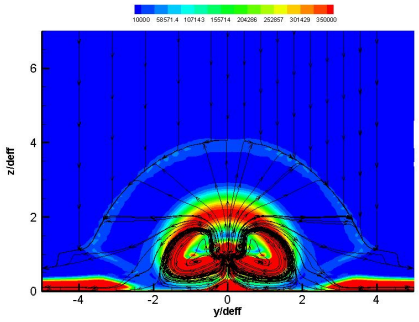


Figure 6.15: Shock 2 at 4

vor1

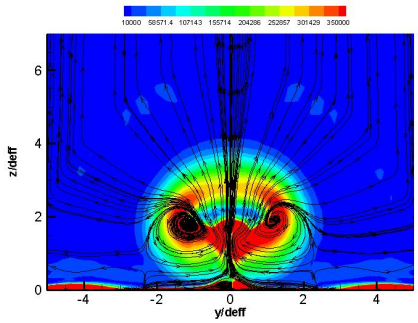


Figure 6.16: NoShock at 6

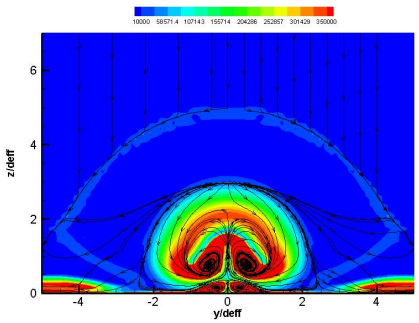


Figure 6.17: Shock 2 at 6

vor2

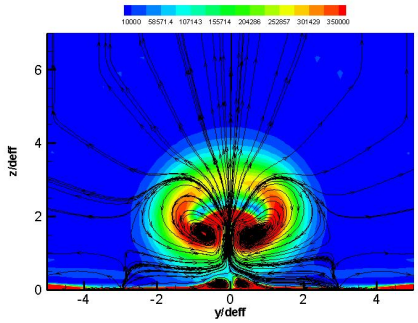


Figure 6.18: NoShock at 8

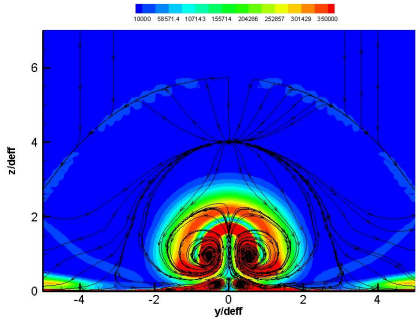


Figure 6.19: Shock 2 at 8

vor3

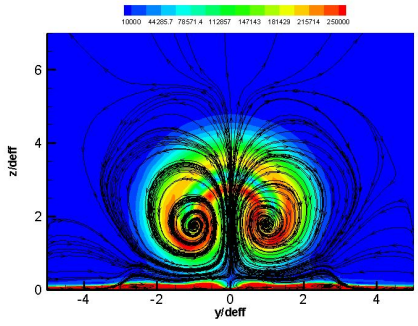


Figure 6.20: NoShock at 16

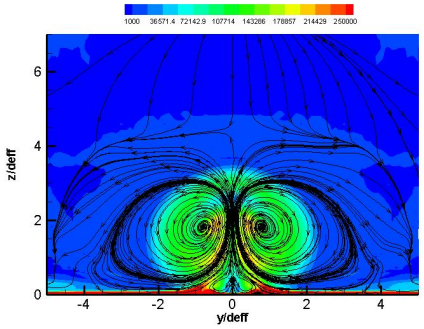


Figure 6.21: Shock 2 at 16

vor4

# Chapter 7

# Vortex Interactions with a Jet in a Supersonic Crossflow

## 7.1 Overview

This study is concerned with the interaction of the usual vortex structure produced by jet injection into a supersonic crossflow and an additional axial vortex typical of those that might be produced by the inlet of a scramjet or the forebody of a vehicle to be controlled by jet interaction phenomena. The cases treated are for sonic, heated Helium injection from a circular jet inclined at 30 degrees to a Mach 4 flow at high Reynolds number conditions. The additional axial vortex is generated by a strut-mounted, diamond cross-section wing mounted upstream of the injection location

In general, low speed wing tip vortices have been found to exhibit tangential velocity distribution similar to a Burger's vortex, in combination with a wake-like streamwise velocity distribution. The streamwise velocity deficit in the vortex core is attributed to the momentum deficit in the boundary layer on the wing. On the other hand, studies of streamwise supersonic vortices are scarce in the literature (Smart et al.,[52,53] and Milanovic[54]). To the author's knowledge, the current investigation is the first attempt to measure the detailed flow structure originated by supersonic freestream vortex interactions.

## 7.2 Vortex Dynamics Considerations

The behavior of the counter-rotating vortex pair created in the plumes of jets in a cross-flow is a key feature of fuel injection and mixing in scramjets and other jet interaction applications. It is, therefore, of interest to understand how additional vortex structures might interact with the vortices in the jet plumes. Concepts of vortex dynamics were used to conduct some preliminary studies for idealized cases. The 3D, steady case was represented using an analogy with the 2D, unsteady case. Marble[42] suggested this same analogy in a different, but related situation. Let's consider a lifting line of length equal to 2, placed along the y-axis in z=0 plane, from y = -1 to y = 1 ( Figure 7.1)

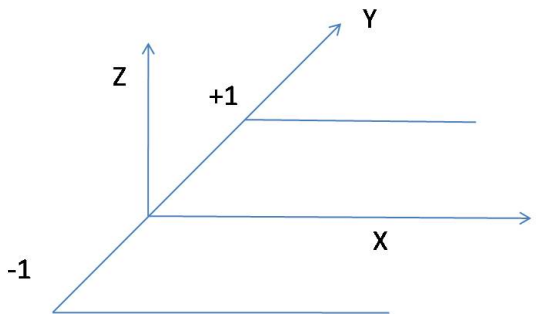


Figure 7.1: **The horseshoe vortex in supersonic flow**

It is possible to show that the potential of the lifting line can be expressed in the form

$$\phi = \frac{\Gamma}{2\pi} tan^{-1} \frac{x\,(y-1)}{z\sqrt{\Omega}} \tag{7.1}$$

where $\Gamma$ is the circulation and $\Omega$ defined as: $\Omega = x^2 - (\sqrt{M^2-1})^2\left[(y-1)^2 + z^2\right]$. The potential is other than zero only within the two Mach cones arising at the end of the lifting line, while it is zero in the other remaining space. The velocity components corresponding to the potential can be easily found. If, for example, we consider the component $w$ in the z direction we obtain:

$$w = \frac{\partial \phi}{\partial z} = \frac{\Gamma}{\pi} \frac{x(y-1)(\Omega - (M^2-1)z^2}{\pi\left[z^2\Omega + (y-1)^2\,x^2\right]\sqrt{\Omega}} \tag{7.2}$$

The important observation is that near the axis of the vortex the velocity components

as the one in Equation 7.2 behave exactly as in the zone near a vortex filament in incompressible flow. Therefore, the induced velocity in zones far behind the wing ( exactly at $x = \infty$ or in the case of the 2D analogy suggested by Marble[42]) can be determined with the equation of Biot-Savart for incompressible flow (Ferri[55]).
Consider a simple case where an axial vortex passes close to the side of the plume from the jet. The jet plume can be idealized as a pair of counter-rotating axial vortices, and the strength of these vortices was calculated after a complete five-hole probe survey. The equations of motion for $N$ interacting point vortices in the bounded plane (y-z) consists of $4N$ first order, nonlinear, ordinary differential equations. To gain an understanding of the possible effect of these streamwise vortex interactions, several simple simulation were studied. The main result is that the presence of an axial vortex of sufficient strength (same order of magnitude of the vortices in the CVP) and sense can have a large effect on jet penetration. In addition, the plume can be distorted, which will affect mixing. Based on these results, a wing was designed to produce a tip vortex of a strength comparable to that of one of the typical CVP found in the plume of a jet in a crossflow ($\Gamma = 1.8 m/s^2$)

## 7.3 Experimental Arrangement

The experimental arrangement is shown in Figure 7.2 and Figure 7.3. The vortex generator was a rectangular half wing with a diamond shaped cross section (6 degrees half angle), a chord length of 2 in, and span of 3.5 in. It was located 2 chords upstream of the injector center. The convention adopted for specifying the location of the wing tip with respect to the injection point is shown in Figure 7.10. The injection conditions are the same used for the study of the single-hole injector in Chapter 5.

## 7.4 Experimental Results

Some comparisons of the flow with axial vortices interacting with the jet plume in various locations are considered.

### 7.4.1 Vortex Survey

The main objective of the vortex characterization was to determine the Mach number, total pressure, and swirl distributions in the core region of the supersonic wing tip vortex. A shadowgraph of the flow in which it is possible to identify the vortex is presented in Figure 7.5. The survey of the tip vortex was conducted at a station located $16d_{eff}$ downstream of the injector. The position of the vortex is defined as the position at which the Pitot pressure was observed to be a minimum. Spanwise Pitot pressure distributions of the region of the tip vortex are shown in Figure 7.4 indicating that the tip vortex is a region of significant deficit in total pressure. The total pressure distributions reach a minimum at approximately $7mm$. Figures 7.6 to 7.8 show the Mach number distributions. For the geometry of the current experiments, $M_x$ may be interpreted as swirl component of the Mach number. The distribution shows a similarity to the work of Smart[52] with an inner linear swirl distribution, surrounded by a region with swirl similar to an irrotational vortex. The point with zero swirl corresponds with the vortex axis. It is noted, however, that the profile is not symmetric but shows a larger swirl outboard of the half-wing . This asymmetry, is also typical of low-speed flow wing tip vortices. The average core diameter was observed to be of $4mm$. Figure 7.7 shows the spanwise component of the Mach number $M_y$. In order to interpret the observed distribution, it is worth noting that this shows the radial Mach number component in the vortex core in combination with the wake.

Figure 7.8 shows the distribution of the streamwise Mach number. A significant Mach number deficit is observed to occur in a small region near the axis of the vortex. The wake-like profile reaches a minimum of $M = 1.77$. Again, the wake-like streamwise Mach number distribution observed in this experiment is similar to those found in Milanovic[54] and Smart[53] and is attributed to the momentum deficit in the wing's boundary layer. Streamwise Mach number deficits of this magnitude have important implications for the vortex interaction studies. Based on the results presented above, the magnitude of the swirl angle is $\tau$ is plotted in Figure 7.9. As noted earlier, the vortex is not symmetric, leading to a peak swirl angle of 10.5 degrees.

The vortical flow in the jet plume alone is documented in Figure 7.15 as measured with the five-hole probe. It is believed that this is the first such data for a jet in a supersonic crossflow.

### 7.4.2 Mass Fraction Contours

Helium concentration data is presented in the form of mass fraction contours. Consider first the case in Figure 7.11 where the tip of the vortex is at $x = 2d_{eff}$ and $h = 1d_{eff}$. The core of the jet, defined as the maximum helium mass fraction, is located at approximately $y/d_{eff} = 1$ at an elevation of $z/d_{eff} = 2.5$. The maximum concentration is $\alpha = 0.78$. The plume width extends for $9d_{eff}$. From the picture, it is clear that there is a tremendous distortion of the counter-rotating vortex pair (CVP) that, in absence of the wing tip vortex, usually manifest itself with the classic horse-shoe shape as described in Chapter 5. In Figure 7.12, in which the tip of the vortex generator is located at $x = 4d_{eff}$ and $h = 1d_{eff}$ shows a lower penetration than the previous case. The plume is shifted in the left direction and it appears that the CVP formation, even if inhibited by the additional vortex, occurs. The maximum concentration is found at an elevation of $z/d_{eff} = 2.1$. Figure 7.13 and Figure 7.14 show the effects of the tip of the vortex generator at $x = 0$ with $h = 2d_{eff}$ and $h = 1d_{eff}$, respectively. The small variation in the position of the wing resuls in a completely different morphology of the mass fraction dstribution. In fact, in Figure 7.11 there is an entrainment effect and in Figure 7.12 we can identify a partial rotation of the plume, with the same sense of the circulation of the vortex, which results in the lifting of the right side.

### 7.4.3 The complete flowfield

A complete conical probe survey was obtained for the case with the tip of the vortex generator at $x = 2d_{eff}$ , $h = 1d_{eff}$ selected as an interesting case. The interesting feature to note is the entrainment process, driven by the wing tip vortex that occurs in the left side of the Figure 7.17. Figure 7.16 shows that the strong influence of the wing tip vortex results in an inhibition of the right side of the CVP and a reduction of the strength of the left component compared with the baseline case. This can help to explain the fact that the maximum concentration in the plume is almost twice of the base case without vortex.

### 7.4.4 Summary

The main conclusions drawn from these studies are as follows:

1) The generated wing tip vortex has a circulation of $\Gamma = 1.6m^2/s$ and a maximum swirl angle of 10.5 degrees. These were the values we were planning to investigate.

2) A wake-like streamwise Mach number distribution was observed but the vortex vas able to sustain the bow shock generated by the injection in the supersonic stream. It is well known that a wake-like profile decreases the critical Mach number at which vortex bursting occur

3) The results show a higher value of the helium maximum concentration in all the cases investigated with an addiction of an axial vortex, accompanied by a profound influence in the jet's plume morphology.

4)The flow field survey shows that an incoming axial vortex can dramatically influence the formation of the usual jet counter-rotating vortex pair (CVP), resulting in an asymmetry.

5)The combined flow field survey and concentration measurements show that an important entrainment driven by an axial vortex occurs and results in a higher penetration with a wider jet plume compared to the case without a vortex.

6) A simple model such as the line vortex cannot be representative in a situation in which the CVP in this early stage of formation is so strongly affected by an axial vortex. In addition, the potential theory implies a nearly uniform streamwise velocity, and the data shows that this velocity component defect is not negligible.

7) The experimental fact that in the measurement plane the maximum helium mass fraction is higher than the baseline case doesn't define much about the further downstream development. The dynamics and consequently the mixing can accelerate once the

reorganization of the vortical flow is completed.

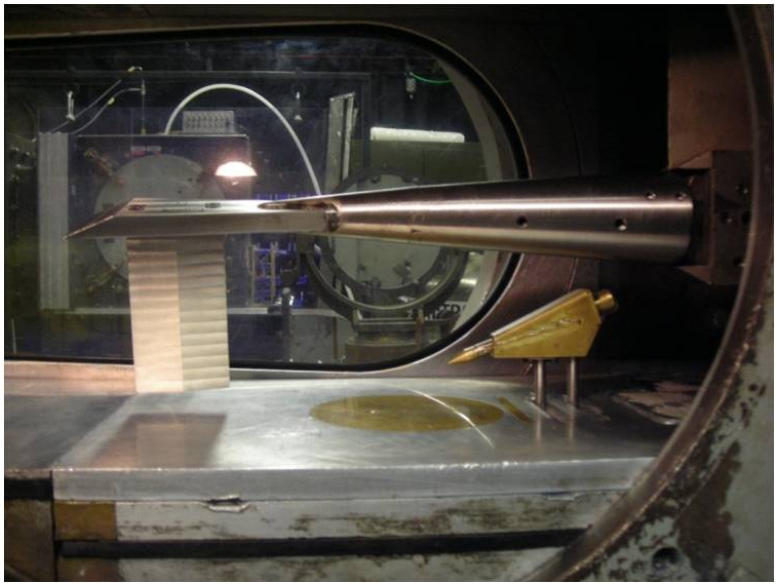

Figure 7.2: **Vortex generator and concentration probe**

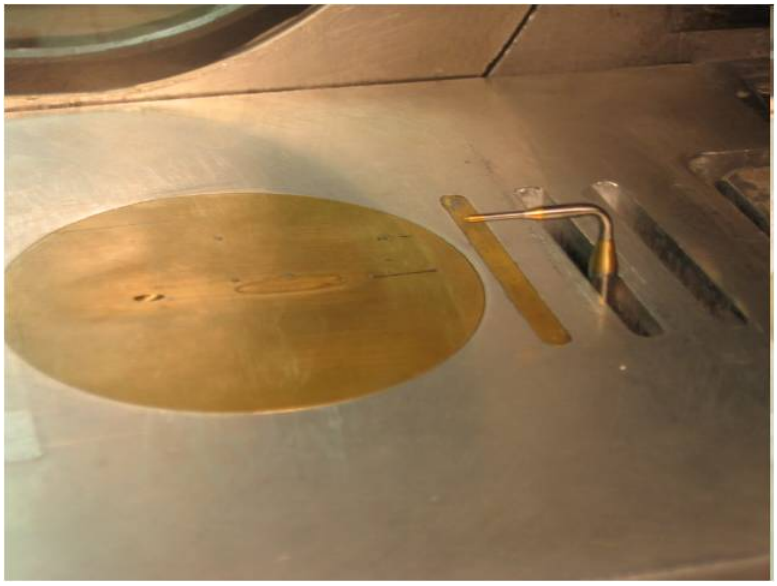

Figure 7.3: **Detail of the conical five hole probe used for the vortex survey**

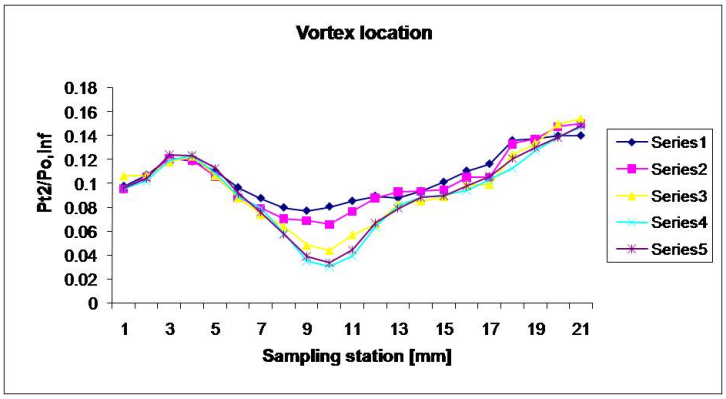


Figure 7.4: **Pitot pressure distributions used to locate the vortex**

Figure 7.5: **Shadowgraph of the wing tip vortex**

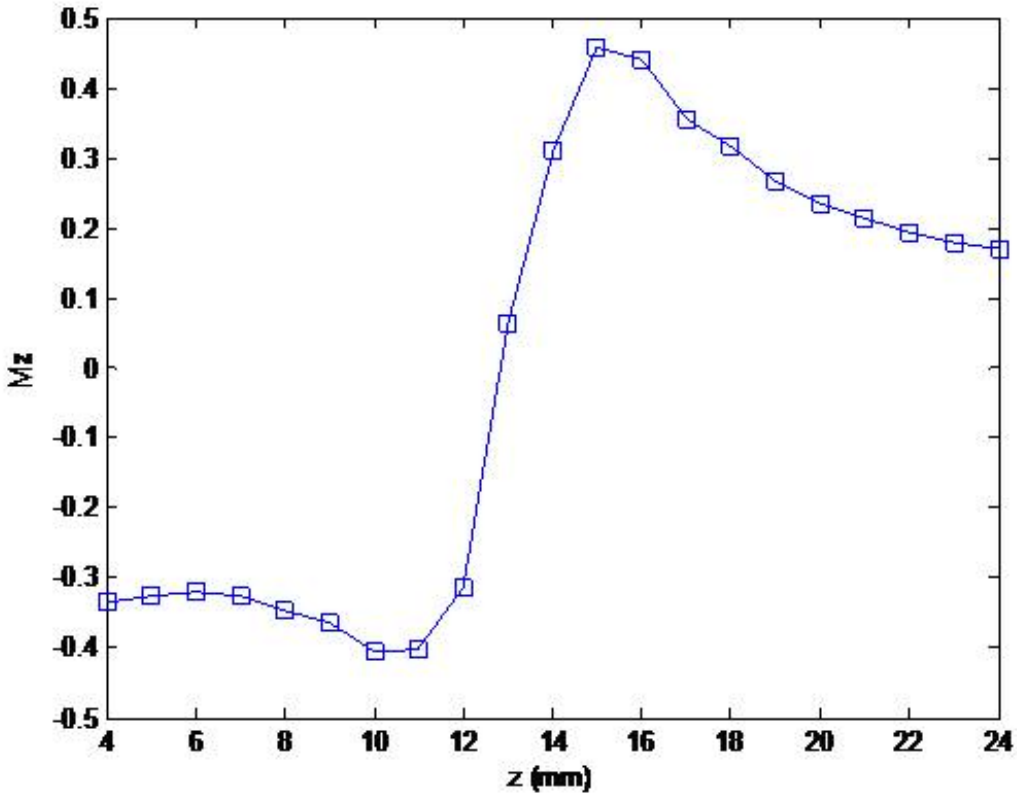


Figure 7.6: **Swirl Mach number,** $Mz$

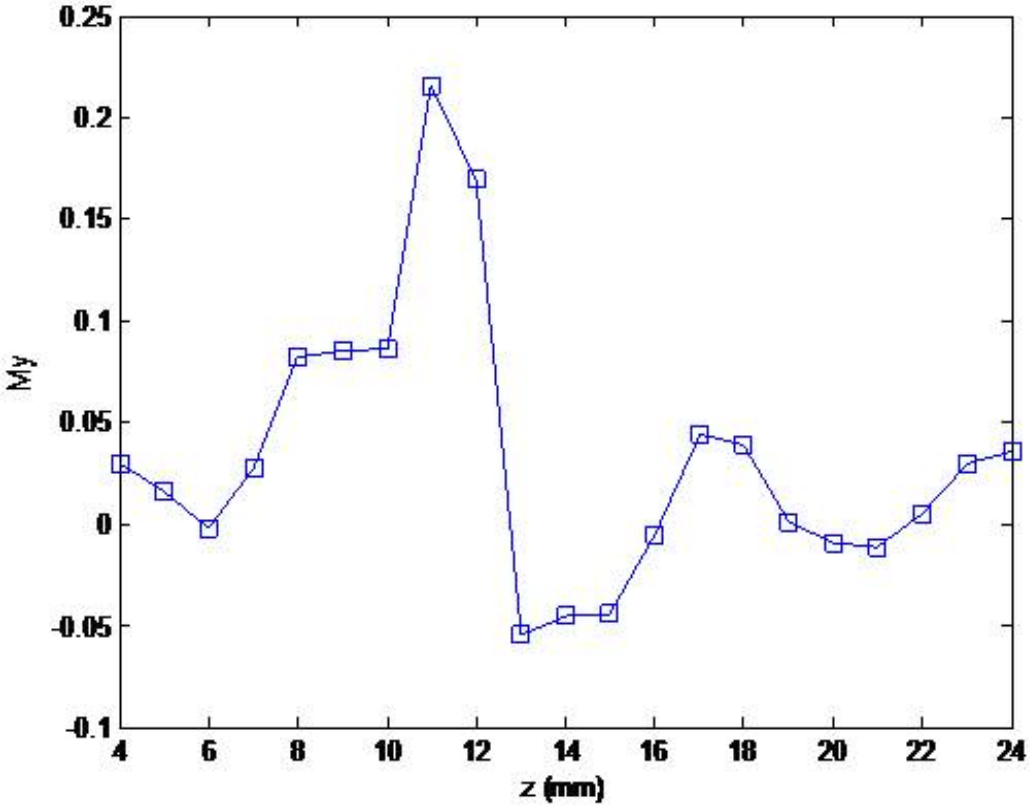


Figure 7.7: **Spanwise Mach number,** $My$

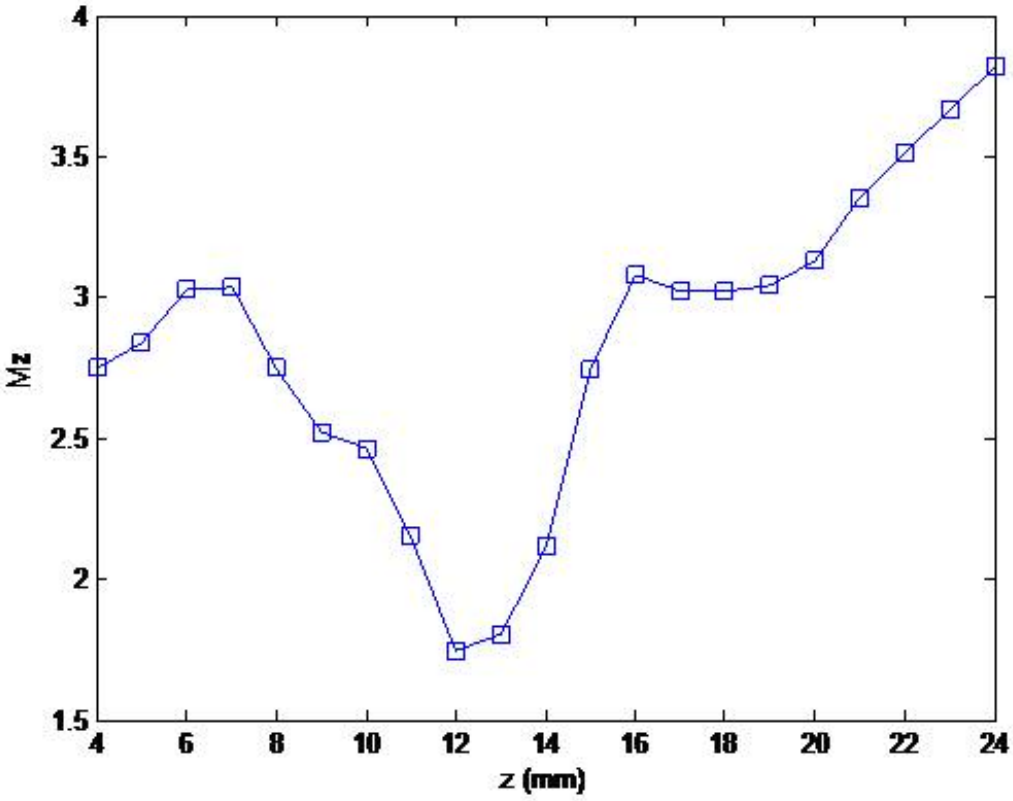


Figure 7.8: **Streamwise Mach number**

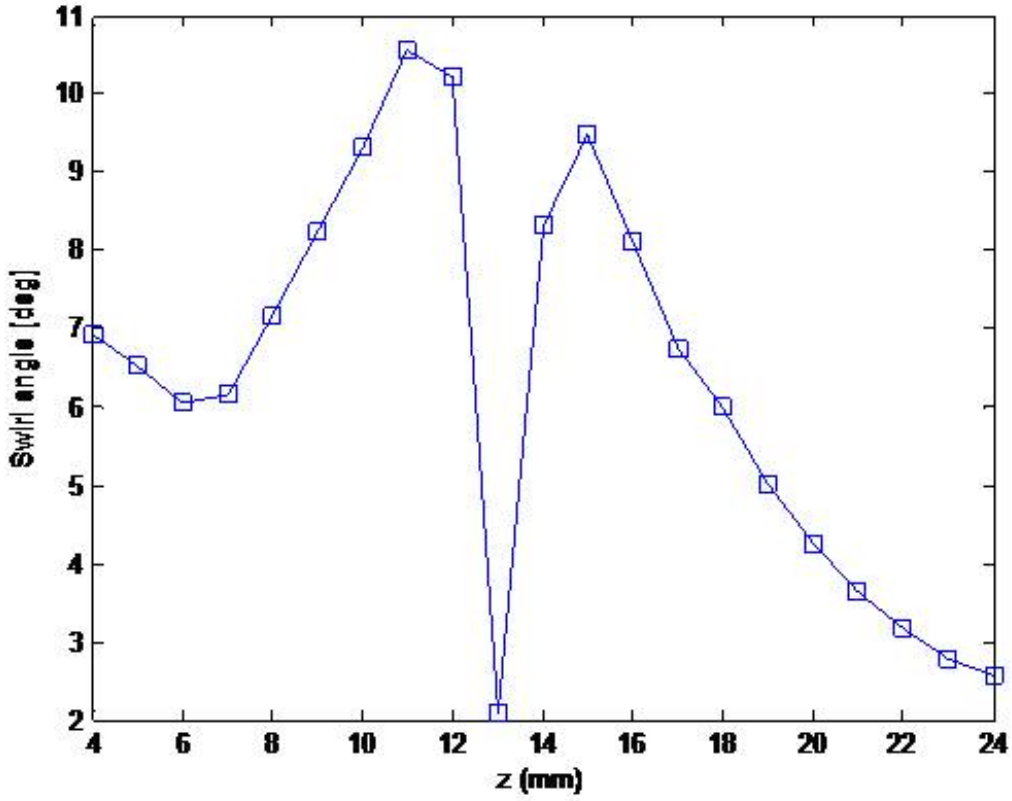


Figure 7.9: **Swirl angle distribution in the vortex core**

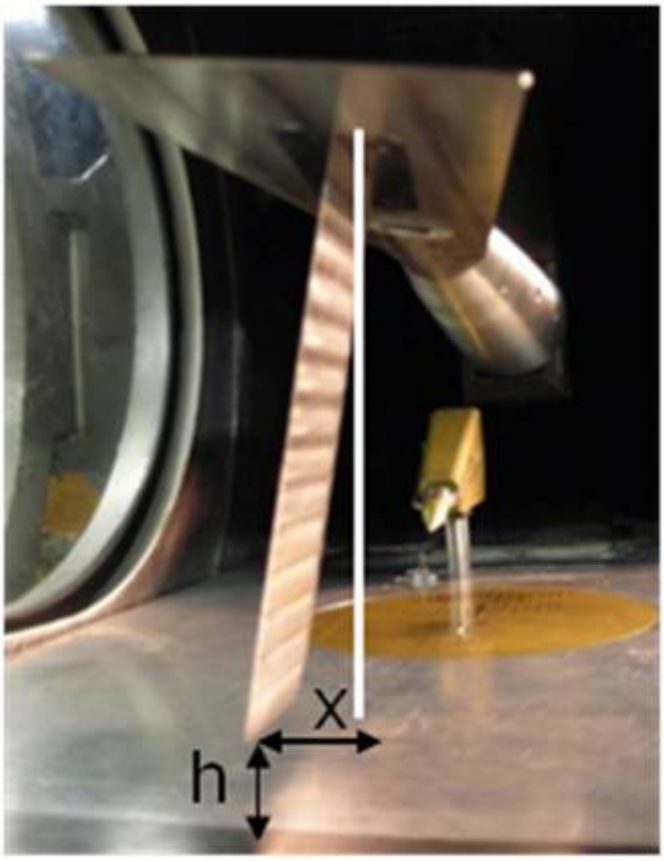


Figure 7.10: **Wing tip position. The adopted reference system**

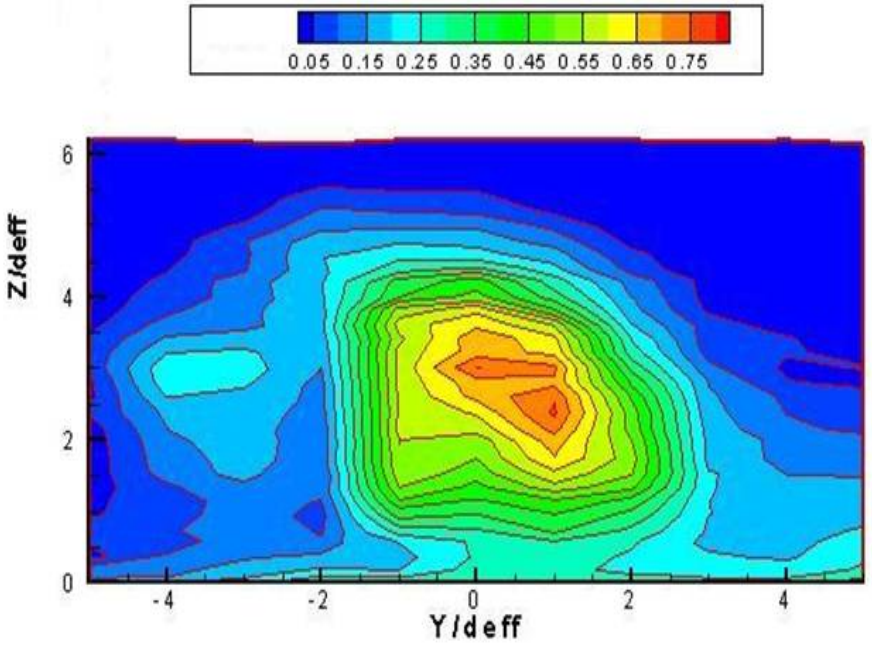


Figure 7.11: **Mass fraction contours for the case x=2 $d_{eff}$ and h= 1 $d_{eff}$**

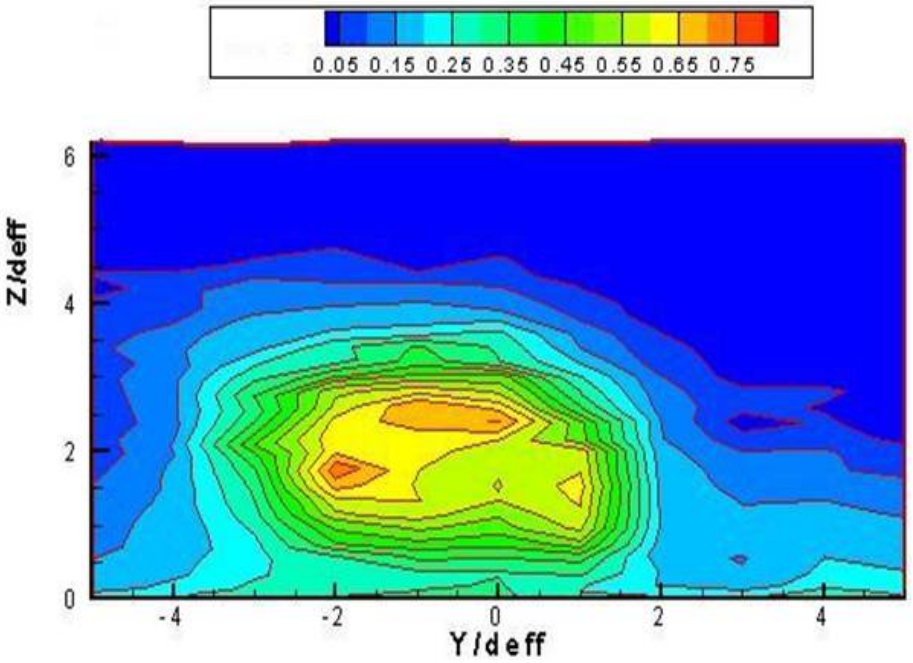


Figure 7.12: **Mass fraction contours for the case $x = 4d_{eff}$ and h= 1 $d_{eff}$**

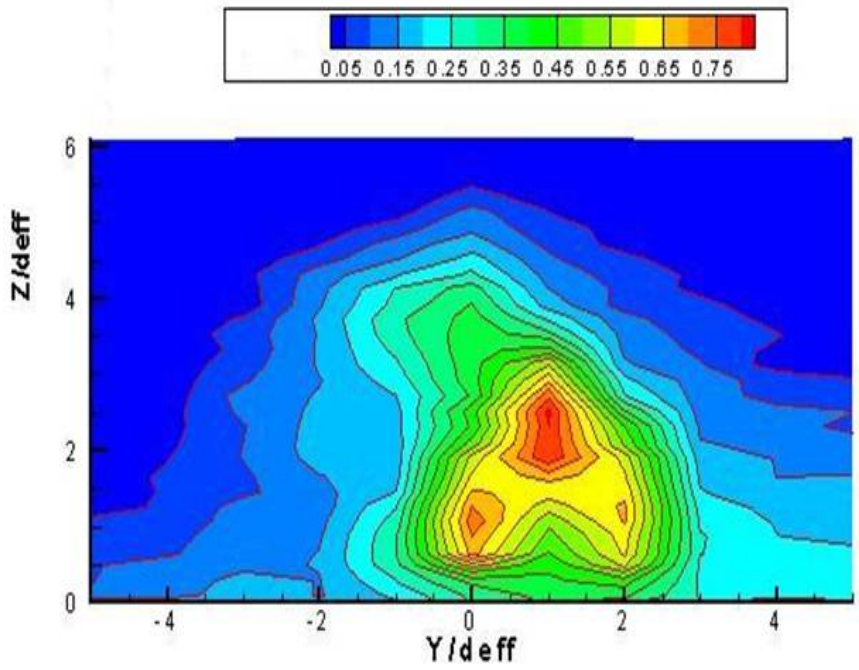


Figure 7.13: **Mass fraction contours for the case x=0 $d_{eff}$ and h= 2 $d_{eff}$**

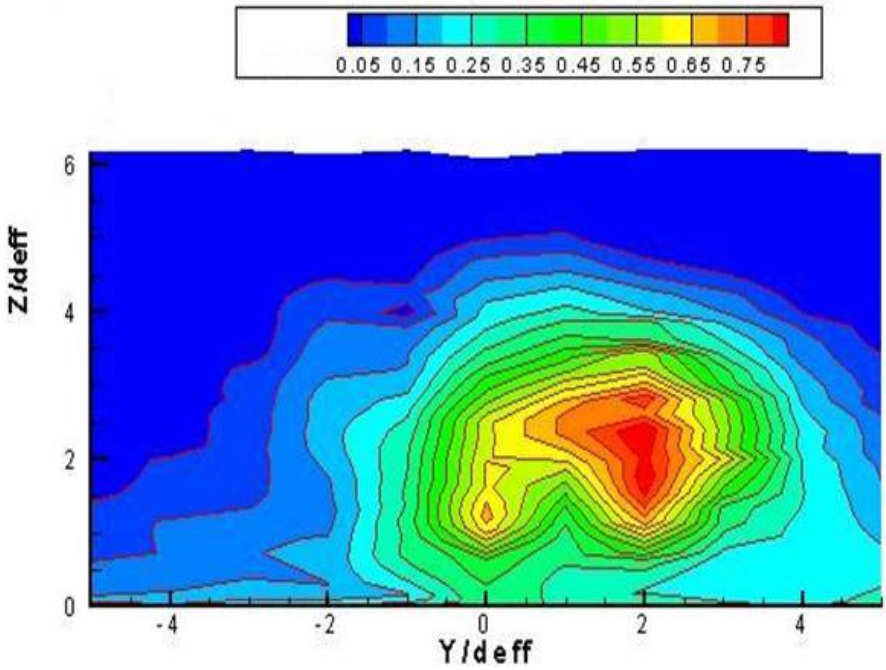


Figure 7.14: **Mass fraction contours for the case x=0 $d_{eff}$ and h= 1 $d_{eff}$**

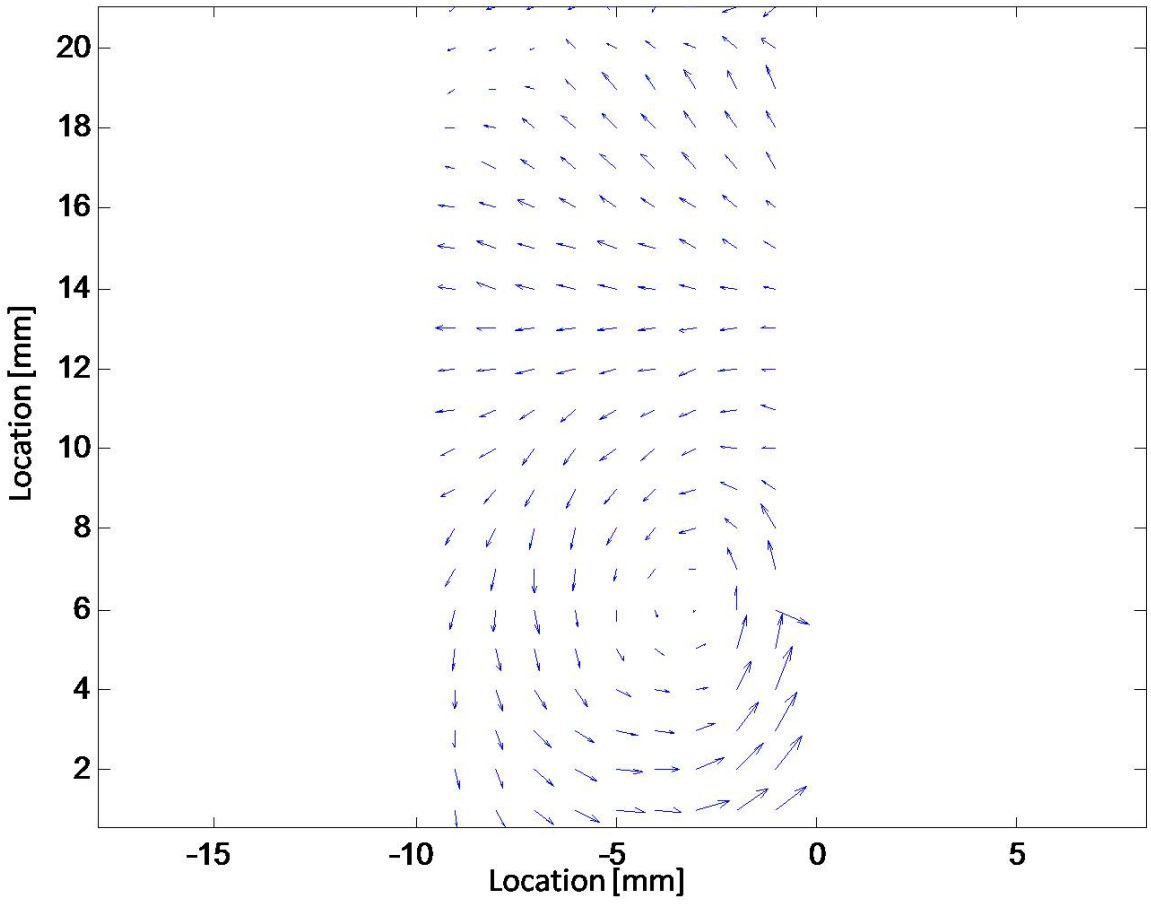


Figure 7.15: **The result of the base case CVP five-hole probe survey ( left plane only)**

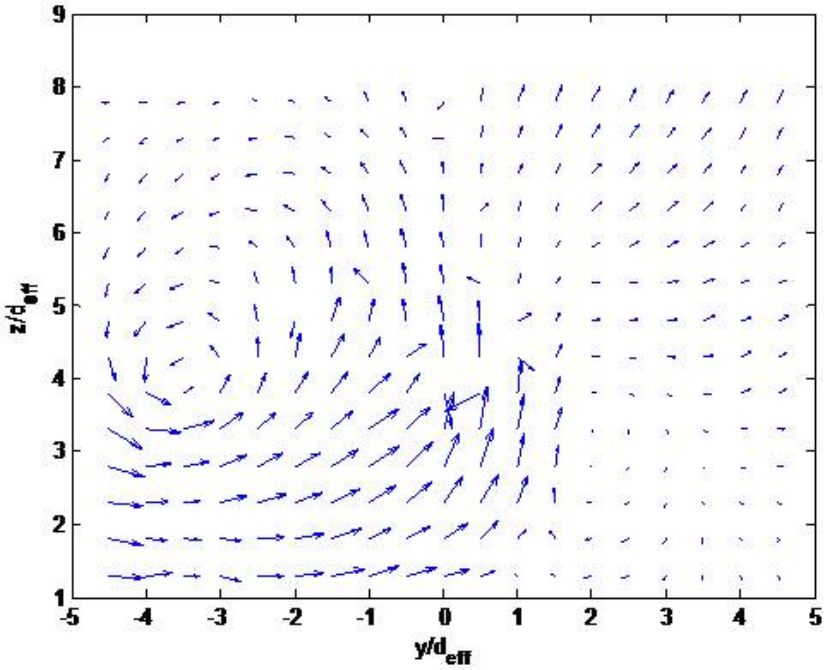


Figure 7.16: **The complete CVP and wing tip vortex interaction flowfield**

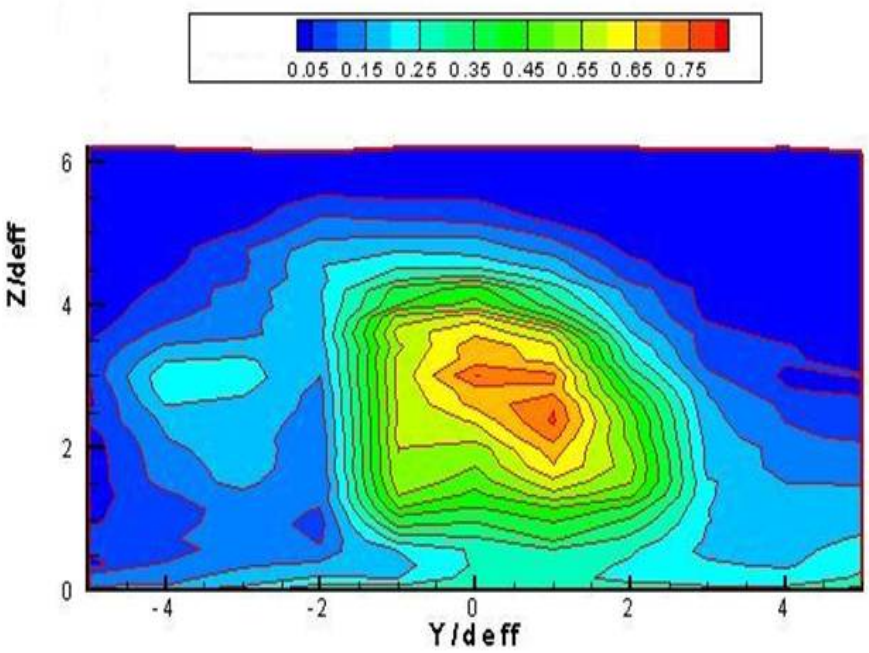


Figure 7.17: **Mass fraction contours for the case x=2** $d_{eff}$ **and h= 1** $d_{eff}$

# Chapter 8

# Conclusions

## 8.1 Overview

The first set of experiments performed were aimed to investigate the flowfield near a four-hole aeroramp injector previously developed and studied by Jacobsen for hydrocarbon gas injection into a Mach 2.4 airstream. The aeroramp was compared to a single low-angled circular injector. Both injectors were exposed to a Mach 4 cross stream with heated helium as the injectant to simulate hydrogen. Helium concentration, Pitot pressure, total temperature and cone-static measurements were taken during the mixing studies. From the measurements, helium mass fraction contours, Mach number, total temperature and total pressure plots were generated. From this data, penetration of the helium injectant core, total pressure losses and mixing efficiency were calculated. The main conclusions drawn from these studies are as follows:

1) The mixing efficiency value of the aeroramp was only slightly higher than that of the single-hole injector at these conditions.

2) The aeroramp injector showed somewhat higher local total pressure losses at some places in the plume than the single-hole injector. This was due to the higher angle of injection of the first row of the aeroramp array and the multiple shock structures from the two rows of jets. Although the local total pressure losses appeared more substantial, the mass averaged total pressure loss parameter showed that the aero-ramp had the same

overall losses in the area studied.

3) The aeroramp had a plume area comparable with the plume area of the single-hole injector. The aeroramp produced a larger amount of lateral mixing. This was due to the greater cross-stream distance between the individual injector holes.

4) The core of the jet, i.e. maximum helium mass fraction, was higher for the single-hole injector as expected considering the higher momentum value in the z direction. The plume center of mass was higher for the aeroramp injector.

5) The present aeroramp was optimized for the injection of ethylene in a Mach 2.4 crossflow. Further development may include a study of the optimization of the aeroramp injector design for higher Mach number conditions with light gas injections.

The natural extension of the investigation was then to look in detail at two major physical phenomena that occurs in a complex injector design such as the aeroamp as well as in scramjet combustors in general: (1) the jet-shock interaction and (2)the interaction of the vortical structures produced by the jets injection into a supersonic cross flow with additional axial vortices. The important conclusions from these investigations are summarized below.

For the jet-shock interaction case, experimental studies were performed to investigate the effects of impinging shocks on injection of heated helium (simulated hydrogen) into a Mach 4 crossflow. Helium concentration, Pitot pressure, total temperature and cone-static measurements were taken during the mixing studies. From the measurements, helium mass fraction contours, Mach number, total temperature and total pressure plots were generated. From this data, penetration of the helium injectant core and mixing efficiency were calculated. The main conclusion drawn from these studies are as follows:

1) The addition of a shock behind gaseous injection into a Mach 4 crossflow enhances mixing by deposition of baroclinic generated vorticity.

2) The closer the shock to the injection point, the larger the effect on mixing and vortic-

ity. The earlier the reflected shock intersects the jet, the less stable is the original vortex pair and the greater is the influence and the magnitude. Due to the vectorial nature of the vorticity, the deposition of new voticity can be suppressed by vorticity of opposite sign already present in the flow. In the early stage of the CVP formation, in which the vorticity is not yet organized in two strong poles, this suppression is minimal.

2) The results show no benefit from the impinging shock far from the injection point compared to the baseline case. This result is important because clearly imply that another method of mixing enhancement has to be utilized in the far field.

3) In a joint effort with the numerical partner the vorticity jump across the shock was calculated and the largest change in vorticity occurred with the shock intersecting the jet closest to injection.

4)The vortex dynamics analysis helped in the interpretation of the results and showed faster mixing for the cases with shocks. In particular the vortex dynamics analysis was useful in order to understand the mechanism of the voricity allocation process and the subsequent partition and dynamics.

The final investigation concerned with the interaction of the usual vortex structure produced by jet injection into a supersonic crossflow and an additional axial vortex typical of those that might be produced by the inlet of a scramjet or the forebody of a vehicle to be controlled by jet interaction phenomena. The cases treated are for sonic, heated Helium injection from a circular jet inclined at 30 degrees to a Mach 4 flow at high Reynolds number conditions. The additional axial vortices are generated by a strut-mounted, diamond cross-section wing mounted upstream of the injection location. The wing was designed to produce a tip vortex of a strength comparable to that of one of the typical counter-rotating vortex pair (CVP) found in the plume of a jet in a crossflow. For this purpose a separate study of the detailed vortex structure produced by jet injection into a supersonic crossflow was conducted. The main conclusions drawn from these studies are as follows:

1) The generated wing tip vortex has a circulation of $\Gamma = 1.6m^2/s$ and a maximum swirl

angle of 10.5 degrees. These were the values we were planning to investigate based on the results of the five-hole probe measurements of the CVP in the plume of the baseline case and the numerical simulations based on the considerations presented in chapter 7.

2) A wake-like streamwise Mach number distribution was observed but the vortex vas able to sustain the bow shock generated by the injection in the supersonic stream. It is well known that a wake-like profile decreases the critical Mach number at which vortex bursting occurs.

3) The results show a higher value of the helium maximum concentration in all the cases investigated, accompanied by a profound influence in the jet's plume morphology. The CVP is responsible of the entrainment-stretching-mixing process which dominates the near field mixing. The counter-rotating vortex pair disruption or inhibition translates immediately in a reduction of mixing.

4)The flow field survey shows that the incoming axial vortex can dramatically influence the formation of the jet counter-rotating vortex pair (CVP), resulting in an asymmetry due to the different amount of vorticity present in the CVP. This partition of the vorticity in the counter-rotating vortex pair leads to a mutual interference between the vortices and can help to explain the plume conformation.

5)The combined flow field survey and concentration measurements show that even if the CVP formation is inhibited by the axial vortex, resulting in a higher value of the helium maximum concentration, an important entrainment driven by the wing tip vortex occurs and results in an higher penetration with a wider fuel plume compared to the case without a vortex.

## 8.2 Recommendations for Future Work

The profound interaction of supersonic vortices supported by a quantitative description and characterization of the flowfield has been demonstrated. The recommendation of further studies is inevitable.

Additional experimental work is necessary to expand the preliminary set of results obtained in this work in relation to the interaction of supersonic vortices. An additional and complementary investigation is also necessary to quantify the shock-vortex interaction based on the vortex scale besides its intensity. Computational simulations can provide additional insight into the physics of such interaction and an optimization method for the supersonic vortices interaction could be approached.

Oblique shock wave impingement into the jet is one method to enhance the molecular mixing between supersonic air and gaseous fuel. Waves are also unavoidable in scramjets and often originate in the inlet isolator leading to the combustion zone or from ramps and the bow-shock in front of the jet in crossflow.

A better understanding of the physics behind the interaction of supersonic vortices and the shock-vortex interaction would contribute in the design of a new generation of injectors or better, in a new generation of an integrated injectors system.

# References


[1] Fry, R.S. "A century of Ramjet Propulsion Technology Evolution". *Journal of Propulsion and Power*, **20**(1), Jan-Feb 2001.

[2] Brown, G.L. and Roshko, A.R. "On Density Effects and Large Structure in Turbulent Mixing Layers". *Journal of Fluid Mechanics*, **64**(4):775–781, 1974.

[3] Dimotakis, P.E. "Turbulent Free Shear Layer Mixing and Combustion". *Progress in Aeronautics*, **137**:265–340, 1991.

[4] Papamoschou, D. and Roshko, A.R. . "The compressible turbulent shear layer: an experimental study". *Journal of Fluid Machanics*, **197**:453–477, 1988.

[5] Markovin, M.V. "Mach Number Effects on Free and Wall Turbulent Structures in Light of Instability Flow Interactions", 1970 Springer-Verlag, November, 1990.

[6] Papamoschou, D. "Communication Paths in the Compressible Shear Layer", AIAA paper 90-0155, January 1990.

[7] Swithenbank, J.A.and Chigier, N.A. "Vortex Mixing for Supersonic Combustion", XII th Intl. Symposium on Combustion, pp 1152-1162, The Combustion Institute 1980.

[8] Povinelli, L.A. and Ehlers, R.C. "Swirling Base Injection for Supersonic Combustion Ramjets". *AIAA Journal*, **10**(9):1243–1244, September 1972.

[9] Schetz, J.A. and Swanson, R.C. "Turbulent jet Mixing at High Supersonic Speeds". *AIAA Journal*, **21**:166–173, 1973.

[10] Naughton, J.W., Cattafesta, L.N., and Settles, G.S. "An Experimental Study of the Effect of Streamwise Vorticity on Supersonic Mixing Enhancement". *AIAA paper*, (89-1815), 1989.

[11] Cutler, A.D. and Levey, B.S. "Vortex Breackdown in a Supersonic Jet", AIAA paper 91-1815, June 1991.

[12] Levey, B.S. "An Experimental Investigation of a Supersonic Vortical Flow", MS Thesys, George Washington University, 1991.

[13] Naughton, J.W., Cattafesta, L.N., and Settles, G.S. "Minuature, Fast-response Five-Hole Conical Probe for Supersonic Flowfield Measurements". *AIAA Journal*, **31**(3):453–458, 1993.

[14] Davis, D.L. "Numerical Analysis of Techniques for Efficient Generation of Vorticity in Supersonic Flow ", AIAA paper 92-0828, 1992.

[15] Northam, G.B. and Anderson, G.Y. "Ramjet Research at Langley", AIAA paper 86-0159, 1986.

[16] Waitz, I.A., Marble, F.E., and Zukoski, E.E. "A Systematic Experimental and Computational Investigation of a Class of Countoured Wall Flush Injectors", AIAA paper 92-0625, 1992.

[17] Hartfield, R.J., Hollo, S.D., and McDaniel, J.C. "Experimental Investigations of a Supersonic Swept Ramp Injector using Laser Induced Iodine Fluorescence". *Journal of Propulsion and Power*, **10**(1):129–135, Jenuary-February 1994.

[18] Riggins, D.W. and Vitt, P.H. "Vortex Generation and Mixing in Three-Dimensional Supersonic Combustors". *Journal of Propulsion and Power*, **11**(3):419–426, May-June 1995.

[19] Stouffer, G.B. and Gruber, M.R. "Further Investigation of the Effects of Aerodynamic Ramp Design Upon Mixing Characteristics", AIAA paper 99-2238, 1999.

[20] Schetz, J.A., Cox-Stouffer, S., and Fuller, R. "Integrated CFD and Experimental Studies of Complex Injectors in Supersonic Flows".

[21] Fuller, R.P. andNejad, A.S. and Schetz, J.A. "Fuel-Vortex interactions for Enhancing mixing in Supersonic Flow", AIAA Paper 96-2661, July 1996.

[22] Cox, S.K. and Gruber, M.R. "Effects of Spanwise Injector Spacing on Mixing Characteristic of Aerodynamic Ramp Injectors", AIAA Paper 98-3272, July 1998.

[23] Jacobsen, L.S., Gallimore, S.D., Schetz, J.A., and O'Brien, W.F. "Mixing Enhancement by Jet Swirl in a Multiport Injector Array in Supersonic Flow",FEDSM99-7248, July 1999.

[24] Jacobsen, L.S. , Schetz, J.A., Gallimore, S.D., and O'Brien, W.F. "Improved Aerodynamic-Ramp Injector in Supersonic Flow",AIAA Paper 2001-0518, FEDSM99-7448, July 1999.

[25] Jacobsen, L.S. , Gallimore, S.D., Schetz, J.A., and O'Brien, W.F. "Integration of an Aeroramp Injector/Plasma Igniter for Hydrocarbon Scramjets". *Journal of Propulsion and Power*, **19**(2), March - April 2003.

[26] Gruber, M., Donbar, J., Jackson, T., and Billig, F. "Performance of an Aerodynamic Ramp Fuel Injector in a Scramjet Combustor", AIAA Paper, 2000-3707, July 2000.

[27] Ben-Yakar, A. Mungal, M.G. and Hanson, R.K. "Transverse Jets in Supersonic Crossflow, Part 2: The Effect of Compressibility, Velocity Ratio and Density Ratio". Physics of fluids, submitted,2005.

[28] Schetz, J.A. "Interaction Shock Shape for Transverse Injection". *Journal of Spacecraft and Rockets*, **7**(2):143–149, February 1970.

[29] McClinton, C.R. "The effect of Injection Angle on the interaction Between Sonic Secondary Jets and a Supersonic Freestream",NASA TND-6669, February 1972.

[30] Barber, M.J., Roe, L.A., and Schetz, J.A. "Simulated Fuel Injection through a Wedge Shaped Orifice in a supersonic Flow", AIAA Paper 95-2559, July 1995.

[31] Tomioka, S., Jacobsen, L.S., and Schetz, J.A. "Interaction between a Supersonic Airstream and a Sonic Jet Injected throught a Diamond-shaped Orifice",AIAA Paper 2000-0088, January 2000.

[32] Schetz, J.A. "Injection and Mixing in a Turbulent Flow", AIAA, New York, New York, 1980.

[33] Ben-Yakar, A. and Hanson, R.K. "Ultra-Fast-Framing Schlieren System for the Study of the Time Evolution of Jets in Supersonic Flows", Experiments in Fluids.

[34] Frich, T.F. and Roshko, A. "Vortical Structure in the Wake of Transverse Jet", Journal of Fluid Mechanics, 279, 1-47.

[35] Yuan, L.L. and Ferziger, H. "Large Eddy Simulation of a Round Jet in Crossflow", Journal of Fluid Mechanics, 379, 71-104.

[36] Lee, S.H., Jeung, I.S., and Yoon, Y. "Computational Investigation of Shock-Enhanced Mixing: Application to Circular Cross Section Combustor". *AIAA Journal*, **36**(11), November 1998.

[37] Obata, S. and Hermanson, J.C. "Numerical Simulation of Shock-Enhanced Mixing in Nonuniform Density Turbulent Jets". *AIAA Journal*, **38**(11), November 2000.

[38] Smart, M.K. and Kalkhoran, I.M. "A Scenario for Oblique Shock Wave Induced Vortex Breakdown",AIAA Paper 97-0069, January 1997.

[39] Cattafesta, L.N. and Settles, G.S. "Experiments on Shock/Vortex Interactions", AIAA Paper 92-0315, 1992.

[40] Foster, J.M., Wilde, B.H.and Rosen, P.A., Perry, T.S., Fell, M., and Edwards, M.J. "Supersonic Jet and Shock Interactions". *Journal of Physics*, **9**(5), May 2002.

[41] Menon, S. "Shock Wave Induced Mixing Enhancement in Scramjet Combustors", AIAA Paper 89-0104, January 1989.

[42] Marble, F.E. , Zukoski, J.W., Jacobs, J.W., Hendricks, G.J., and Waitz, I.A. "Shock Enhancement and Control of Hypersonic Mixing and Combustion",AIAA Paper 90-1981, July 1981.

[43] Yang, J. and Kubota, T.and Zukoski, E.E. "Applications of Shock Induced Mixing to Supersonic Combustion". *AIAA Journal*, **31**(5), May 1993.

[44] Ng, W.F. , Kwok, F.T., and Ninnemann, T.A. "Concentration Probe for the Study of Mixing in Supersonic Shear Flows", AIAA Paper 89-2459, July 1989.

[45] Centolanzi, F. J. "Characteristics of a 40 degree Cone for Measuring Mach Number, Total Pressure, and Flow Angles at Supersonic Speeds",NACA TN 3967, 1957.

[46] Metwally, O.M., Settles, O., and Horstman C. "An Experimental Study of Shock Wave / Vortex Interaction ", AIAA Paper 89-0082, January 1989.

[47] Krasnov, N.F. "Aerodynamics of Bodies of Revolution", 1970 New York.

[48] Doerner S.E. and Cutler A.D. "Effects of Jet Swirl on Mixing of a Light Gas Jet in a Supersonic Airstream",NASA/CR-1999-209842, December 1999.

[49] Mao, M., Riggins, D. W., and Mc Clinton C.R. "Numerical Simulation of Transverse Fuel Injection",NASP CR 1089, May 1990.

[50] Campioli, T., Maddalena, L., and Schetz J.A. "Studies of Shock Wave/Transverse Injection Interaction on Supersonic Mixing Processes ", AIAA Paper 2006-8135, November 2006.

[51] Houwing, F., Bishop, A., Gaston, M., Fox, J., Danehy, P., and Mudford, N. "Simulated-Fuel-Jet/Shock Wave Interaction", Proceedings of the 23rd International Symposium on Shock Waves (CD version), Fort Worth, Texas, USA, July 22 -27, 2001, (Lu, F.K., ed.), ISBN: 0-9721227-0-2, p 1074-1080.

[52] Smart, M.K., Kalkhoan, I.M., and Bentson, J. "Measurements of Supersonic Wing Tip Vortices", AIAA Paper 94-2576, 1994.

[53] Smart, M.K., Kalkhoan, I.M., and Bentson, J. "Measurements of Supersonic Wing Tip Vortices". *AIAA Journal*, **33**(10), October 1995.

[54] Milanovic, I.M. and Kalhoran, I.M. "Measurements of Leading Edge Vortices in a Supersonic Stream", AIAA Paper 2000-4002, 2000.

[55] Ferri, A. "Elements of Aerodynamics of Supersonic Flows", The MacMillan C0., 1949 New York.

[56] Chernyi, H.K. "Introduction to Hypersonic Flow ", Academic. Press Inc., New York, 1961.

[57] Cheng, H.K. "Hypersonic Shock-Layer Theory of a Yawed Cone and Other Three-Dimensional Pointed Bodies",WADC TC 59-335, U.S. Air Force, Oct. 1959; Errata, June 1960.

[58] Swalley, F.E. "Measurement of Flow Angularity at Supersonic and Hypersonic Speeds with the use of a conical probe",NACA TN D-959, September 1961.

# Appendix A

# Uncertainty Analysis

The uncertainty in the pressure measured during the probe surveys , which is used in the data reduction program to determine the Mach number, total pressure, and flow angularity at a given point, is primarly du to static calibration and interpolation uncertainties. The calibration uncertainties of the measured pressures are calculated from the linear curve fits of the data, which for $P_1$ is given by:

$$U_{P_1}^2 = \frac{\sum_{i=1}^{N} \left(P_1 - \bar{P}_1\right)^2}{N} \tag{A.1}$$

Where $P_1$ is an individual calibration point and $\bar{P}_1$ is the value predicted by the linear regression. The interpolation uncertainty is approximated using the survey points, and for $P_1$ is given by

$$U_{P_1}^2 = \left(\frac{\partial\left(P_1\right)\Delta x}{\partial x}\right)^2 + \left(\frac{\partial\left(P_1\right)\Delta y}{\partial y}\right)^2 \tag{A.2}$$

Where $\Delta x$ and $\Delta y$ are one-half the distance between the data points. The total uncertainty of $P_1$ is the root sum square of Equations prima e seconda. The uncertainties in $P_2$,$P_3$,$P_4$, and $P_5$ are calculated similarly. In the data-reduction process, the accuracy of the results is largely dependent on $P_a/P_1$, where

$$P_a = \frac{P_2 + P_3 + P_4 + P_5}{4} \tag{A.3}$$

Using general uncertainty analysis it can be shown that the uncertainty of $P_a/P_1$ depends upon the uncertainty of the individual pressures, as shown by

$$\mathrm{U}_{\frac{P_a}{P_1}} = \left[ \left( \frac{U_{P_1}}{P_1} \right)^2 + \left( \frac{1}{4P_a} \right) \left( U_{P_2}^2 + U_{P_3}^2 + U_{P_4}^2 + U_{P_5}^2 \right) \right] \quad \text{(A.4)}$$

This uncertainty analysis is applied at each point where flowfield quantities are determined. Uncertainties in the original calibration are assessed to be of secondary importance to those previously discussed. The probe-tip alignment error,a bias error, is eliminated in an efficient way in particular with L-shaped probes, acquiring few calibration points with the probe rotated of 180 deg respect to the full calibration position.

Estimated uncertainties associated with the five-hole conical probe measurements are in Table A.1:

Table A.1: Estimated five-hole probe uncertainties

| Total pressure, % | Static presure, % | $M_x$% | $M_y$% | $M_z$% |
|---|---|---|---|---|
| 4 | 3 | 2 | 2 | 4 |

For the concentration probe, the uncertainty is estimated to be 7% in terms of mass fraction. This estimation was determined based on the results of a jitter program in which a 2% error in the molar fraction was assumed.

Uncertainties of the Pitot and cone-static pressure measurements were quoted as having an accurancy of 1%. This is not more valid for the cone-static in the presence of strong angularities as demonstrated by direct comparison with the conical five hole probe results. The uncertainty of the total temperature measurements was estimated to be about 2%. Table A.2 shows the measurement uncertainties of the reduced quantities:

Table A.2: Estimated uncertainties in the reduced quantities

| | Uncertainty |
|---|---|
| M | 2% |
| $\rho$ | 4% |
| $p$ | 3.2% |
| $u$ | 4% |
| T | 1.3 % |

Another source of uncertainty results from the inaccurate placement of the probe. The effect this misplacement is difficult to predict and, of course, increases the uncertainty of the computed quantities.

# Appendix B

# Transonic Free-Jet facility

A program for automatic design of a slotted transonic nozzle has been developed. The system is optimized for Mach = 1.2. In order to achieve the required flow properties for probe calibration, the characteristic network has been taken into account for the design of slots.

## B.1 Transonic Nozzle Design

### B.1.1 Design optimized for $M = 1.2$

To cover the transonic range a nozzle is used consisting of a fixed convergent contour up to the throat and a slotted cylinder from the throat, to the exit plane. Upstream of the throat the flow is accelerated smoothly to $M_a = 1.0$. The slots, distributed equidistantly on the perimeter of the cylinder should be designed in such a way that the Mach number smoothly reaches the desired supersonic level at the nozzle exit (without the over expansion problem). For a specific problem, input variables as total pressure, total temperature and throat dimension will be assigned.

## B.2 The Design method

### B.2.1 The nominal Mach number curve on nozzle axis

The nominal Mach number curve on the nozzle axis from the nozzle throat ($x = 0$; $M_a = 1$) to some distance upstream of nozzle exit ($x = l_e,\ M_a = M_{ae}$) has to be chosen. In this case a quadratic polynomial was chosen as a Mach number curve on the axis which starts with $M_a = 1$ and ends horizontally at $M_a = M_{ae}$ (fig.1):

$$M_a(x) = \frac{1 - M_{ae}}{l_e^2} x^2 + 2\ \frac{M_{ae} - 1}{l_e}\ x + 1. \tag{B.1}$$

### B.2.2 Calculation of the Flow Rate on the Axis and at the Wall from the Mach Number Distribution

The flow rate on the axis and at the wall can be calculated from the Mach number according to the following relation:

$$\rho(x)u(x) = P_0 \sqrt{\frac{\gamma}{RT_0}} M_a(x) \left[1 + \frac{\gamma - 1}{2} M_a^2(x)\right]^{\frac{\gamma+1}{2(1-\gamma)}}. \tag{B.2}$$

### B.2.3 The design mass flow in the nozzle

The design mass flow as a function of $x$ in the nozzle can be calculated from the flow rates and the nozzle cross section:

$$\mathring{m}_{design}(x) = \rho(x)u(x)A^*. \tag{B.3}$$

### B.2.4 The local mass flow leaving from the slot

The local slot mass flow which has to leave the nozzle through the slots in order to achieve the design mass flow ( and the prescribed Mach curve) is done step-by-step, beginning at $x = 0$ (Figiure B.2.4). The tunnel coordinate $x$ has been discretized dividing the overall length into $n$ points. For the arbitrary section $n$, the leaving mass flow through all the previous $(n - 1)$ points has been taken into account leading to the following iteration

process

$$\Delta q_n = \left[\rho^* u^* - Q(n)\right] A^* - \sum_{i=0}^{n-1} \rho u(i-1) \left[A_W(i-1) - A^*\right], \tag{B.4}$$

where

$$Q(n) = \rho u(n),$$

and $A_W$ is the area corresponding to the area of the contoured nozzle at the same Mach number. In order to verify the effectiveness of the routine the conservation of the total mass flow has been checked.

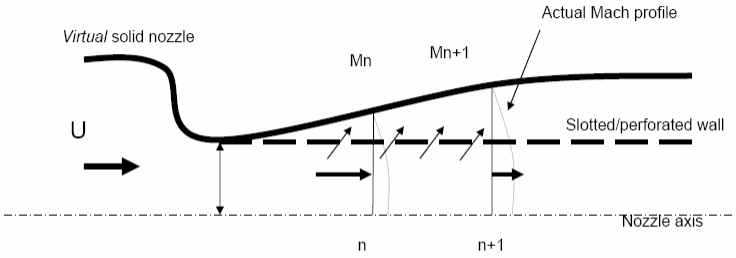


Schematic of the mass flow balance for each station. In the virtual solid nozzle contour, the Mach number is varied based on the area ratio. To obtain an equivalent Mach profile inside the transonic slotted nozzle, a certain amount of mass has to leave for each section.

Figure B.1: Design: conceptual approach

### B.2.5 Effect of the discharge coefficient

From the local slot mass flow an isentropic slot mass flow is calculated by guessing a reasonable discharge coefficient that is a function of slot thickness $t$ and width $S$:

$$C_d = f(t(x), S(x)). \tag{B.5}$$

### B.2.6 Calculation of the local isentropic flow rate through the slot

For each location $x$, an isentropic flow rate through the slot is calculated from the wall pressure inside the nozzle ( $f(M(x))$ )and the chamber pressure outside ($P_c$).

### B.2.7 Calculation of the slot area width

The required slot area can be calculated from the ratio of the isentropic mass flow through it and the local flow rate(slot). From the required open area of the slot as a function of $x$, it is now possible to calculate the slot width as a function of $x$.

$$\begin{aligned} S(x)dx &= A_{slot}(x), \\ 2\pi R dx &= A_{lat}, \end{aligned} \tag{B.6}$$

from which

$$S(x) = 2\pi R \frac{A_{slot}(x)}{A_{lat}}. \tag{B.7}$$

## B.3 Characteristic network for the correct prediction of the wall pressure

### B.3.1 Prediction of the wall pressure

The correct wall pressure prediction is especially important in the rear part of the slotted nozzle where the prescribed Mach number approaches the desired outlet Mach number Mae. Accordingly with the development of the characteristic network it is sufficient to stretch the Mach number distribution on the axis by the inclination of the characteristics.

$$\begin{aligned} \sin\mu &= \frac{1}{M}, \\ AB\sin\mu &= \frac{d_e}{2} \rightarrow AB = M\ \frac{d_e}{2}. \end{aligned} \tag{B.8}$$

Thus

$$\delta x = \frac{d}{2}\sqrt{M^2 - 1}. \tag{B.9}$$

For the correct pressure on the wall using the stretching term $\delta x$ the corresponding Mach number will be

$$M_{Wall}(x) = M_{axis}(x + \delta x). \tag{B.10}$$

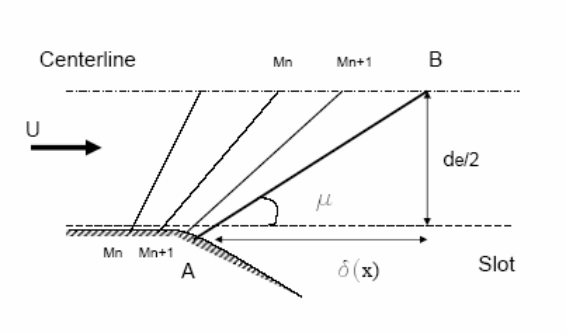


Figure B.2: Characteristic network

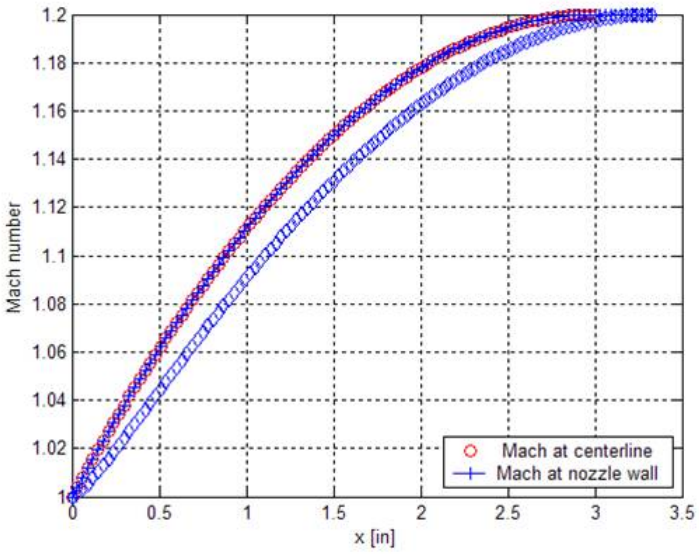


Figure B.3: Mach profile in the nozzle

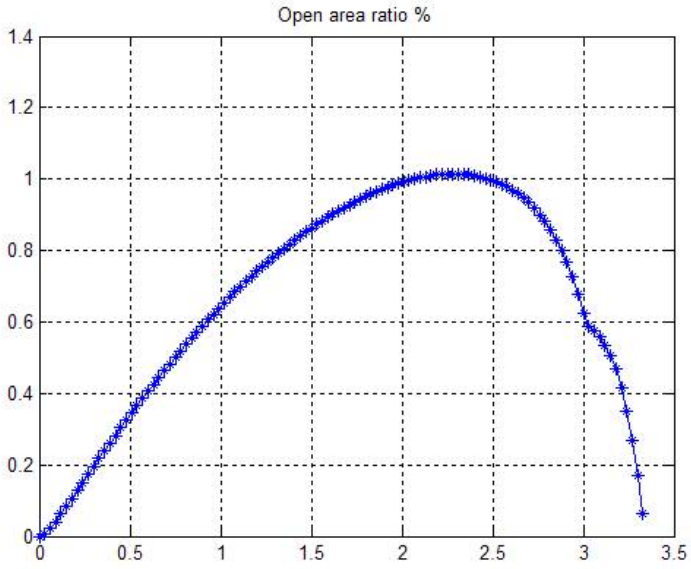


Figure B.4: Local nozzle required porosity

Figure B.5: Picture of the plenum and perforated nozzle assembly

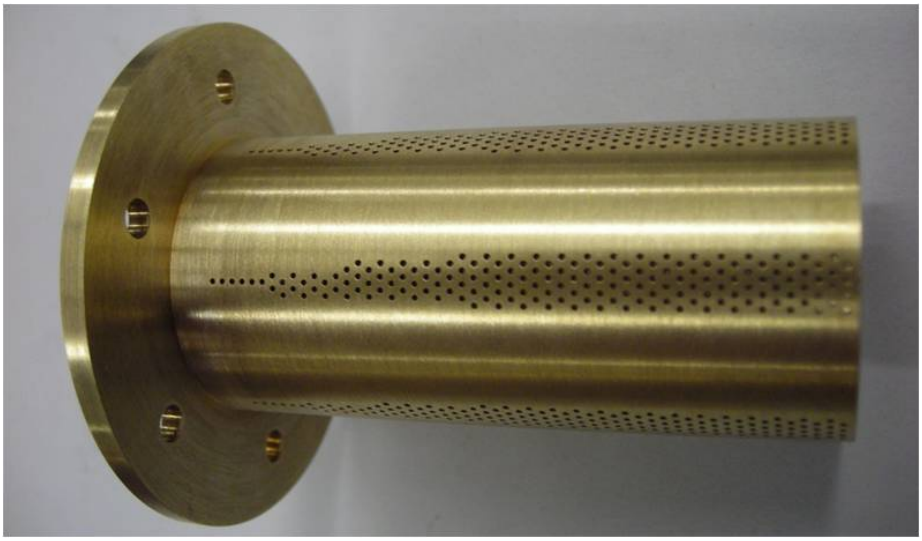

Figure B.6: The perforated transonic nozzle

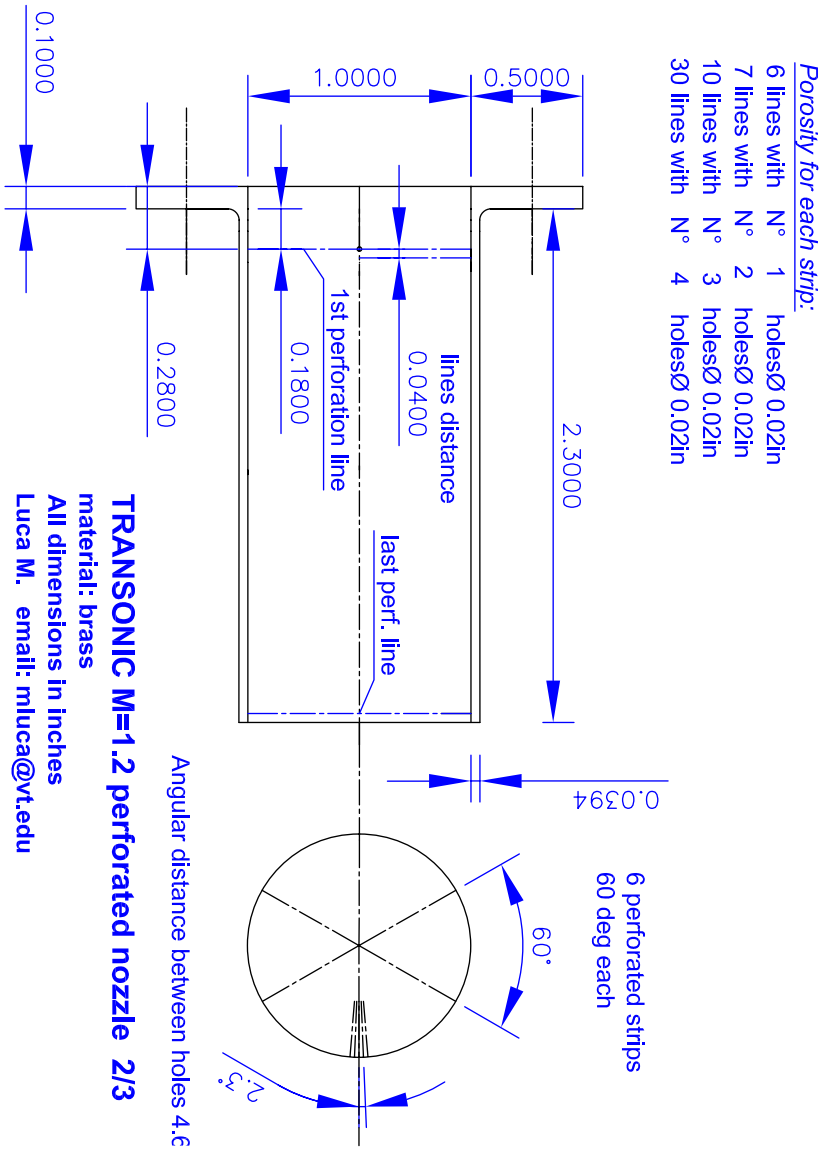


Figure B.7: Transonic 1

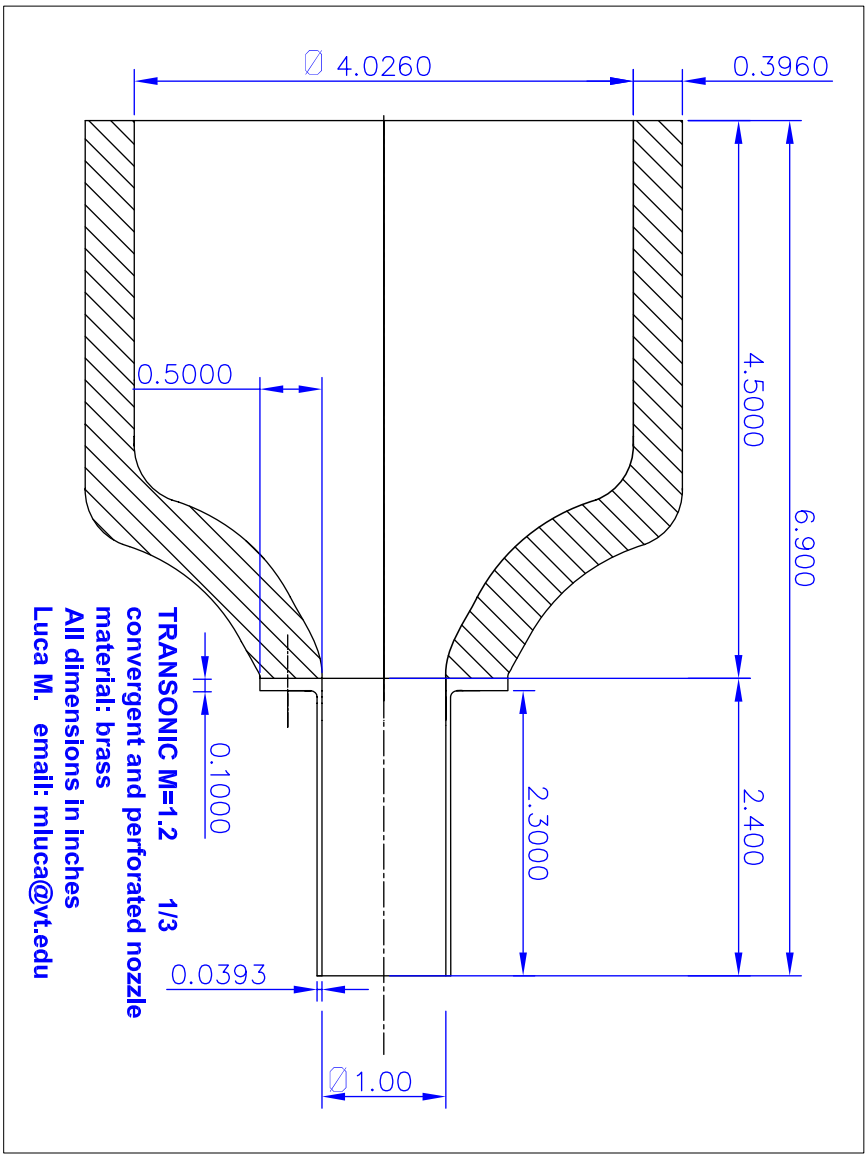


Figure B.8: Transonic2

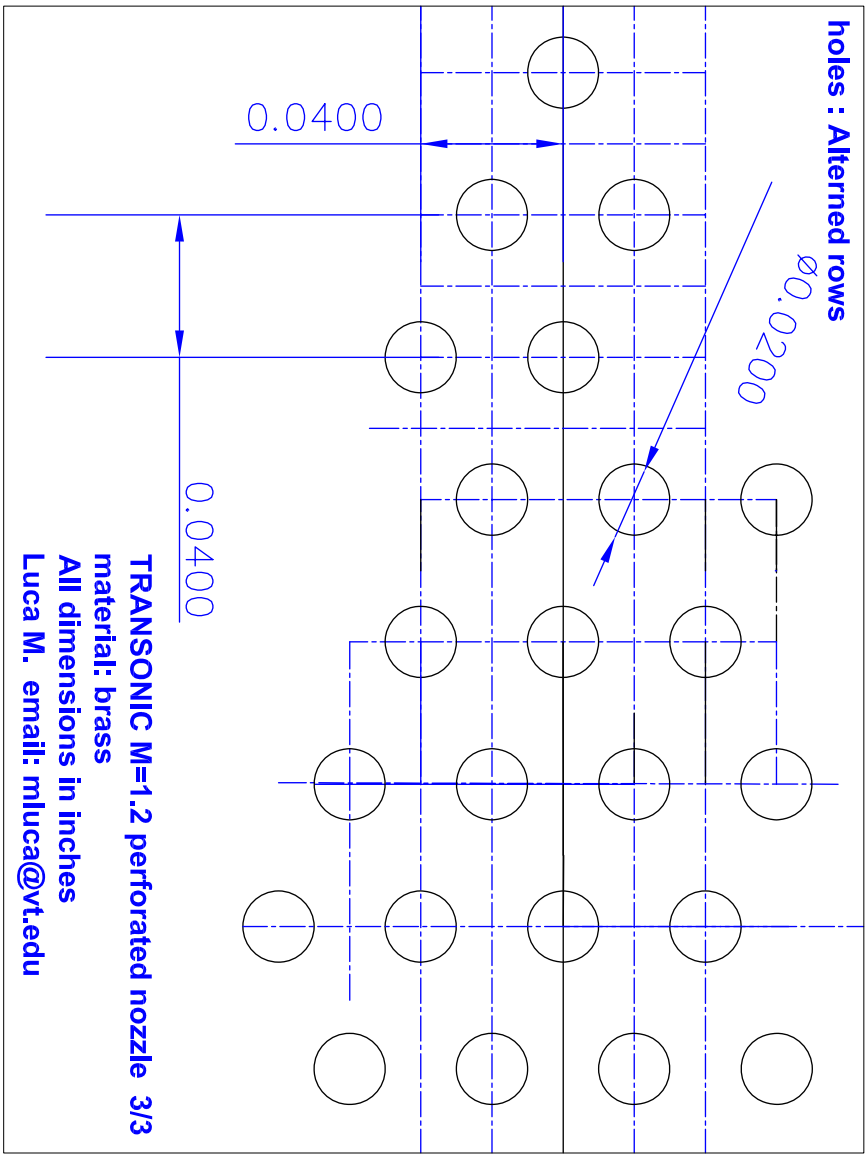


Figure B.9: Transonic3

# Appendix C

# Five-hole probe

The influence of a truncated tip on the downstream cone surface pressure distribution is examined here. Due to the corner expansion, flow around a cone with flat nose results in a lower pressure region behind the tip compared to a sharp cone of the same half-angle. Beyond this portion affected by flow expansion, the pressure distribution will quickly recover to that of a sharp cone. Therefore, the position of the surface orifices is important in determining whether the pressure taps are at a sufficient distance away to have readings as predicted by the sharp cone theory.

### C.0.2 The Flow Around a Slender Cone and the Similarity Law for Arbitrary Mach Number

Professor G. G. Chernyi[56] solved the problem of a steady flow around a slender cone at hypersonic velocity problem by using the analogy of the unsteady motion of the gas behind the cylindrical shock wave originating in front of a piston. According to this analogy, the perturbed flow around a cone is equivalent, in a lateral plane stationary with respect to the body, to the gas flow in front of a piston. For observers located in this plane, the flow is similar to the flow that originates in the propagation of an explosion wave.

Krasnov[47] (Figure C.1) indicated that for a slender blunt cone it is necessary to include the cone angle $\delta_c$ in the set of parameters that define the motion. It can be done by adding the similarity parameter $K_1 = M_\infty \delta_c$ to the number of dimensionless parameters on which the flow depends. These dimensionless parameters then determine the dimensionless

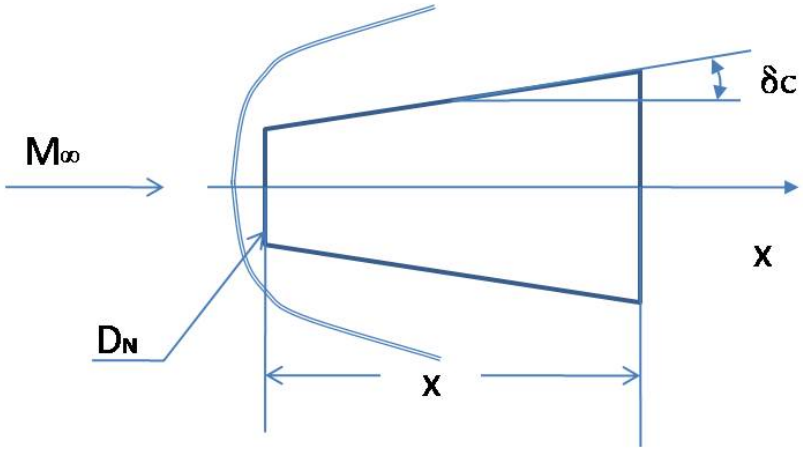


Figure C.1: Flat nose schematic

characteristics of the flow. Therefore, the pressure coefficient at the cone surface is given by the general relation:

$$\frac{C_p}{\delta_c^2} = \frac{2(p - p_\infty)}{\rho_\infty V_\infty^2 \delta_c^2} = P\left(x_*, K_1, \gamma\right) \tag{C.1}$$

Where

$$x_* = \frac{1}{M_\infty^2 \sqrt{C_{DN}}} \left(\frac{x}{D_N}\right) = \frac{1}{K_3} \left(\frac{x}{D_N}\right) \tag{C.2}$$

This can be considered the longitudinal coordinate (in a similar way Krasnov provides the similarity law for the radial coordinate of the shock wave). According to the similarity rules, the dimensionless quantity in Equation C.2 for cones having different values of $\delta_c$ and $D_N$ will be identical for equal relative coordinates $x_N$ if the similarity parameters $K_1$ and $K_3$ are maintained the same. The Krasnov universal curve, constructed on the basis of the previous considerations and using the experimental data is presented in his work. According to the similarity law, this curve can be used for the calculation of pressure for cones of different blunting.

The similarity law is not valid for the entire surface of the body. In fact, a complex phenomenon, which cannot be represented by the similarity law, is observed in the flow around a cone in the vicinity of the flat face. Flow separation occurs directly behind the corner, and a stagnant region develops. The flow eventually reattaches itself to the

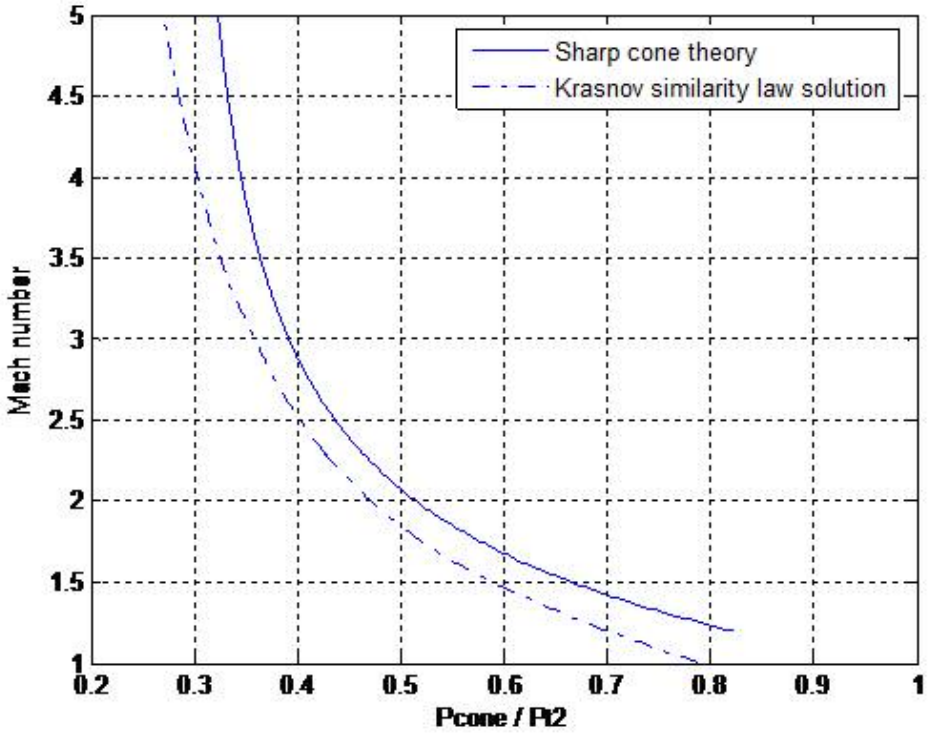


Figure C.2: Sharp cone theory results and Kasnov solution for the Naughton probe

surface. The deflection caused by the diversion of the flow in this zone is accompanied by the development of a local shock wave. The pressure decreases due to the expansion across the corner and rapidly increases passing through the shock wave. After achieving a maximum, the pressure begins to decrease again.

The overexpansion region for a flat-nose cone at zero angle of attack can be assessed by the similarity law of Krasnow. The five-hole probe used by Naughton was studied as example of prediction of the variation of the normalized average cone surface pressure with Mach number at zero pitch angle.

His geometry reveals that the pressure taps where situated at $x/D_{DN} = 1.7$, well within the region influenced by the nose, therefore causing discrepancy between the conical theory and the experimental measurements at the orifice location.

The surface pressure coefficient as given by Cheng[57] to a second-order approximation permits expressing the pressure coefficient for diametrically opposed orifices as:

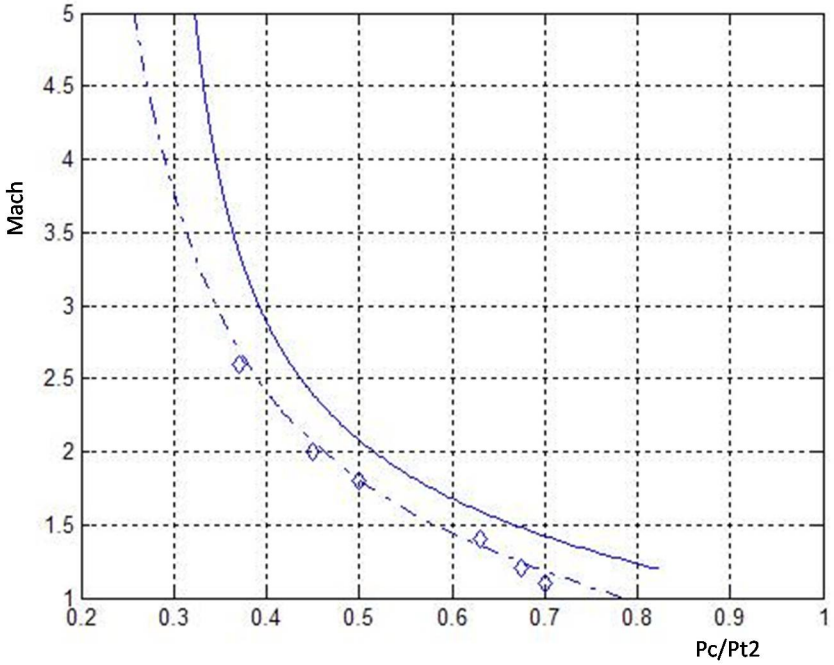


Figure C.3: Sharp cone theory results and Kasnov solution for the Onera probe [Measuring techniques for transonic and supersonic flow in cascades and turbomachines : proceedings of the 7th Symposium ]

$$\Delta C_p = 2sin^2\delta_c \left[4\xi cos\delta_c cos\phi - \frac{2\lambda\xi cos\phi}{cos\delta_c}\left(\frac{sin^2\delta_c}{2} - \frac{4}{15}\right)\right] \tag{C.3}$$

Where $\lambda = \frac{\gamma-1}{\gamma+1}$ and $\xi = \frac{sin\theta}{sin\delta_c}$.

In this equation, $\phi$ denotes the meridian angle of either one of the two orifices. One important note is that in deriving the above expression the limit $K \rightarrow 0$ ( hypersonic speeds) was not needed. The terms containing $K$ as a factor cancel each other and give an expression independent of Mach number . In his experimental work Swalley[58] concluded that the $40^o$ half-angle probe cone showed good agreement at a Mach number of 21 in helium and a Mach number of 3.55 in air confirming the theoretical indications. He concluded that only one calibration curve is required to determine the flow angularity over a wide Mach number range in either air or helium.

# Appendix D

# New integrated sampling probe and gas analyzer

The following section is intended to show the basic analytical calculations performed in the probe design process. An Idealized flow model of the VT probe is illustrated in Figure D.1.

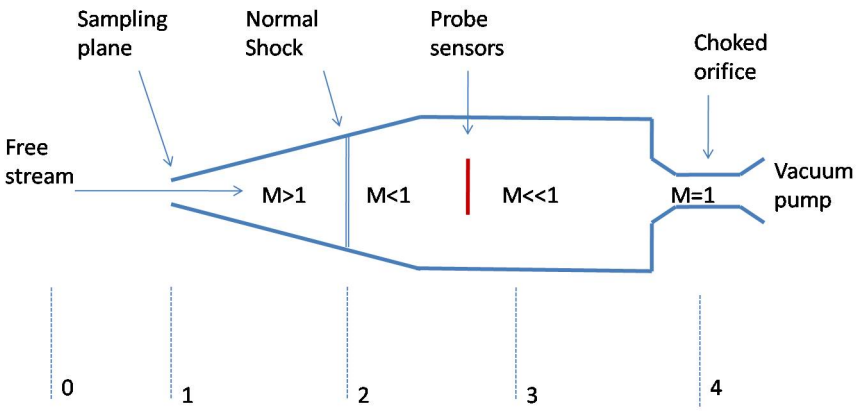


Figure D.1: **Schematic of the new probe tip**

In the flow model, the following assumptions have been made.

1)Sample enters probe at a Mach number greater than or equal to one
2)Isentropic supersonic expansion upstream of normal shock
3)Normal shock occurs in diverging probe inlet (for isokinetic sampling)
4)Isentropic flow and subsonic expansion downstream of shock
5)Flow is choked at probe exit ( section 4)

Furthermore, it is necessary to slow the flow to a low subsonic Mach number in the sensor plane to a value at which the total and static conditions are only negligibly different. The design of the extraction probe and orifice geometry entails trade-off studies between the normal shock location and maximum strength and Mach number at the sensor plane. For a given probe inlet geometry and Mach number just upstream the shock, the location of the shock may be determined using the area Mach number relation:

$$\frac{A_2}{A_1} = \frac{1}{M_2}\left[\frac{2}{\gamma-1}\left(1+\frac{\gamma-1}{2}M_2^2\right)\right]^{\frac{\gamma+1}{2(\gamma-1)}} \tag{D.1}$$

This permits solving for $A_2$ and the corresponding axial location. The conditions just downstream of the shock may be obtained using the normal shock relations and the remaining conditions at the sampling plane may be determined using quasi-one-dimensional compressible flow relations. A computer program was written to conduct parametric studies in order to optimize the geometry over a larger range of flow conditions. Analysis of the results produced the geometry shown in Figures D.2 to D.4.

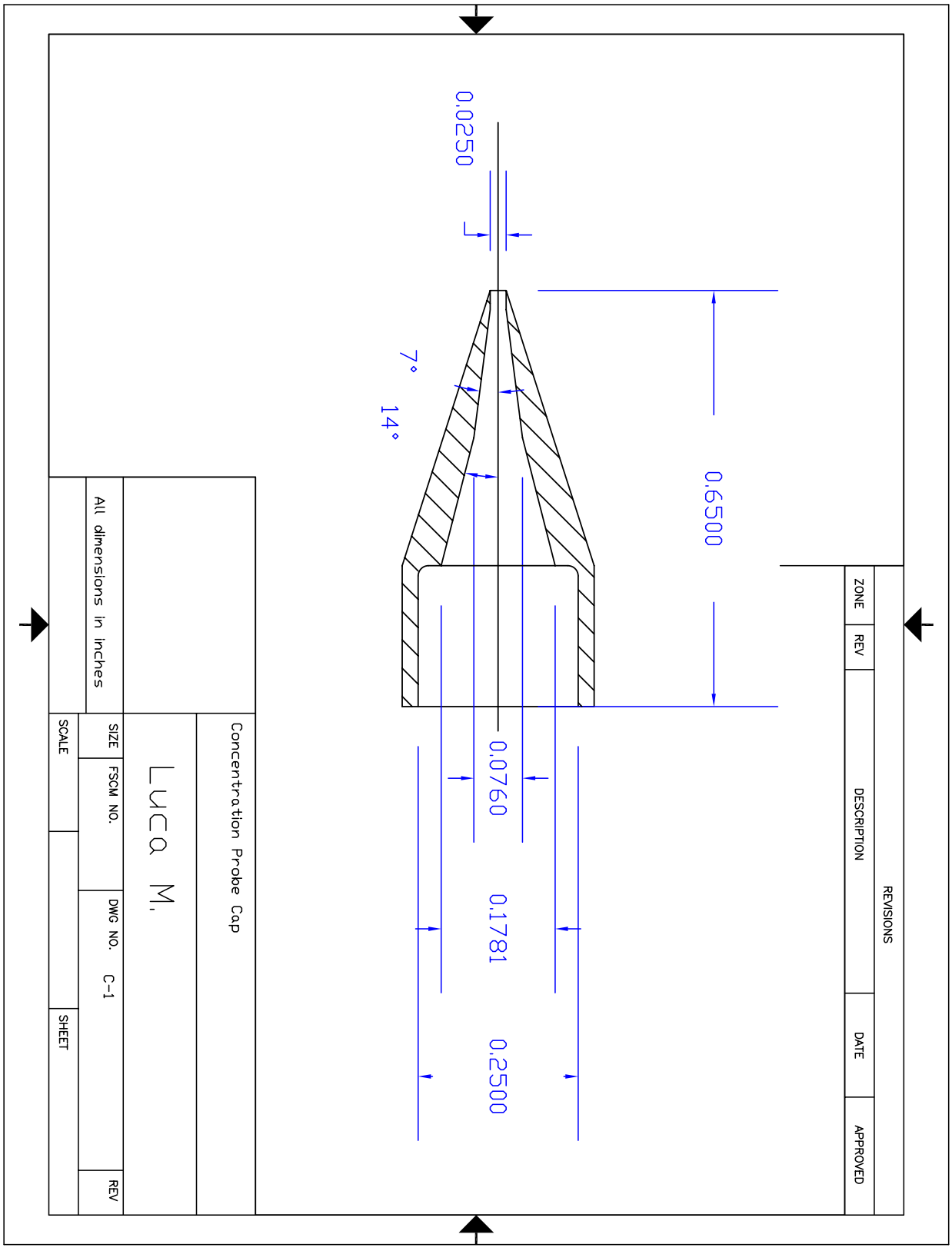


Figure D.2: **Schematic of the new concentration probe tip**

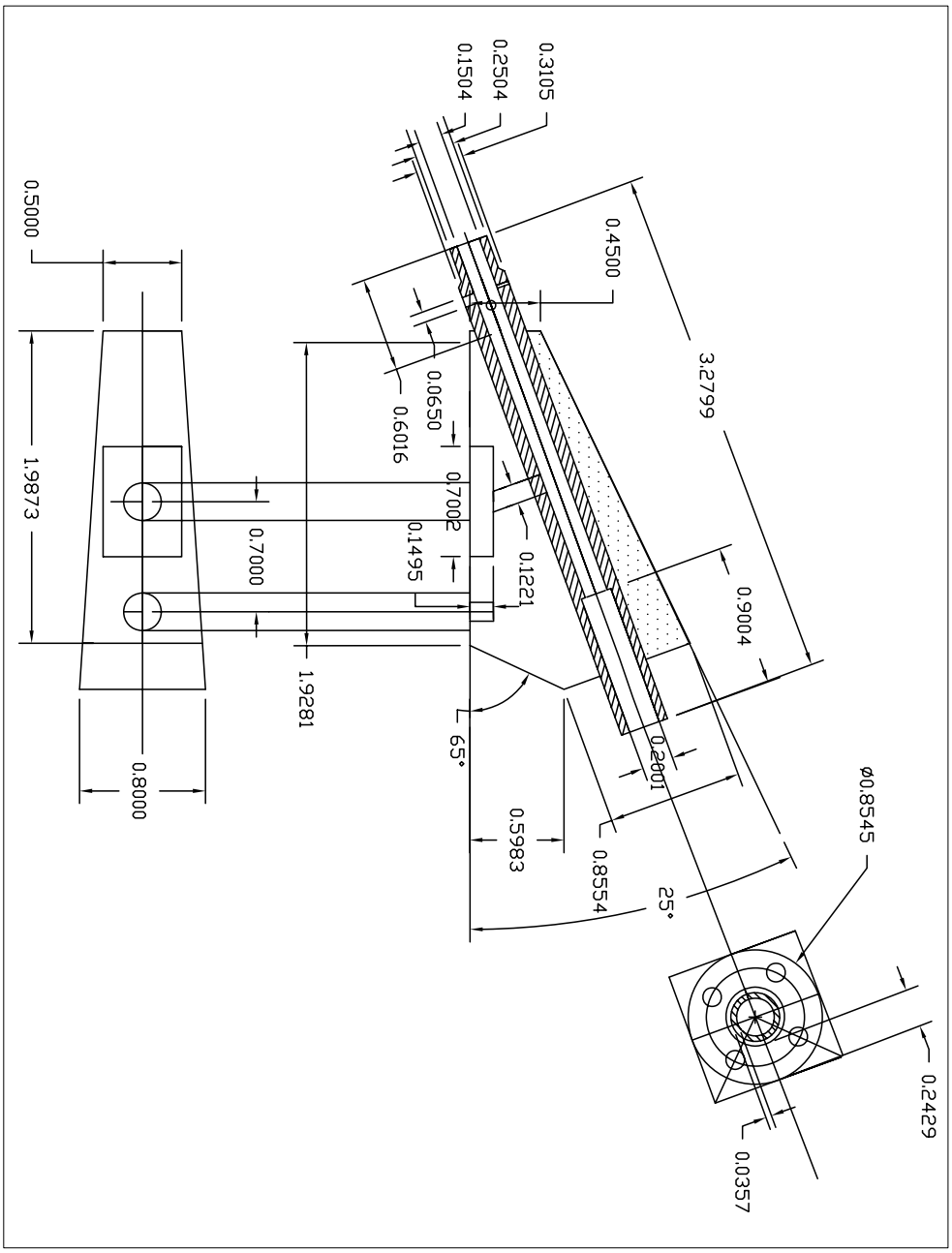


Figure D.3: **Schematic of the new probe**

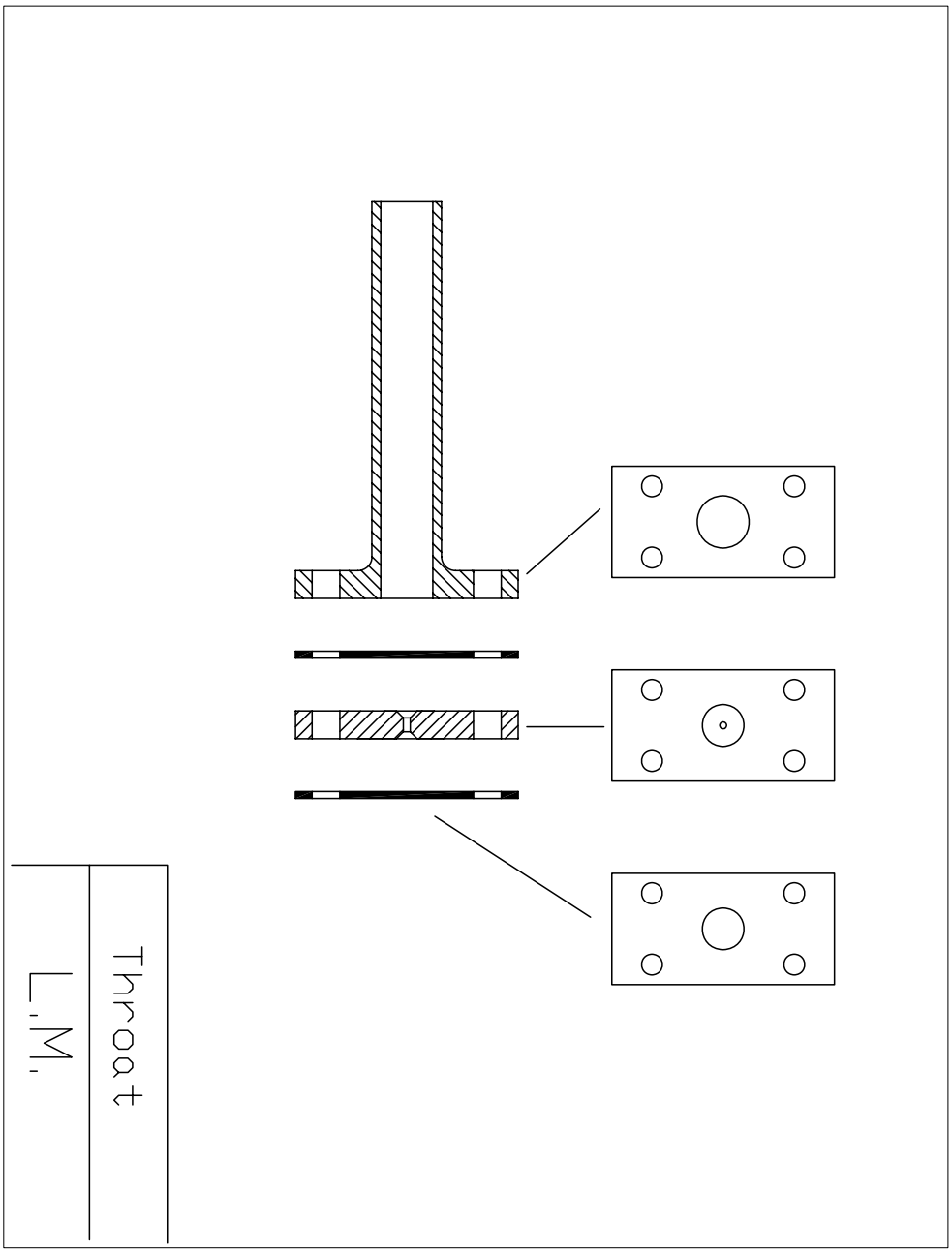


Figure D.4: **Schematic of the removable probe throat assembly**

# Vita

Luca Maddalena was born on January 21, 1974 in San Vito al Tagliamento, Pordenone Italy. In 1992, he graduated from Istituto Tecnico Malignani High School, Udine. In the same year, he began his Laurea degree study in the Aerospace Department of the Polytechnic of Milan. In 2004, he graduated from the same school with a Laurea degree in Aeronautical Engineering. In the same period he graduated from the Scuole Centrali Antincendi of Rome as Firefighter.